

# **A Study of Doubly Crosslinked Microgels and Their Composites**

A thesis submitted to the University of Manchester for the degree of

Doctor of Philosophy

in the Faculty of Science and Engineering

**Submitted 2016**

**Zhengxing Cui**

School of Materials

The University of Manchester

# Contents

<b>Contents .....</b>	<b>1</b>
<b>List of Figures.....</b>	<b>4</b>
<b>List of Tables .....</b>	<b>9</b>
<b>List of Abbreviations .....</b>	<b>10</b>
<b>List of Symbols .....</b>	<b>12</b>
<b>Abstract.....</b>	<b>16</b>
<b>Declaration.....</b>	<b>17</b>
<b>Copyright Statement.....</b>	<b>18</b>
<b>Acknowledgements.....</b>	<b>19</b>
<b>Chapter 1: Introduction .....</b>	<b>20</b>
<b>1.1 Aims of the study .....</b>	<b>20</b>
<b>1.2 Survey of thesis .....</b>	<b>20</b>
<b>1.3 References .....</b>	<b>24</b>
<b>Chapter 2: Literature review .....</b>	<b>25</b>
<b>2.1 Microgels .....</b>	<b>25</b>
<b>2.1.1 Free-radical polymerisation.....</b>	<b>26</b>
<b>2.1.2 Polymerisation involving crosslinking monomers .....</b>	<b>29</b>
<b>2.1.3 Emulsion polymerisation.....</b>	<b>30</b>
<b>2.1.4 Colloidal dispersion .....</b>	<b>32</b>
<b>2.1.5 Colloidal stability and DLVO theory .....</b>	<b>33</b>
<b>2.1.6 Stabilisation of MG particles .....</b>	<b>37</b>
<b>2.1.7 The pH-responsive microgels.....</b>	<b>38</b>
<b>2.1.8 The swelling of microgel particles .....</b>	<b>39</b>
<b>2.1.9 The gel networks of pH-responsive doubly crosslinked microgels.....</b>	<b>44</b>
<b>2.2 Nanocomposites hydrogels.....</b>	<b>47</b>
<b>2.2.1 Nanocomposite strategy .....</b>	<b>47</b>
<b>2.2.2 Hydrogels containing graphene oxide.....</b>	<b>48</b>
<b>2.2.3 Hydrogels contain carbon nanotubes.....</b>	<b>50</b>
<b>2.2.4 Mechanical properties of composites .....</b>	<b>53</b>
<b>2.3 Instrumentation .....</b>	<b>56</b>
<b>2.3.1 Dynamic light scattering .....</b>	<b>56</b>
<b>2.3.2 Raman spectroscopy .....</b>	<b>58</b>
<b>2.3.3 Dynamic rheology .....</b>	<b>60</b>
<b>2.3.4 Scanning electron microscopy .....</b>	<b>62</b>

2.3.5	Transmission electron microscopy .....	64
2.4	References .....	67
Chapter 3: Microgel/Graphene oxide composites .....		78
3.1	Abstract .....	78
3.2	Introduction .....	79
3.3	Experimental.....	81
3.3.1	Materials .....	81
3.3.2	Synthesis of graphene oxide .....	81
3.3.3	Synthesis of poly(EA/MAA/BDDA) microgel.....	82
3.3.4	Synthesis of GMA-functionalised poly(EA/MAA/BDDA) microgel .. .....	82
3.3.5	Preparation of SX MG/GO physical gels and DX MG/GO covalent gels .....	83
3.3.6	Physical measurements.....	83
3.3.7	Assessment of cytotoxicity .....	84
3.4	Results and discussion .....	85
3.4.1	Microgel characterisation .....	85
3.4.2	Graphene oxide characterisation .....	89
3.4.3	Composite gel characterisation.....	92
3.5	Conclusions .....	106
3.6	References .....	107
Chapter 4: Microgel / multi-walled carbon nanotubes composites .....		111
4.1	Abstract .....	111
4.2	Introduction .....	112
4.3	Experimental.....	115
4.3.1	Materials .....	115
4.3.2	Preparation of MG dispersion .....	115
4.3.3	Preparation of SX/CNT <sub>x</sub> dispersions .....	116
4.3.4	Preparation of DX MG/CNT <sub>x</sub> composite gels .....	116
4.3.5	Physical Measurements .....	117
4.3.6	Cytotoxicity studies.....	118
4.4	Results and discussion .....	120
4.4.1	Microgel characterisation .....	120
4.4.2	Characterisation of CNT .....	122
4.4.3	Characterisation of MG/CNT dispersions.....	124
4.4.4	Characterisation of SX MG/CNT and DX MG/CNT gels.....	128
4.5	Conclusions .....	140

4.6	References .....	141
<b>Chapter 5: Using intra-microgel crosslinking to control the mechanical properties of doubly crosslinked microgels .....</b>		
5.1	Abstract .....	144
5.2	Introduction .....	145
5.3	Experimental.....	149
5.3.1	Materials .....	149
5.3.2	Microgel synthesis.....	149
5.3.3	Preparation of doubly crosslinked microgels.....	151
5.3.4	Physical Measurements .....	151
5.4	Results and discussion.....	153
5.4.1	Microgel particle size and pH-triggered swelling .....	153
5.4.2	Dynamic rheological measurements for SX MGs and DX MGs ..	158
5.4.3	DX MG morphology .....	161
5.4.4	Uniaxial compression and bending of the DX MGs.....	162
5.4.5	Proposed relationship between MG and DX MG mechanical properties.....	165
5.5	Conclusions .....	167
5.6	References .....	168
<b>Chapter 6: Conclusions and future works.....</b>		
6.1	Summary of conclusions .....	172
6.2	Future works.....	174
6.3	References .....	176
<b>Appendix.....</b>		177
Published works.....		177

**Final word count: 38872**

## List of Figures

<b>Fig. 2.1.</b> The MG particle in a poor solvent (a) and a good solvent (b).	25
<b>Fig. 2.2.</b> Two possible models of propagation of free radical polymerisation.	27
<b>Fig. 2.3.</b> The combination and disproportionation of termination.	28
<b>Fig. 2.4.</b> Chemical structures of DVB and EGDMA.	30
<b>Fig. 2.5.</b> The schematic diagram of three intervals in emulsion polymerisation.	31
<b>Fig. 2.6.</b> Schematic diagram of conversion versus reaction time for three intervals of a classic emulsion polymerisation.	32
<b>Fig. 2.7.</b> Schematic diagram of two particles in the medium.	34
<b>Fig. 2.8.</b> Schematic diagram of different planes and potentials in double layer.	35
<b>Fig. 2.9.</b> Schematic diagram of potential energies versus distance of two particles.	37
<b>Fig. 2.10.</b> Schematic diagram of steric stabilisation between two MG particles.	38
<b>Fig. 2.11.</b> (a) Dependence of microgel size on neutralisation and crosslinker contents. The curves from top to bottom correspond to crosslinker contents from low to high. (b) Dependence of microgel size on degree of neutralisation and salt concentration.	44
<b>Fig. 2.12.</b> The schematic diagram of DX gels formation. Step A is the surface of MG particles modified by vinyl groups. Step B is the particles swelling and contact. The final step is the formation of DX MGs.	45
<b>Fig. 2.13.</b> The formation microgel networks by direct contact ((a) and (b)), microgel-mediated crosslinking ((c) and (d)) and physical microgel entrapment ((e) and (f)).	46
<b>Fig. 2.14.</b> The structure of graphene oxide.	48
<b>Fig. 2.15.</b> (a) The structures of SWNT and MWCNT. (b) The high resolution TEM image of MWNT. The inset shows the structure of MWNTs.	51
<b>Fig. 2.16.</b> The application of carbon nanotubes nanocomposites hydrogels.	52
<b>Fig. 2.17.</b> The schematic diagram of isostrain and isostress conditions.	53
<b>Fig. 2.18.</b> The comparison of isostrain and isostress conditions. The black data points are shown a real case of an epoxy/carbon fibre composites.	55
<b>Fig. 2.19.</b> Scheme of the set-up for DLS instrument.	56
<b>Fig. 2.20.</b> Energy level diagram of Rayleigh and Raman scattering processes.	58
<b>Fig. 2.21.</b> A typical Raman Spectrometer.	59

<b>Fig. 2.22.</b> The shear deformation of an ideal solid.	60
<b>Fig. 2.23.</b> Schematic diagram of the SEM.	63
<b>Fig. 2.24.</b> Schematic diagram of the TEM.	66
<b>Fig. 3.1.</b> The main mechanism of GMA functionalisation reaction.	85
<b>Fig. 3.2.</b> Potentiometric titration data for (a) NF MG and (b) SX MG.	86
<b>Fig. 3.3.</b> (a) Hydrodynamic diameters and (b) particle volume-swelling ratios ( $Q$ ) of NF MG and SX MG in a range of pH from 4 to 11.	88
<b>Fig. 3.4.</b> SEM images of (a) NF MG and (b) SX MG particles.	88
<b>Fig. 3.5.</b> SEM images of SX MG cross-section sample. The particles were on a silicon substrate (lower part in (b)). The layer (upper layer in (b)) on the substrate was the platinum coating layer with a thickness of $\sim 12$ nm.	89
<b>Fig. 3.6.</b> (a) TEM image of a GO sheet and (b) SEM of a GO sheet.	90
<b>Fig. 3.7.</b> Raman spectra for as supplied graphite powder (a) and GO (b). Note that (b) is the normalised Raman spectrum.	91
<b>Fig. 3.8.</b> Digital photographs of GO water dispersions. The concentrations in wt.% are shown in the bottom.	91
<b>Fig. 3.9.</b> Digital photos of composites, (a) The pH-triggered fluid-to-gel transition of SX MG/GO <sub>0.50</sub> . (b) The SX MG/GO gels were injectable and also mouldable as can be seen from the SX MG/GO <sub>1.0</sub> gel. (c) DX MG/GO gels were prepared as cylinders by using DX MG/GO <sub>1.0</sub> gel as an example. The scale bars for (b) and (c) are 5 mm.	92
<b>Fig. 3.10.</b> SEM of DX MG/GO <sub>1.0</sub> gel ((a) and (b)) and DX MG ((c) and (d)). (b) and (d) are higher magnification images. The yellow arrows show the spherical particles on the gel surface. The Red arrows indicate the different roughness on the surfaces of gel walls.	93
<b>Fig. 3.11.</b> SEM Images are shown for freeze-dried DX MG/GO <sub>1.0</sub> after being heated to 550°C under N <sub>2</sub> . The inset for (b) shows GO sheets.	94
<b>Fig. 3.12.</b> Thermo gravimetric analysis data for DX MG/GO <sub>1.0</sub> . The sample was heated under a nitrogen atmosphere, and the temperature was maintained at 550 °C after the heating ramp was completed.	95
<b>Fig. 3.13.</b> Frequency-sweep studies for various gels containing GO. (a), (b) and (c) showed the $G'$ (close symbols) and $G''$ (open symbols) data in a range of frequency for GO dispersion, SX MG/GO physical gels and DX MG/GO gels, respectively. (c), (d) and (e) showed the relaxation component, $G'$ and $\tan \delta$ as the function of $C_{GO}$ . The legend in (b) applied to (a) and (c). The legend in (d) applied to (e) and (f).	97

- Fig. 3.14.** Strain-sweep data showing the variation of  $G'$  (closed symbols) and  $G''$  (open symbols) with strain ( $\gamma$ ) are shown for GO (a), SX MG/GO (b) and DX MG/GO (c). The legend for (a) applies to (b) and (c). (d) shows the  $\Delta G''_n$  (see text) dependence on GO concentration ( $C_{GO}$ ). (e) shows the variation of the yield strain ( $\gamma^*$ ) with  $C_{GO}$ . 99
- Fig. 3.15.** The fitting curve of storage modulus on the volume fraction of GO within the DX MG/GO network. 102
- Fig. 3.16.** Static compression data for various gels. (a) shows the selected stress versus extension ratio ( $\lambda$ ) curves for different DX MG/GO gels. (b) shows the effects of GO concentration on the maximum strain ( $\epsilon_{max}$ ) and maximum true stress ( $\sigma_{T(max)}$ ). The variation of modulus with  $C_{GO}$  is shown in (c). 103
- Fig. 3.17.** Cell challenge experiments for DX MG/GO gels. Live / Dead assays for Nucleus pulposus cells contacted DX MG/GO<sub>0.5</sub> in a period of 10 days (a) – (c), the Live control samples are shown in (d) – (f) and the dead control sample is shown in (g). Nucleus pulposus cells contacted DX MG/GO<sub>0.5</sub> under a toroid-shaped gel (h) in a well plate. 104
- Fig. 3.18.** The morphology of cells in Live / Dead assays. The Nucleus pulposus cells contacted DX MG/GO<sub>0.5</sub> in a period of 10 days (a) – (c), the Live control samples are shown in (d) – (f). 105
- Fig. 4.1.** Potentiometric titration data for SX MG before (a) and after (b) the GMA functionalisation. 120
- Fig. 4.2.** (a) Hydrodynamic diameters and (b) particle volume-swelling ratios ( $Q$ ) of SX MG particles over a range of pH values. 121
- Fig. 4.3.** SEM images of SX MG particles. 122
- Fig. 4.4.** SEM images of as-supplied (a) and (b), Images after dispersing CNT using ultrasonication (c) and (d). 123
- Fig. 4.5.** Raman spectra of (a) as-supplied CNTs and (b) the CNTs after ultrasonication in water. 124
- Fig. 4.6.** Optical micrographs of CNT (1 wt.%) dispersed in (a) MG solution (10 wt.%, pH = 6.8) as a viscous fluid, (b) water and (c) in aqueous SDS (2.5 wt.%) solution. All images were taken within 5 minutes after ultrasonication. 125
- Fig. 4.7.** (a) Optical micrograph of SX MG/CNT<sub>1.0</sub> gel and the photographs of SX MG/CNT<sub>1.0</sub> dispersion (b) and gel ((c) and (d)). The scale bars in (b)-(d) represent 10 mm. The red arrows in (a) showed the CNT bundles. 126
- Fig. 4.8.** (a) showed the MG and CNTs formed a macroscopic aggregate. (b) showed the sediments of CNTs in water. The CNT concentration in both cases was 0.5 wt.%. 127

- Fig. 4.9.** TEM images showed (a) CNTs were distributed in a MG concentrated layer and (b) the evidence of CNT-MG interaction. The insets of b showed (i) the entangled CNTs, (ii) the interaction between CNT and MG particles, (iii) MG particles bridging two CNTs. 128
- Fig. 4.10.** SEM images of a freeze-dried DX MG1/CNT<sub>0.5</sub>. (a), (b) show low and high magnification images. The red arrows in (a) shows many CNTs can be observed on the surface of DX MGs. The inset in (b) shows CNT on the surface. 129
- Fig. 4.11.** TGA data for DX MG/CNT<sub>0.5</sub> when heated under a N<sub>2</sub> atmosphere. 130
- Fig. 4.12.** SEM images of a DX MG1/CNT<sub>0.5</sub> gel after heating at 800 °C in N<sub>2</sub>. 131
- Fig. 4.13.** A sample that was fractured and then freeze-dried and the SEM images show a fracture surface. (a) shows a crack on the gel surface. (b) shows the higher magnification images of the tail part of the crack. The inset in (a) showed the position of the tail part. The insets in b showed the pulled-out CNTs, which were also highlighted by red arrows. 132
- Fig. 4.14.** Variable pH swelling behaviour for DX MG/CNT<sub>1.0</sub> gels. (a) showed the as-made DX MG/CNT<sub>1.0</sub> gels. (b) showed the size of samples after being placed in various buffer solutions for 7 days. Volume swelling ratios are also shown. (c) and (d) showed the sample in buffer solutions at pH 4 and 10, respectively, after 30 days. (e) showed a piece of SX MG/CNT<sub>1.0</sub> gel was placed into buffer solution and (f) showed the gels re-dispersed after 30 minutes. 133
- Fig. 4.15.** Conductivity vs. CNT concentration for DX MG/CNT composite gels. The inset shows a fit for the data to the percolation power law. 134
- Fig. 4.16.** Dynamic rheology data for to DX MG/CNT (black) and SX MG/CNT (red), respectively. Frequency-sweep data are in the left column. For (a), (c), (e), (g) and (i), the closed and open symbols are  $G'$  and  $\tan \delta$ , respectively. Strain-sweep data are shown in in the right column. For (b), (d), (f), (h) and (j), The closed and open symbols are  $G'$  and  $G''$ , respectively. The concentrations of CNT used to prepare the composite gels were 0 ((a) and (b)), 0.25 ((c) and (d)), 0.50 ((e) and (f)), 0.75 ((g) and (h)) and 1.0% ((i) and (j)). 135
- Fig. 4.17.** Summary of dynamic rheology data for SX MG/CNT and DX MG/CNT gels. (a) showed the effect of CNT concentration on modulus and critical strain for (a)SX MG/CNT and (b) DX MG/CNT. 137
- Fig. 4.18.** Compression data for DX MG/CNT gel composites. (a) shows stress vs strain curve for various CNT concentrations. (b) and (c) show the effect of CNT concentration on modulus and strain at break, respectively. 138



- Fig 4.19.** Cytotoxicity study for DX MG/CNT<sub>1,0</sub>. Live-Dead staining showing (a) ASC cells exposed to DX MG/CNT<sub>1,0</sub> gel at day 7, and (b) showed cells without exposure to the composite in the same condition. (c) Graph showing the metabolic activity of MSCs after exposure to the gels for different time periods. 139
- Fig. 5.1.** Potentiometric titration data for (a) SX DVB, (b) SX DVB-BDDA, (c) SX BDDA MGs. 153
- Fig. 5.2.** (a) Hydrodynamic diameters and (b) particle volume-swelling ratios ( $Q$ ) of SX MG particles at pH 4 to pH 11 measured at various value. 155
- Fig. 5.3.** TEM images of (a) SX DVB, (b) SX DVB-BDDA and (c) SX BDDA particles. The arrows indicate the particle-particles contact area. The insets show higher resolution images of several representatives connected particles. The scale bars for each inset represent 50 nm. 157
- Fig. 5.4.** (a) the inversion test of DVB SX (b) “MG” letters written by continuous injection of DVB SX gel. 158
- Fig. 5.5.** Strain-sweep rheology data for SX MG physical gels (left) and the corresponding covalently-interlinked DX MGs (right). The data shown are for (a) SX DVB, (b) DX DVB. (c) SX DVB-BDDA, (d) DX DVB-BDDA, (e) SX BDDA and (f) DX BDDA. The closed and open symbols represent the storage modulus ( $G'$ ) and the loss modulus ( $G''$ ), respectively. 159
- Fig. 5.6.** The critical strain of SX MG gels (a) and the DX MGs (b). Shear modulus of SX MG (c) and DX MGs (d). 160
- Fig. 5.7.** SEM images for freeze-dried DX DVB (a) and (b), DX DVB-BDDA (c and d) and DX BDDA (e and f). (a), (c) and (e) are low magnification images and (b), (d) and (f) are higher magnification images. 162
- Fig. 5.8.** Uniaxial compression stress vs. strain data for DX MGs prepared using various crosslinkers. The photographs show DX DVB MG compressed at different strains which were (a) 0%, (b) 40% and (c) 80%. The scale bars represent 10 mm. 163
- Fig. 5.9.** The DX DVB MG film was tested under bending followed by relaxations cycles. The process was repeated for three times. (The sample is prepared as pie shape with diameter of 20 mm and thickness of 2 mm and cut in half). 164
- Fig. 5.10.** (a) Variations of the modulus,  $E$ , and the strain-at-break,  $\varepsilon_b$ , for the DX MGs with the MG particle swelling ratio,  $Q$ , for the respective parent MG particles. (b) and (c) show the relationships between the  $E$  and  $\varepsilon_b$  values, respectively, and  $Q$ . 166

## List of Tables

<b>Table 3.1.</b> Characterisation data for MGs particles.	87
<b>Table 4.1.</b> Characterisation data for the MG.	120
<b>Table 5.1.</b> Compositions of the mixed co-monomer solutions used to synthesise the MGs.	150
<b>Table 5.2.</b> Characterisation data for the MGs investigated in this work.	154
<b>Table 5.3.</b> Static uniaxial compression data for the DX MGs.	164

## List of Abbreviations

APS	Ammonium persulfate
BDDA	1,4-butanediol diacrylate
CNT	Carbon nanotube
COOH	Carboxylic acid group
CoV	Coefficients of variation
DI	Deionised water
DLS	Dynamic light scattering
DLVO	Derjaguin, Landau, Verwey and Overbeek
DVB	Divinylbenzene
DX	Doubly crosslinked
EA	Ethyl acrylate
EGDMA	Ethyl glycol dimethacrylate
GMA	Glycidyl methacrylate
GO	Graphene oxide
H <sub>2</sub> O <sub>2</sub>	Hydrogen peroxide
H <sub>2</sub> SO <sub>4</sub>	Sulfuric acid
HCl	Hydrochloric acid
IVD	Intervertebral disc
MAA	Methacrylate acid
MG	Microgel
MSC	Mesenchymal stem cell
MWNT	Multi-wall carbon nanotube
N <sub>2</sub>	Nitrogen

NaCl	Sodium chloride
NaNO <sub>3</sub>	Sodium nitrate
NaOH	Sodium hydroxide
NF	Non-functionalised
NP	Nucleus pulposus
P2VP	poly(2-vinylpyridine)
PBS	Phosphate buffered saline
PCS	Photon correlation spectroscopy
PNIPM	poly( <i>N</i> -isopropylacrylamide)
PS	polystyrene
rpm	Rotations per minute
SDS	Sodium dodecyl sulphate
SEM	Scanning electron microscopy
SWNT	Single-wall carbon nanotube
SX	Singly crosslinked
TEM	Transmission electron microscopy
TGA	Thermal gravimetric analysis

## List of Symbols

$a$	Particle radius
$A$	Hamaker constant or Area
$A_1$	Hamaker constant for particles in vacuum
$A_2$	Hamaker constant for media in vacuum
$C$	Concentration
$C_i$	Concentration of ions in the solution
$C_i'$	Concentration of ions in insides the swelling networks
$d_c$	Particle diameter in collapsed state
$d_h$	Particle diameter in swelling state
$D$	Translational diffusion coefficient
$e$	Charge
$E$	Modulus or compression modulus
$E_m$	Modulus of matrix
$E_r$	Modulus of reinforcement
$G$	Shear modulus
$G'$	Storage modulus
$G''$	Loss modulus
$G(\tau)$	Correlation coefficients functions
$f$	Initiator efficiency
$f_e$	Number of counterions per chain
$F$	Force
$h$	Height
$H$	Distance between particles

$I$	Scattered light intensity
$k$	Boltzmann constant
$k_d$	Rate coefficient for initiator dissociation
$k_p$	Rate coefficient of propagation
$k_t$	Rate coefficient of termination
$n$	number of random links
$n'$	Frequency exponent
$M_{eff}$	Average molecular weight of the elastically effective chains
$N_A$	Avogadro constant
$N_C$	Effective number of chains
$q$	Scattering vector
$Q, Q_V$	Volume swelling ratio
$Q_m$	Weight swelling ratio
$R$	Gas constant
$R_i$	Rate of initiation
$R_p$	Rate of propagation
$s$	Power law component of the network.
$t$	Time
$T$	Absolute temperature
$v_0$	Molar volume of the polymer
$v_1$	Molar volume of the solvent
$V_A$	Attractive interaction energy
$V_C$	Volume in collapsed state
$V_R$	Electrostatic repulsive energy
$V_S$	Volume in swelling state

$V_T$	The total potential energy between two particles
$z$	Valence
$\alpha$	Deformation ratio
$\gamma$	Parameter of potential
$\delta$	Phase angle
$\Delta G$	Free enthalpy change
$\Delta G_{mix}$	Free enthalpy of mixing polymer into solvent
$\Delta G_{el}$	Free enthalpy of elasticity
$\varepsilon$	Strain
$\varepsilon_c$	Strain on composite
$\varepsilon_m$	Strain on matrix
$\varepsilon_r$	Strain on reinforcement
$\varepsilon_{max}, \varepsilon_B$	Strain at break
$\gamma$	Shear strain
$\gamma^*$	Yield strain
$\gamma_c$	Critical strain
$\eta$	Viscosity of medium
$\theta$	Scattering angle
$\kappa$	Debye screening Parameter
$\lambda$	Extension ration
$\lambda_0$	Wavelength of the incident laser
$\pi$	Circular constant
$\pi_{res}$	Swelling pressure
$\pi_{mix}$	Osmotic pressure

$\pi_{el}$	Elastic response force from networks
$\pi_{ion}$	Force of ionisation
$\rho$	Density
$\sigma$	Shear stress
$\sigma$	Conductivity
$\sigma_c$	Stress on composite
$\sigma_{max}, \sigma_B$	Stress at break
$\sigma_m$	Stress on matrix
$\sigma_r$	Stress on reinforcement
$\tau$	Delay time
$\tau_s$	applied force per unit area
$\nu_{eff}$	Number density of effective elastic chains, $\nu_{eff}$
$\chi$	Flory-Huggins interaction parameter
$\Phi$	Osmotic coefficient for gel phase
$\phi_0$	Volume fraction of polymer without solvent
$\phi$	Volume fraction of polymer
$\phi_1$	Osmotic coefficient for solvent
$\phi_2$	Volume fraction of polymer in a swelling particle
$\phi_m$	Volume fractions of matrix
$\phi_r$	Volume fractions of reinforcement
$\psi_d$	Potential at stern plane
$\omega$	Angular frequency



## Abstract

This thesis presents a study of pH-responsive doubly crosslinked microgels (DX MGs) and associated investigations to enhance their performance. The potential application of this material is soft tissue engineering, so the research concerns mechanical properties, other properties like swelling, microporous and conductivity are also discussed. The MG particles are based on poly(EA/MAA/ $x$ ), where EA is the ethyl acrylate, MAA is the methacrylate acid and  $x$  represents the crosslinker. The particles were subsequently functionalised using glycidyl methacrylate (GMA) to introduce vinyl groups in the MG particles. The formation of DX MGs includes a pH triggered swelling of MG particles in the dispersion to form a physical gel and a heat-triggered free-radical reaction to form a covalent hydrogel.

The starting point of this study was using graphene oxide (GO) nanosheets to prepare DX MGs composites with a high modulus. We mixed low concentrations of GO with MG particles and formed DX MG/GO gels. Both shear and compressive modulus linearly increased with the concentration of GO, but the ductility of gels was slightly reduced. The moduli for the DX MG/GO gels was increased by a factor of 5 - 6 when only 1.0 wt.% of GO was included.

The next study used multi-wall carbon nanotubes (CNTs) which are widely used to prepare electrical conductive composites. A big challenge for applying CNTs is that they easily form large aggregates in water, which was solved by the space-filling and volume excluded properties of MG particles. The ductility of the composite DX gels increased with CNT concentration, as did the modulus. The conductivity of gels significantly increased with the concentration of CNT and they had a very low percolation threshold. The cytotoxic study for the composite gels showed that they were not toxic, so they may be suitable for soft tissue engineering.

The effect of crosslinking monomers in MG preparation was studied in the last part of the research. Three types of poly(EA/MAA/ $x$ ) MGs were studied and compared. The  $x$  value was 1 mol. % of divinylbenzene (DVB); 1,4-butanediol diacrylate (BDDA) or a 1:1 mixture of both DVB and BDDA. The MGs containing DVB demonstrated higher swelling and more ductile properties and could withstand ~76% of compressive deformation. Moreover, the effects of intra-MG crosslinking of the MGs on the swelling behaviour and the mechanical properties were investigated.

## **Declaration**

I declare that no portion of the work referred to in the thesis has been submitted in support of an application for another degree or qualification of this or any other university or other institute of learning.

Zhengxing Cui

## **Copyright Statement**

- i.** The author of this thesis (including any appendices and/or schedules to this thesis) owns certain copyright or related rights in it (the “Copyright”) and s/he has given The University of Manchester certain rights to use such Copyright, including for administrative purposes.
- ii.** Copies of this thesis, either in full or in extracts and whether in hard or electronic copy, may be made only in accordance with the Copyright, Designs and Patents Act 1988 (as amended) and regulations issued under it or, where appropriate, in accordance with licensing agreements which the University has from time to time. This page must form part of any such copies made.
- iii.** The ownership of certain Copyright, patents, designs, trade marks and other intellectual property (the “Intellectual Property”) and any reproductions of copyright works in the thesis, for example graphs and tables (“Reproductions”), which may be described in this thesis, may not be owned by the author and may be owned by third parties. Such Intellectual Property and Reproductions cannot and must not be made available for use without the prior written permission of the owner(s) of the relevant Intellectual Property and/or Reproductions.
- iv.** Further information on the conditions under which disclosure, publication and commercialisation of this thesis, the Copyright and any Intellectual Property and/or Reproductions described in it may take place is available in the University IP Policy (see <http://documents.manchester.ac.uk/DocuInfo.aspx?DocID=487>), in any relevant Thesis restriction declarations deposited in the University Library, The University Library’s regulations (see <http://www.manchester.ac.uk/library/aboutus/regulations>) and in The University’s policy on Presentation of Theses.

## Acknowledgements

Firstly, I would like to thank my supervisor Prof. Brian Saunders for his excellent advice, encouragements and support since I was a master student. Without his expertise and patient help, this thesis could not reach this form. His professionalism, preciseness and sincerity toward science are admirable to me and he is my academic role model.

I would like to thank all of the staff in the School of Materials, University of Manchester. In particular, I greatly appreciate Polly Greensmith for teaching me a lot of skills and techniques of the lab works. Many thanks also go to Dr. Shicheng Li and Manrui Zhang for their generous care and assistance.

I would also like to thank all of my group members for their efforts over my entire PhD life. I am so fortunate to have stayed in such a positive and friendly group. Specifically, I would like to thank Dr. Amirhossein Milani for kindly training me and frequent chats when I was a novice in the group. I would like to thank Mu Chen who was being five-year roommate with me. Thank you for sharing joys and supporting me over these years. I am grateful to Dr. Jennifer Saunders, Dr. Jane Bramhill, Dr. Somjit Tungchaiwattana, Dr. Nur Nabilah Shahidan, Dr. Sineenat Thaiboonrod, Dr. Junfeng Yan, Dr. Kyriaki Pafiti, Dr. Judith McCann, Dr. Robert Farley, Melody Obeng, Wenkai Wang, Qing Lian, Shanglin Wu, Mingning Zhu, Muhamad Sharan Musa, Aloïs Mispelon, Muhamad Zulhasif Mokhtar and Syazwani Mohd Zaki and I wish you all success and happy in the future. It is fantastic to work with your company.

Finally, I would like to give my deeply grateful to my family, especially my parents and my fiancée. Those warm words over the phone always gave me the strength and encouraged me to complete this journey.

# **Chapter 1: Introduction**

## **1.1 Aims of the study**

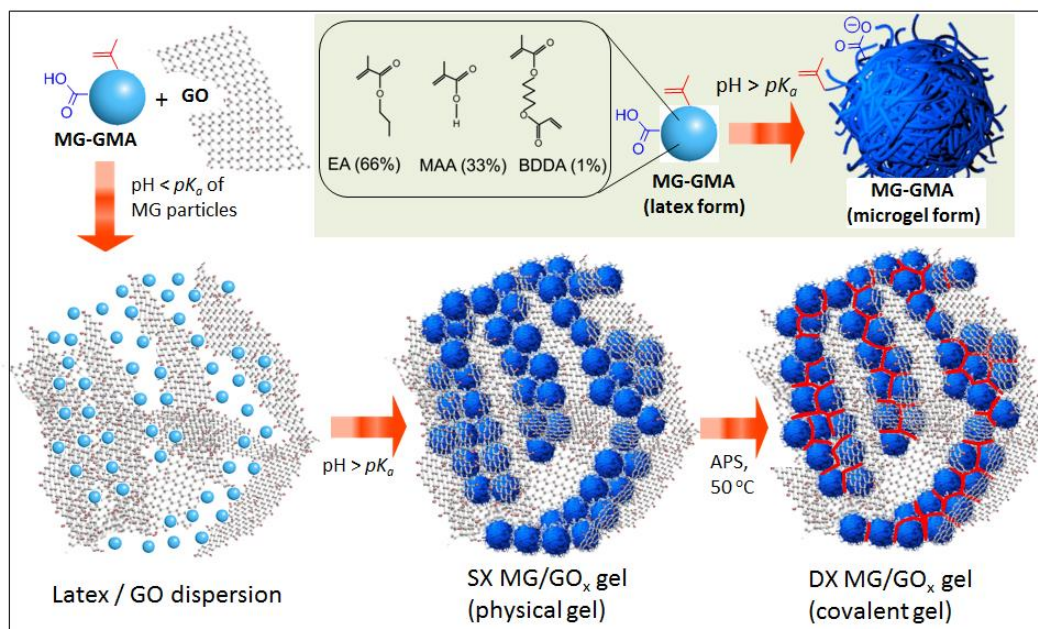
According to previous studies from our group, it has been shown that the pH-responsive doubly crosslinked microgel (DX MG) system can be applied as an injectable gel to restore the mechanical properties of the degenerated intervertebral disc (IVD).<sup>1-2</sup> However, one main limitation for this system to be extensively applied in soft tissue engineering is the relatively low modulus and brittleness. The aim of this thesis was to use composite strategies or adjusting the intra-crosslinking of the MG particles to prepare the covalent hydrogel with improved mechanical performance. Moreover, the results from this study should benefit the design and control of the properties of future DX MG systems and composites.

## **1.2 Survey of thesis**

The main part of this thesis starts with a literature review in Chapter 2. It is followed by three experimental Chapters (3 – 5) which will be introduced independently. The thesis ends with an overall conclusion in Chapter 6. Chapter 2 (literature review section) introduces key theories and backgrounds for the results and discussion chapters. This section includes an introduction to history and development of microgel and the nanocomposite hydrogels accompanying with associated theoretical information.

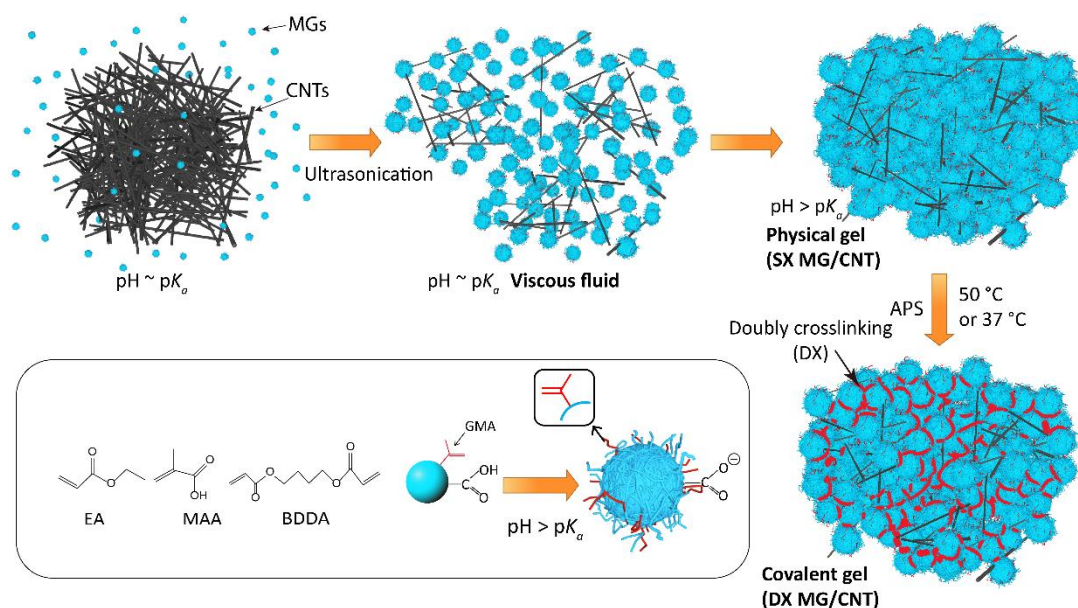
Chapter 3 introduces composite gels containing graphene oxide (GO) and DX MG.<sup>3</sup> The GO dispersion was prepared by a “modified Hummers method”.<sup>4</sup> The MG was prepared by a seed-feed emulsion polymerisation followed with a vinyl functionalisation step. These two materials, in the dispersed state, were mixed at low pH and formed a physical gel when neutralised. The covalently crosslinked

composite gels were formed by a free radical reaction under a heating condition in the presence of initiator. The mechanism of preparing the gels was summarised in Scheme 3.1 and will be discussed in detail later.



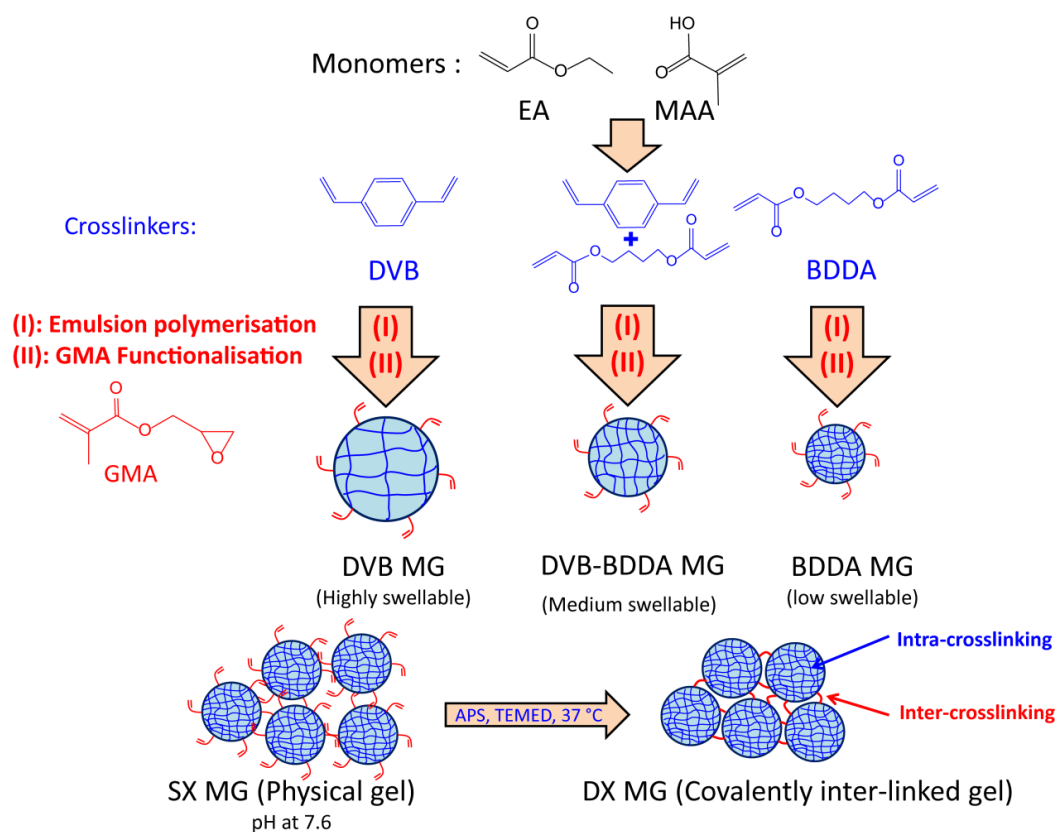
**Scheme 3.1. The depiction of the preparation of DX MG/GO gels.** The MG particles are prepared in their latex form and undergo pH-triggered swelling at pH values of greater than their  $\text{p}K_a$  (inset). The latex was mixed with GO and the pH increased to form a SX MG/GO physical gel. Heating the physical gel in the presence of ammonium persulfate (APS) covalently interlinked neighbouring MG particle interfaces (shown in red) to form a DX MG/GO gel. The MG phase is proposed to exist as domains within percolated, exfoliated, GO sheets.<sup>3</sup>

Chapter 4 introduces electrical conducting DX MG composites by using carbon nanotubes (multi-wall, CNTs) to replace GO.<sup>5</sup> The MG particles were synthesised by the same method as Chapter 3. After ultrasonication, the CNTs were well dispersed in a viscous fluid dispersion of MGs. The covalent gel formation process is same as mentioned in Chapter 3. The method used was summarised in Scheme 4.1.



**Scheme 4.1. The depiction of CNTs using microgels and DX MG/CNT formation.** The CNTs were initially dispersed in the presence of a viscous fluid of partially swollen vinyl-functionalised MG particles. The pH was increased to above the  $pK_a$ , triggering further MG swelling, and the formation of a physical gel (SX MG/CNT). In the presence of ammonium persulfate (APS) covalent interlinking (shown in red) occurred and the DX MG/CNT gel composite formed.<sup>5</sup>

Chapter 5 describes the preparation of some new MG particles by using a different crosslinker.<sup>6</sup> These MGs were designed to improve the ductility of the DX MGs, which was a limitation for future biomedical applications. The structural and pH-responsive mono-vinyl monomers (EA and MAA) were the same as used in Chapter 4 and 5. The differences in swelling and mechanical properties caused by using DVB or a mixture DVB-BDDA as crosslinkers are studied. The mechanism was shown in Scheme 5.1. Chapter 6 is a summary of the conclusions, and also provide ideas for future work.



**Scheme 5.1.** The Depiction of the method used to prepare MGs and DX MGs. Divinylbenzene (DVB), 1,4-butanediol diacrylate (BDDA) or a mixture of DVB and BDDA were used as intra-MG crosslinkers.<sup>6</sup>



### 1.3 References

1. Milani, A. H.; Freemont, A. J.; Hoyland, J. A.; Adlam, D. J.; Saunders, B. R., Injectable Doubly Cross-Linked Microgels for Improving the Mechanical Properties of Degenerated Intervertebral Discs. *Biomacromolecules* **2012**, 13, 2793-2801.
2. Liu, R.; Milani, A. H.; Freemont, T. J.; Saunders, B. R., Doubly crosslinked pH-responsive microgels prepared by particle inter-penetration: swelling and mechanical properties. *Soft Matter* **2011**, 7, 4696-4704.
3. Cui, Z.; Milani, A. H.; Greensmith, P. J.; Yan, J.; Adlam, D. J.; Hoyland, J. A.; Kinloch, I. A.; Freemont, A. J.; Saunders, B. R., A Study of Physical and Covalent Hydrogels Containing pH-Responsive Microgel Particles and Graphene Oxide. *Langmuir* **2014**, 30, 13384-13393.
4. Hummers, W. S.; Offeman, R. E., Preparation of Graphitic Oxide. *J. Am. Chem. Soc.* **1958**, 80, 1339-1339.
5. Cui, Z.; Zhou, M.; Greensmith, P. J.; Wang, W.; Hoyland, J. A.; Kinloch, I. A.; Freemont, T.; Saunders, B. R., A study of conductive hydrogel composites of pH-responsive microgels and carbon nanotubes. *Soft Matter* **2016**, 12, 4142-4153.
6. Cui, Z.; Wang, W.; Obeng, M.; Chen, M.; Wu, S.; Kinloch, I.; Saunders, B. R., Using intra-microgel crosslinking to control the mechanical properties of doubly crosslinked microgels. *Soft Matter* **2016**, 12, 6985-6994.

## Chapter 2: Literature review

### 2.1 Microgels

Microgels (MGs) are crosslinked polymer particles that swell in a good solvent.<sup>1</sup> The term “microgel” was first reported by Baker at 1945 to describe the crosslinked polybutadiene particles.<sup>2</sup> Such a term can be understood literally that the “micro” defines the particle size of MG in the range of 0.01  $\mu\text{m}$  to 1  $\mu\text{m}$  and the “gel” defines the polymeric networks can disperse and swell in a solvent to form the gel.<sup>3</sup> The structures of a collapsed and a swollen particle are shown in Fig. 2.1. The particles of MG are spherical (Fig. 2.1a), they can absorb solvent (Fig 2.1b) and swell in the dispersion. Formally, the collapsed form is a latex.

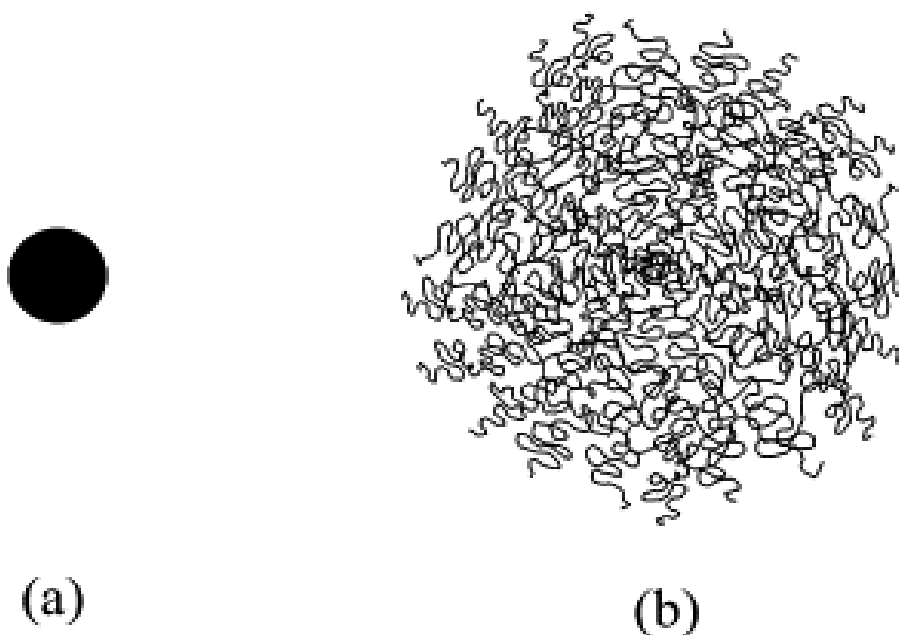


**Fig. 2.1.** A MG particle in a poor solvent (a) and a good solvent (b).<sup>1</sup>

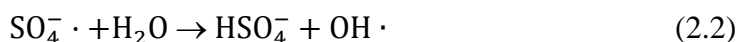
The following introduction to MGs will start from the preparation method. As colloidal dispersions, aggregation may appear on occasion if the attractive interactions dominate.<sup>4</sup> Therefore, the colloid stability of MG particles is discussed in the following. The properties of MG particles are described in the last part.

### 2.1.1 Free-radical polymerisation

Free-radical polymerisation is one of the most common reactions to synthesise polymers. It is a type of chain polymerisation and such chemistry can be applied to most of the vinyl monomers which contain the carbon-carbon double bonds. There are three basic stages in free radical polymerisation which are initiation, propagation and termination.

#### 2.1.1.1 Initiation

The initiation stage can be described as the generation of active centres which are the precondition for polymer chain formation and growth. The active centre is generated by the free radicals or ions from initiators attacking the  $\pi$  bonds of monomers.<sup>5</sup> For example, the free radicals ( $R\cdot$ ) can be generated by the thermal decomposition of persulphate in water as shown in following equations:<sup>6</sup>



Then the active centre ( $M\cdot$ ) can be generated by the free-radical ( $R\cdot$ ) attractive monomer ( $M$ ):



In the initial stage, the decomposition of initiator is the slow reaction which dominates the formation rate of the active centre. Therefore, the rate of initiation,  $R_i$  can be calculated by using the rate coefficient for initiator dissociation,  $k_d$ , initiator efficiency,  $f$  and the initiator concentration,  $[I]$ :

$$R_i = 2fk_d[I] \quad (2.4)$$

### 2.1.1.2 Propagation

The propagation is the stage of growth of polymer chains. The monomers can be sequentially added to the active centres in the chains at a rapid rate.<sup>5</sup> The following diagram shows the possible mode for propagation steps.

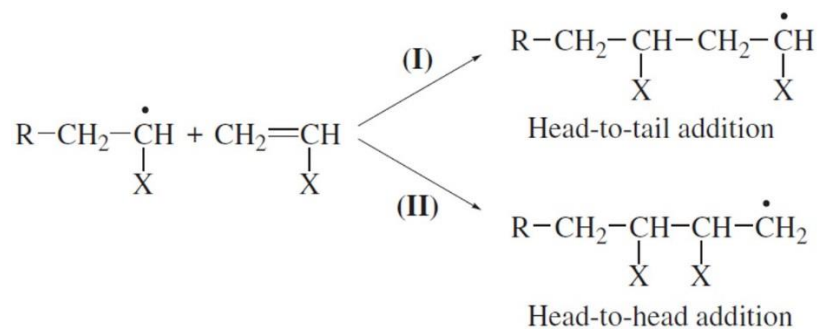


**Fig. 2.2.** Two possible models of propagation of free radical polymerisation.<sup>5</sup>

In this stage, it is assumed that the rate of propagation does not relate to the length of polymer chains. It depends on the concentration of active centre and monomer concentration. The concentration of active centre is not only determined by the initiation stage but also depends on the termination of free radicals.

### 2.1.1.3 Termination

The final stage of free-radical polymerisation is termination, which describes when active centres are annihilated and then the chain propagation is terminated. One mechanism of termination is the coupling of two active centres from two growing chains to form one dead polymer molecule. It is named as the combination of termination. Another mechanism is the disproportionation. Two dead polymer molecules are formed in this route, the active centre in two chains are terminated and transform to one saturated bond and one unsaturated bond.<sup>5</sup> Two mechanisms of termination are shown in Fig. 2.3. The tendency of each mechanism in a reaction depends on the monomer and polymerisation conditions. In general, both of them occur in the polymerisation. However, at 60 °C the polyvinyl cyanide is nearly 100%

terminated by combination. By contrast, the polyvinyl acetate is mostly terminated by disproportionation.<sup>7</sup>

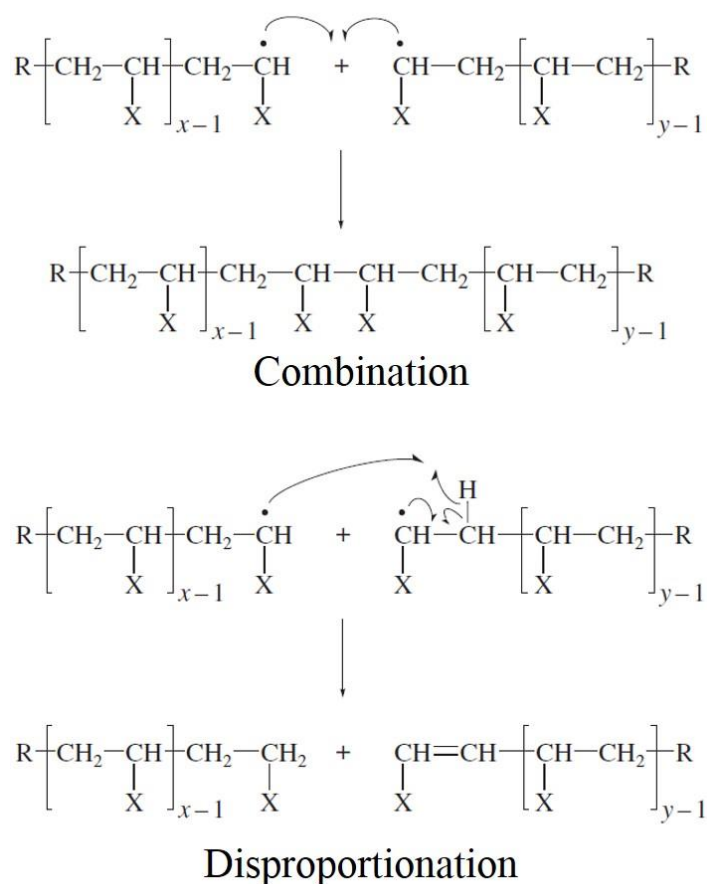


**Fig. 2.3.** The combination and disproportionation of termination.<sup>5</sup>

The rate of termination depends on the concentration of active centres and the rate coefficient of termination,  $k_t$ , which is the total rate coefficient of combination and disproportionation. Here, the rate of propagation,  $R_p$  can be calculated by a steady state condition in propagation when the generation and consumption rates are equal. Here, the rate of free-radical formation is as same as the rate of termination. The rate can be expressed as:

$$R_p = k_p \left( \frac{f k_d}{k_t} \right)^{0.5} [M] [I]^{0.5} \quad (2.5)$$

Where  $k_p$  is the rate coefficient of propagation.

### 2.1.2 Polymerisation involving crosslinking monomers

In a free-radical copolymerisation, if one type of monomer contains more than one carbon-carbon double bonds (i.e. the crosslinker or crosslinking monomer), then non-linear polymer chains could be formed.<sup>8</sup> A copolymerisation containing crosslinker leads to a branched polymer or 3D polymer network. It is widely used to synthesise the crosslinking particles,<sup>9-10</sup> which in our studies it is used to prepare MG particles. In most of the recipes, the amount of crosslinker only occupies a small percentage in the total monomers added.<sup>5</sup> The degree of crosslinking in particles is determined by the combination of mole fraction, the reactivity during polymerisation and the final conversion of crosslinker. Due to the difference from various crosslinkers, they are considered as very important factors in particles design and property control. He et al.<sup>11</sup> reported that the morphology and mechanical properties of polystyrene-*co*-divinylbenzene (PS-DVB) particles can be affected by the mole fraction of crosslinker (DVB). The high content of DVB in particles have a rougher surface and a lower deformability. Jin et al.<sup>12</sup> studied poly(glycidyl methacrylate-*co*-divinylbenzene) (poly(GMA-*co*-DVB)) particles and indicated the yield of polymerisation, the size of particles and the smoothness of particle surface were controlled by the DVB concentration.

Moreover, the different chemical structures of crosslinkers influence the polymer networks. In an ideal case, all of the double bonds from crosslinkers are involved in the reaction and the distribution of crosslinking junctions is homogenous. However, taking the ethylene glycol dimethacrylate (EGDMA) and the DVB as examples (their structures are shown in Fig.2.4), the two vinyl groups in one crosslinking monomer normally do not have equal reactivity or even cannot fully get involved into the

polymerisation. Landin et al.<sup>13</sup> used MMA and EGDMA as monomers to study network formation. They reported that the reactivity of pendent vinyl groups (from EGDMA) in polymer chains is about half of the first vinyl groups from EGDMA monomers. Besides, the formation of the network during polymerisation of poly(MMA/EGDMA) is non-ideal due to the cyclisation of pendant vinyl groups.<sup>13</sup> Compared to DVB, the EGDMA performs much more ideal for the vinyl-divinyl copolymerisation.<sup>5</sup> DVB normally consists of a mixture of isomers (para and meta) which have different reactivities.<sup>14</sup> Story et al. reported a study of PS-DVB MG using para DVB which is not homogenous.<sup>15</sup> When using a low concentration of DVB, a significant decrease of reactivity of the secondary vinyl groups is found after the first vinyl groups are reacted. However, when increasing the concentration of DVB, the risk from cyclisation of pendent vinyl groups will be greatly increased.<sup>16</sup> The inhomogeneous crosslinking distribution is also caused by the impurity of DVB as supplied.<sup>5</sup>

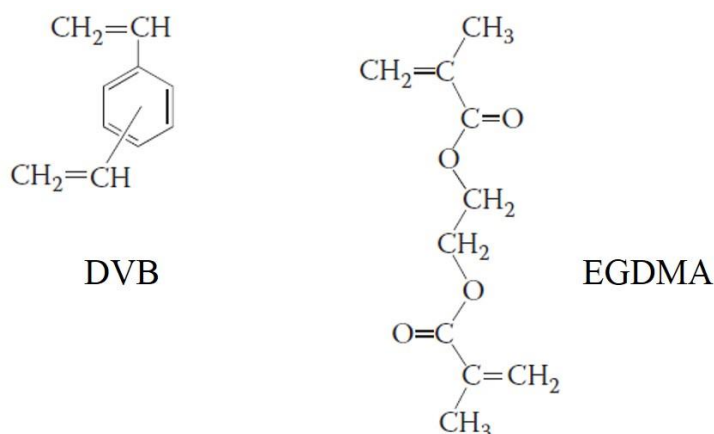


**Fig. 2.4.** Chemical structures of DVB and EGDMA.

### 2.1.3 Emulsion polymerisation

In this thesis, the synthesis of poly(EA-*co*-MAA-*co*-*x*) MGs is reported via a seed-feed emulsion polymerisation. The “*x*” represents a type of divinyl crosslinker. Emulsion polymerisation is one of the most widely used methods for synthesising

MG particles including poly(*N*-isopropylacrylamide) (PNIPAM) MG<sup>17</sup>, poly(2-vinylpyridine) (P2VP) MG<sup>18</sup> and their extending studies.<sup>19-20</sup> Classic emulsion polymerisation can achieve narrow polydispersed particles with a relatively rapid rate of free-radical based polymerisation.<sup>21</sup>

The mechanism of emulsion polymerisation can be explained as follows. The insoluble monomers are added into an aqueous solution containing surfactants and water-soluble free-radical initiator. In aqueous media, the monomers form latex which are stabilised by the surfactant (see Fig. 2.5).

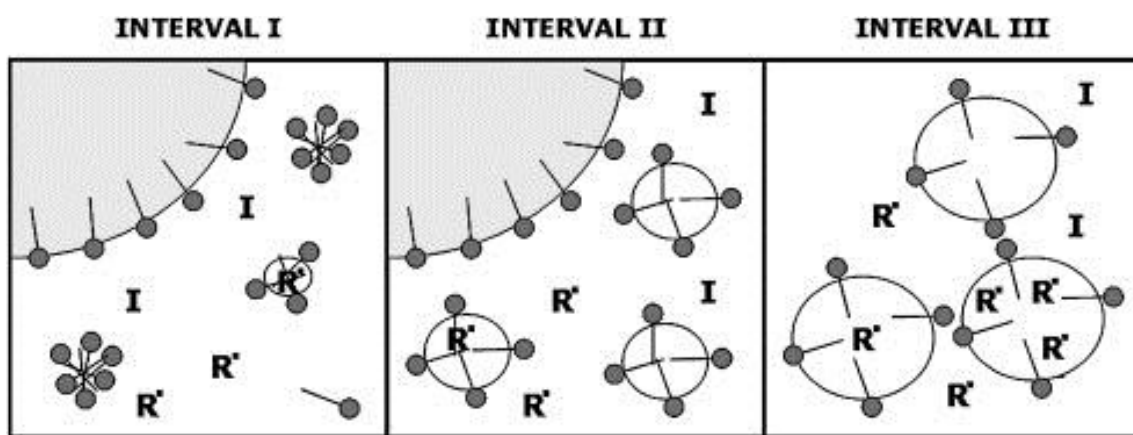


**Fig. 2.5.** The schematic diagram of three intervals in emulsion polymerisation.<sup>22</sup>

The polymerisation is initiated in the aqueous phase, and it leads to nucleation of particles. This step is known as interval I. Subsequently, the particles grow in the stable colloidal dispersion with almost constant number density. The growth is enabled by the absorption of monomers in the aqueous phase which was applied by the monomer droplets. This step is known as interval II, and the rate of polymerisation is almost constant and depends on the diffusion rate monomers into aqueous from the monomers droplets. In interval III, the monomers are gradually exhausted, and therefore the rate decreases.<sup>5</sup> The rate of polymerisation in each interval was shown in Fig 2.6.



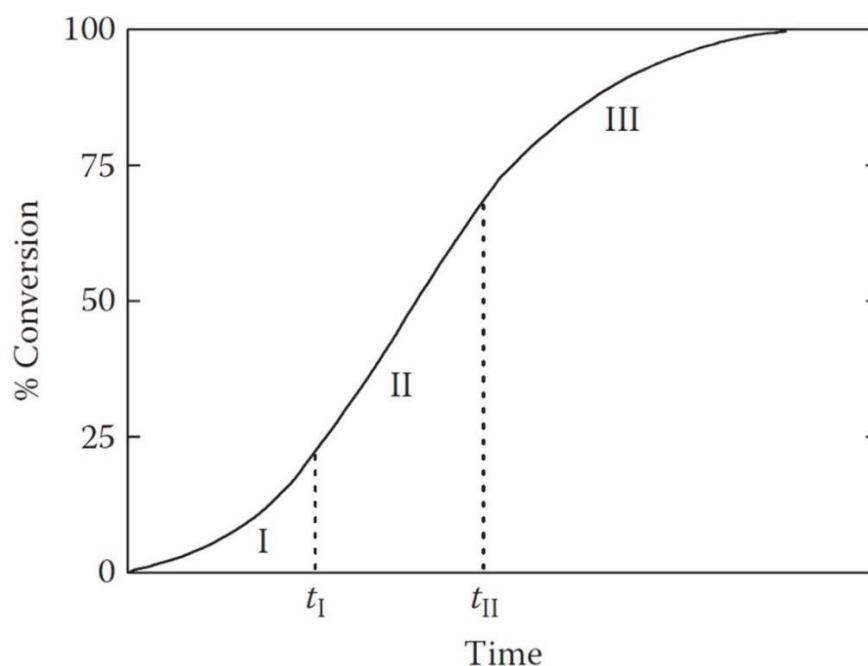


**Fig. 2.6.** Schematic diagram of conversion versus reaction time for three intervals of a classic emulsion polymerisation.<sup>5</sup>

The rate of polymerisation is affected by the solubility of monomer. When there are different monomers with distinct solubility, the distribution of segments in the copolymer is not uniform.<sup>5, 23</sup> In our case the method of Rodriguez et. al.<sup>24</sup> was used, because the MAA is more hydrophilic than EA, a seed-feed emulsion polymerisation method is used to achieve relative uniform distribution particles. This is because the growth of particles occurred under monomer-starved conditions. A small amount of particles is initially formed and stayed until the interval I was completed. Subsequently, the co-monomer mixture was introduced with constant feeding rate. Here, the feeding monomers replace the role of monomer droplets (Fig 2.2b) of classic emulsion polymerisation to provide monomers for particles growth.

#### 2.1.4 Colloidal dispersions

Colloidal dispersions are composed of a dispersed phase in a continuous medium, which is referred to the continuous phase. The dispersed phase can be particles, bubbles and foam with sizes in the range of 1 nm to 1000 nm. The dispersed particles

are moved as Brownian motions which are caused by collisions with other surrounded molecules in the medium.<sup>25</sup> It is a heterogeneous system and is widely applied in the normal life such as beer and milk. In our case, the colloidal dispersion consists of polymeric MG particles (the size is in a range of 50 - 500 nm) and the water is typically used as the continuous phase.

### 2.1.5 Colloidal stability and DLVO theory

As some colloids are prone to aggregation in the solvent, the kinetic stability of colloidal solution is worthy of consideration. The interaction between particles can be divided into an attractive force (van der Waals force) and a repulsive force (electrostatic force). The overall stability of colloidal dispersion can be described by the DLVO theory.<sup>26</sup>

#### 2.1.5.1 Van der Waals forces

The attraction between two spherical particles (see Fig. 2.7) can be explained by the analytical equation for van der Waals interaction, which is caused by attractive dipole or induced dipole interaction between particles.<sup>4, 27</sup> For ideal monodisperse spherical particles in vacuum, two particles have the same radius,  $a$ , and the distance between particles is  $H$ . The attractive interaction energy,  $V_A$ , is derived by Hamaker<sup>28</sup> in the following equation:

$$V_A = -\frac{A}{12} \left[ \frac{1}{x(x+2)} + \frac{1}{(x+1)^2} + 2 \ln \left( \frac{x(x+2)}{(x+1)^2} \right) \right] \quad (2.6)$$

Where  $A$  is the Hamaker constant and  $x = H / 2a$ .

For two approaching particles or a minuscule particle-particle separation is assumed,

$H \ll a$  or  $x \ll 1$ , the equation can be simplified as:

$$V_A = -\frac{A}{12} \cdot \frac{1}{2x} = -\frac{Aa}{12H} \quad (2.7)$$

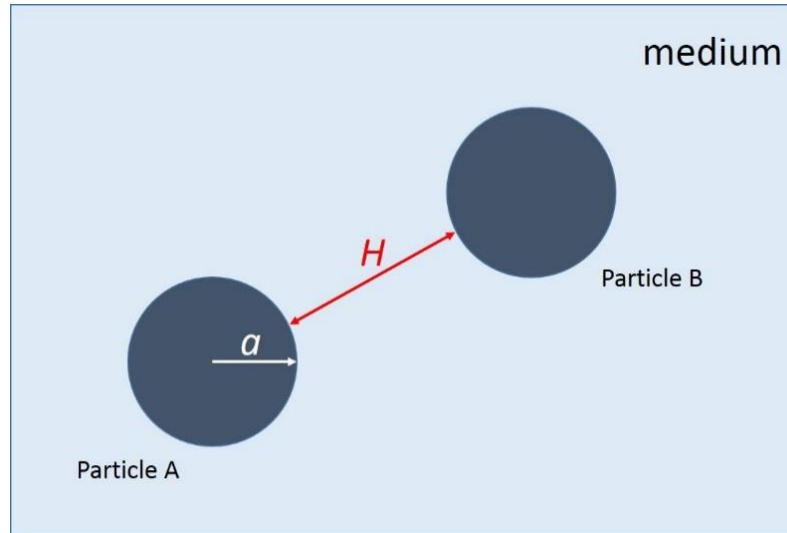


**Fig. 2.7.** Schematic diagram of two particles in the medium.

For a non-vacuum medium, the interaction between particles and medium must be considered. The Hamaker constant of particles in medium can be approximated by:

$$A = (A_1^{1/2} - A_2^{1/2})^2 \quad (2.8)$$

The  $A_1$  and  $A_2$  are the Hamaker constants for particles and medium in vacuum, respectively.<sup>27, 29</sup> Thus, for certain colloidal system the attractive force between particles only relate to the particle-particle distance.

#### 2.1.5.2 Electrostatic forces

In colloidal dispersions, two particles with surface charge can be stabilised by the electrostatic repulsive force. The repulsive force appears when one particle approaches another, and initiates from the overlap of the electrical double layers.<sup>25, 30</sup>

An electrical double layer is created by a charged surface in contact with electrolyte solution consisting of solvent molecules, co-ions and counterions.<sup>31</sup> The surface charges caused a specific structure of ions near and within the interface due to the balance of electrostatic force, which is called the electrical double layers (see Fig. 2.8).

There are two layers in the electrical double layer includes the stern layer and the diffuse layer. The inner (stern) layer consists of compact counter-ions due to the strong electronic force from the surface charge. The outer (diffuse) layer is formed by gradient accumulation of both ions and counter-ions which can be affected by either particles charge or the thermal agitation in the medium. The stern plane and shear plane in Fig. 2.8 are the boundaries of the stern layer and diffuse layer, respectively. The electrokinetic potential measured at the shear plane is called the zeta potential. The thickness of the electrical double layer is not determined by the properties of the particles but by either the properties of the medium or the electrolyte concentration in the media. For a 0.1 M 1:1 electrolyte (like NaCl) in aqueous solution at 25 °C, the thickness is about 1 nm.<sup>32-34</sup>

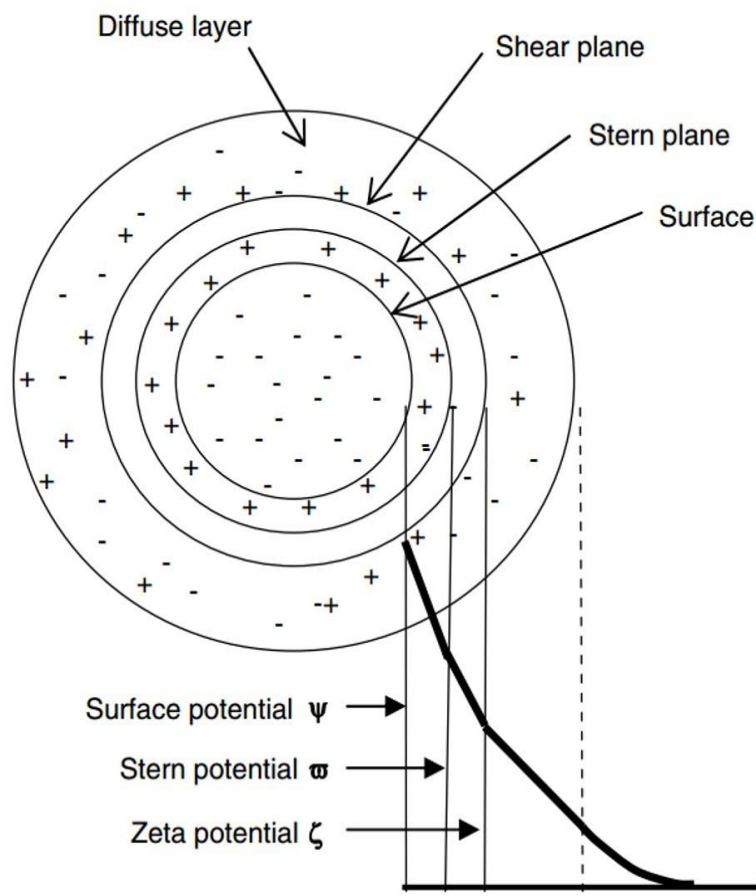


**Fig. 2.8.** Schematic diagram of different planes and potentials in double layer.<sup>35</sup>

The electrostatic repulsive potential,  $V_R$  between two same particles can be evaluated by the following equation:

$$V_R = \frac{32\pi\epsilon a k^2 T^2 \gamma^2}{e^2 z^2} \exp(-\kappa H) \quad (2.9)$$

Where  $\epsilon$  is the permittivity,  $a$  is the radius of particles,  $k$  is the Boltzmann constant,  $T$  is the absolute temperature,  $\gamma$  is a parameter of dimensionless potential.  $e$  is the charge,  $z$  is the valence,  $\kappa$  is the Debye screening Parameter and  $H$  is the distance between two particles. For two approaching particles (i.e. the electrical double layers of particles are small overlapped), the equation 2.9 can be simplified to:

$$V_R = 2\pi\epsilon a \psi_d^2 \exp(-\kappa H) \quad (2.10)$$

Where  $\psi_d$  is the potential at stern plane. The combination of attractive and repulsive forces is explained by a DLVO theory as follow.

### 2.1.5.3 DLVO theory

The DLVO theory describes a balance between the van der Waals attraction and electrostatic repulsion. This theory is developed by Derjaguin, Landau, Verwey, and Overbeek and therefore named after them.<sup>36-38</sup> The total potential energy,  $V_T$  between two particles when they approach each other can be explained by a sum of attractive and repulsive energies as mentioned in the front two sections.

$$V_T = V_A + V_R \quad (2.11)$$

The different energy potentials as a function of  $H$  is shown in Fig 2.9. There are three features can be found from the potential curve of  $V_T$  which includes a primary minimum (position D in Fig. 2.9), a primary maximum (position C) and a secondary minimum (position B). For the secondary minimum, it appears when two particles are separated by a long distance (roughly similar to particle size). For a polymer colloidal dispersion, if the depth of this minimum is large enough, flocculation may

occur in the dispersion. The height of primary maximum is also known as the potential barrier to prevent the contact of the particles. If the particles have enough energy to pass this barrier, the irreversible formation of aggregates occurs in the dispersion. For the primary minimum, the particles are separated by a short distance (molecular level), and the particles are bonded as agglomeration in the point D in Fig. 2.9. However, the colloidal dispersion can keep a long term stability if the potential at this point (C) is large than  $25 kT$ .<sup>35, 39-40</sup>

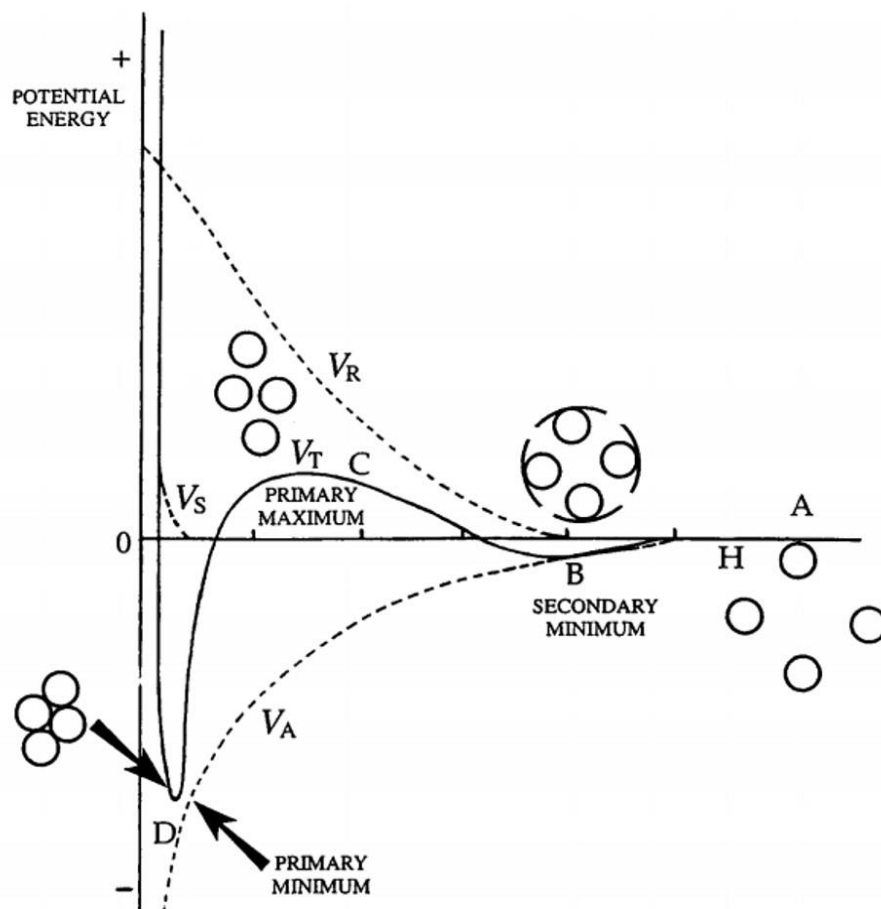


**Fig. 2.9.** Schematic diagram of potential energies versus distance of two particles.<sup>40</sup>

### 2.1.6 Stabilisation of MG particles

The stabilisation of MG particles in water is more complex than the ideal particles in DLVO theory. Because the hydrophilic polymer chains in MG particles can extend from the particles surface into water in the forms of loop or tail. The extended polymer chains prevent the agglomeration of particles which is called as “steric

effect” or “steric stabilisation”.<sup>41-42</sup> The extended polymer chains penetrate to each other when two particles are approaching. Then the repulsion is generated because of the imbalance of osmotic pressure in the overlapping area. For MG particles, the stabilisation becomes a total effect from the DLVO and the steric stabilisation. The diagram of steric repulsion is shown in Fig. 2.10 which can be divided into two types. The MG particles used in this thesis are surrounded by negative charges and therefore the electrosteric stabilisation also contributes to the increasing stability of MG dispersions. Moreover, to a first approximation the repulsion can also grow by the degree of MG particles swelling.<sup>43-44</sup>

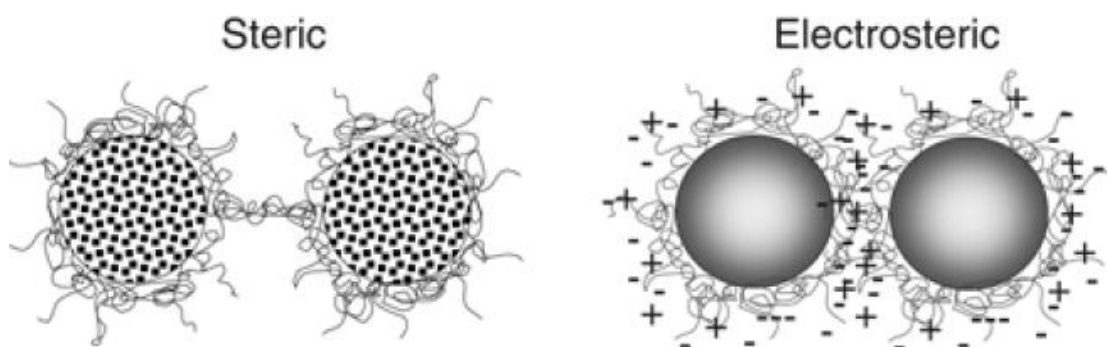


**Fig 2.10.** Schematic diagram of steric stabilisation between two MG particles.<sup>35</sup>

### 2.1.7 The pH-responsive microgels

The responsive MG is a type of particles which the swelling and de-swelling behaviours of MG are in responsive of environment stimuli.<sup>45</sup> The response can be triggered by temperature,<sup>46</sup> pH,<sup>47</sup> light<sup>48</sup> or enzymes.<sup>49</sup> Therefore, they are called as “smart” materials and applied as “intelligent polymer therapeutics” in biomedicine applications.<sup>50-51</sup> The pH-responsive MG can be defined as crosslinked polymer particles that can swell when the pH approaches their  $pK_a$ .<sup>52</sup> In general, some segments of pH-responsive MG particles are polyelectrolytes structures including weak acid or base or both groups. These structures can be ionised by releasing or

absorbing protons from solution.<sup>53</sup> Because of the ionisation, the polymer chains with the same charge are repulsive with each other. As a result, the chains are expanded which lead to the size or structures of MG particles can be changed in responsive to environmental pH.<sup>54</sup> In our case, the swelling of poly(EA/MAA/*x*) MGs is caused by the MAA segments. The dissociation of MAA groups in aqueous solution is based on their carboxyl groups:



The MAA type MGs swell with increased pH near to the  $\text{pK}_a$ . Other types of MGs like PVAM MG, which contain amine groups can swell with decreased pH.<sup>55</sup> Beyond the critical gelation concentrations, the physical gel can be formed at physiological pH. These gels are believed to be suitable for soft tissue engineering application<sup>56-57</sup> such as degenerated intervertebral disc repair (IVD)<sup>58</sup> because of their similarity to biological tissues. In addition, the networks expanding and condensing of particles are widely applied as drug carriers<sup>59</sup> or rate controlling barriers<sup>60</sup> in drug delivery systems.<sup>61</sup> Considering so many applications are achieved by the pH-responsive system, the crucial parameters and mathematic modelling of swelling equilibrium are important to be mentioned.

## **2.1.8 The swelling of microgel particles**

### **2.1.8.1 Swelling ratio**

For responsive MGs, the most important parameter to characterise the swelling process is the volume swelling ratio,  $Q$  which represents how much solvent can be absorbed by swelling particles. It can be calculated by the ratio of gel volume in swollen state,  $V_s$  and the volume in the collapsed state  $V_c$ , or by the cubic of



swelling/collapsed ( $d_h / d_c$ ) particle diameter ratio. The  $\varphi_2$  is the volume fraction of polymer in a swelling particle.

$$Q = \varphi_2^{-1} = \frac{V_s}{V_c} = \left(\frac{d_h}{d_c}\right)^3 \quad (2.13)$$

As mentioned above, the fluid to gel transformation can be achieved by increase pH of the MG dispersion to gel. In experimental work, we are using the ratio of diameter, not the volume ratio to examine the ability of MG particle swelling. Because when the particles in concentrated MG dispersion swell, the swelling particles nearly fill all of the space in dispersion and the individual particle is trapped in steric confinement which cannot reach its fully swelling volume. The diameter of particles can be examined by DLS measurements or electron microscopy. However, the limitation of DLS measurement is that the hydrodynamic diameter of collapsed particles is not accurate because the polymer particles still can absorb some solvent molecules in dispersion. For the electron microscopes, both SEM and TEM require a dried sample so the swelling particles cannot be measured. Besides, the deformation of particles during drying process also needs to concern. According to the past works of our group, the values of  $Q$  are in the range of 10 – 100.<sup>62-64</sup>

#### 2.1.8.2 The theoretical background of swelling

The mixing process of swelling polymers in solvent can be described by the Flory-Rehner theory: the free enthalpy changes during the networks swelling,  $\Delta G$  is contributed by the free enthalpy of mixing polymer into solvent,  $\Delta G_{mix}$  and the free enthalpy of elasticity attributed to elastic deformation of polymer networks,  $\Delta G_{el}$ .<sup>65-66</sup>

$$\Delta G = \Delta G_{mix} + \Delta G_{el} \quad (2.14)$$

Therefore, the swelling equilibrium can be described as a balance of osmotic pressure or an osmotic equilibrium. The swelling pressure,  $\pi_{res}$  is the sum of two

opposite forces: the osmotic pressure,  $\pi_{mix}$  and the elastic response force from networks,  $\pi_{el}$ .<sup>66</sup>

$$\pi_{res} = \pi_{mix} + \pi_{el} \quad (2.15)$$

When the polymer networks are in the swelling equilibrium, the value for  $\pi_{res}$  is zero. Then the chemical potential inside and outside the particles is equal. For pH-responsive MG particles, the repulsion from ionised polymer chains should be considered. The force of ionisation,  $\pi_{ion}$  mainly depends on the degree of ionisation (increased by pH) and the ionic strength in solution. So the equation 2.14 and 2.15 can be modified to:<sup>66</sup>

$$\Delta G = \Delta G_{mix} + \Delta G_{el} + \Delta G_{ion} \quad (2.16)$$

$$\text{And } \pi_{res} = \pi_{mix} + \pi_{el} + \pi_{ion} \quad (2.17)$$

The  $\pi_{mix}$  can be calculated by the Flory-Huggins equation:<sup>66</sup>

$$\pi_{mix} = -\frac{N_A k T}{v_1} [\phi + \ln(1 - \phi) + \chi \phi^2] \quad (2.18)$$

Here, the  $N_A$  is the Avogadro constant,  $k$  is the Boltzmann constant,  $T$  is the absolute temperature.  $v_1$  is the molar volume of the solvent,  $\phi$  is the volume fraction of polymer and  $\chi$  is the Flory-Huggins interaction parameter. The  $\chi$  value is an important parameter demonstrating the interaction of polymer and solvent which depends on the temperature and polymer concentration. A low value for  $\chi$  indicates a strong interaction between polymer and solvent.<sup>66-67</sup>

The  $\pi_{el}$  can be expressed as:<sup>66-67</sup>

$$\pi_{el} = \frac{N_c k T}{v_0} \left[ \frac{\phi}{2\phi_0} - \left( \frac{\phi}{\phi_0} \right)^{\frac{1}{3}} \right] \quad (2.19)$$

The  $N_c$ ,  $v_0$  and  $\phi_0$  stands for the effective number of chains, molar volume of the polymer and volume fraction of polymer without solvent. In ideal state,  $\phi_0$  is equal to 1, so

$$Q = 1 / \phi \quad (2.20)$$

The ionic contribution to osmotic pressure is complex as they can be divided into two parts including the repulsion from the counter ion in polymer chains and the effect from the electrolytes in the solvent.<sup>68</sup> The  $\pi_{ion}$  can be expressed as:<sup>68</sup>

$$\pi_{ion} = RT[\Phi \sum_i C_i' + \phi_1 \sum_i C_i] \quad (2.21)$$

Where the parameter  $R$  is the gas constant,  $\Phi$  and  $\phi_l$  are osmotic coefficient for gel phase and solvent.  $C_i$  and  $C_i'$  are the concentration of ions in the solution and insides the swelling networks. The  $\Phi$  value is related to the polyelectrolytes from polymer in the solution. If only considering the ions from polymer chains, the  $\pi_{ion}$  can be expressed as:

$$\pi_{ion} = \frac{f_e N_c kT}{v_0} \left( \frac{\phi}{\phi_0} \right) \quad (2.22)$$

Where  $f_e$  is the number of counterions per chain.

So in the equilibrium gel swelling state (i.e.  $\pi_{res} = 0$ ), it is possible to combine equation 2.18, 2.19, 2.20 and 2.22 as follow:<sup>66-68</sup>

$$\phi + \ln(1 - \phi) + \chi\phi^2 - \frac{N_c v_1}{v_0} \left[ (f + 0.5)\phi - \phi^{\frac{1}{3}} \right] = 0 \quad (2.23)$$

In equation 3.23, the swelling ratio  $Q$  ( $= 1/\phi$ ) for an equilibrium state can be calculated. In summary, the forces from osmotic pressure, elastic networks and electrostatic balance are main forces to govern the swelling process of crosslinked particles.

### 2.1.8.3 Experimental data for swelling of microgels.

The swelling of pH-responsive microgels can be triggered by the dissociation of anionic or cationic groups in the polymer chains. When the pH approaches the  $pK_a$  of

polyelectrolytes in particles, the strong force from ionisation, the osmotic equilibrium causes the particles sensitively to swell. For anionic MGs containing carboxylic groups (-COOH), they can be ionised at high pH. For example, the first work of poly(EA-*co*-MAA-*co*-BDDA) was reported by Rodriguez et al. at 1994.<sup>24</sup> A volume swelling ratio of 110 at pH 8 in water was reported by Saunders et al. for this type of MG.<sup>52</sup> A study from Lally et al.<sup>69</sup> compared poly(EA-*co*-MAA-*co*-BDDA) MG to poly(MMA-*co*-MAA-*co*-EDGMA) MG. The result showed that the particles had a big difference in swelling ratio even when they have similar contents of MAA groups. The results supported that the swelling properties of MG particles do not only depend on the ionisation of polyelectrolytes in chains but also affected by elasticity and structure of polymer chains. For the cationic MG, in general the pH-triggered swelling is achieved by the amine groups so that the particles size increase with the decreased pH. The factors that are controlling the swelling behaviours of particles are as same as that for anionic MGs. The poly(2-vinylpyridine-*co*-styrene) particles are a typical example of this MG style, whose swelling occurred at low pH.<sup>70</sup>

The ionic strength can significantly affect the swelling process of MGs. The PNIPAM MG particles are obviously fluctuated by different electrolytes concentration which is reported by Daly et al.<sup>71</sup> At a relative low concentration of salt, the particles are collapsed due to the dehydration of polymer chains. Tan et al.<sup>72</sup> reported that the particles size of pH-responsive poly(EA-*co*-MAA-*x*) MG decreased by the increasing concentration of salt. It also reported that the solvent contains different counter-ions have complex behaviours. For example, if the MG swells in a solvent containing both K<sup>+</sup> and Na<sup>+</sup> ions, some K<sup>+</sup> ions prefer to penetrate into the porous MG particles and some Na<sup>+</sup> are expelled,<sup>72</sup> because the association of ions to

the MGs are affected by the electrolyte polarisation.<sup>73</sup> In our case, the swelling process of poly(EA-co-MAA-co-BDDA) MGs is controlled by all of the environmental conditions mentioned above which were reported by Rodriguez.<sup>24, 74</sup> The pH and ionic strength sensitive swelling process of this particles are shown in Fig 2.11a and b, respectively.

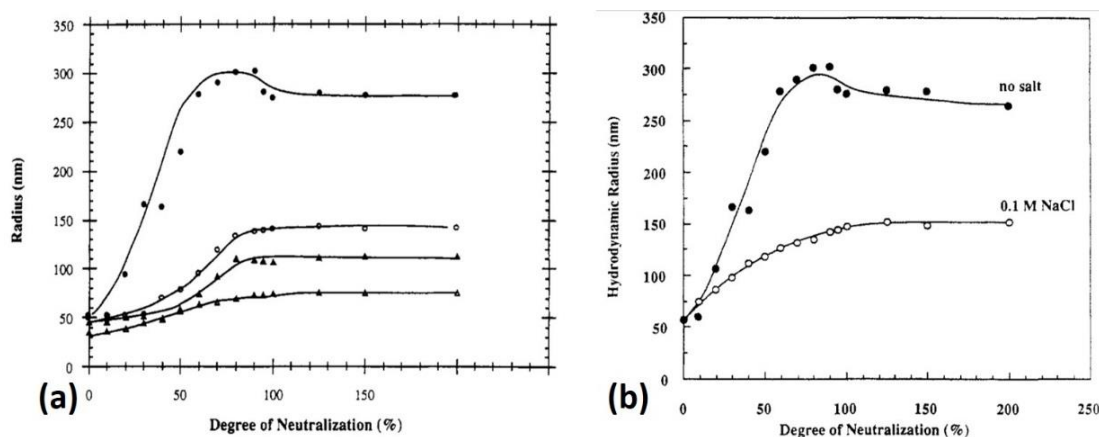


**Fig 2.11.** (a) Dependence of microgel size on neutralisation and crosslinker contents. The curves from top to bottom correspond to crosslinker contents from low to high. (b) Dependence of microgel size on degree of neutralisation and salt concentration.<sup>24</sup>

### 2.1.9 The gel networks of pH-responsive doubly crosslinked microgels

The doubly crosslinked microgel (DX MG) hydrogels are of particular interest for biological tissue engineering or biomedicine applications because their similarity to tissues.<sup>75</sup> Conventional hydrogels are normally crosslinked in bulk to form the macroscopic gels. They are easy to make but are generally not suitable for formation in vivo. In this thesis, we used the doubly crosslinked (DX) MGs which were formed by the covalent interlinking of swollen crosslinked MG particles.

#### 2.1.9.1 Mechanism of pH-responsive doubly crosslinked microgels.

The pH-responsive DX MGs were first reported by Liu et al.<sup>62</sup> The term “doubly crosslinked” is used to describe and distinguish two types of crosslinking: the intra-crosslinking of particles provide a spherical internal networks and particles here are

termed as singly crosslinked particles. When particles come into contact (i.e. swelling), inter-crosslinking can be achieved to form external covalent intra-linking between particles via a free-radical reaction between vinyl groups on particles surfaces. Thus, they are called DX MG particles. The mechanism of the DX process is shown in Fig. 2.12.

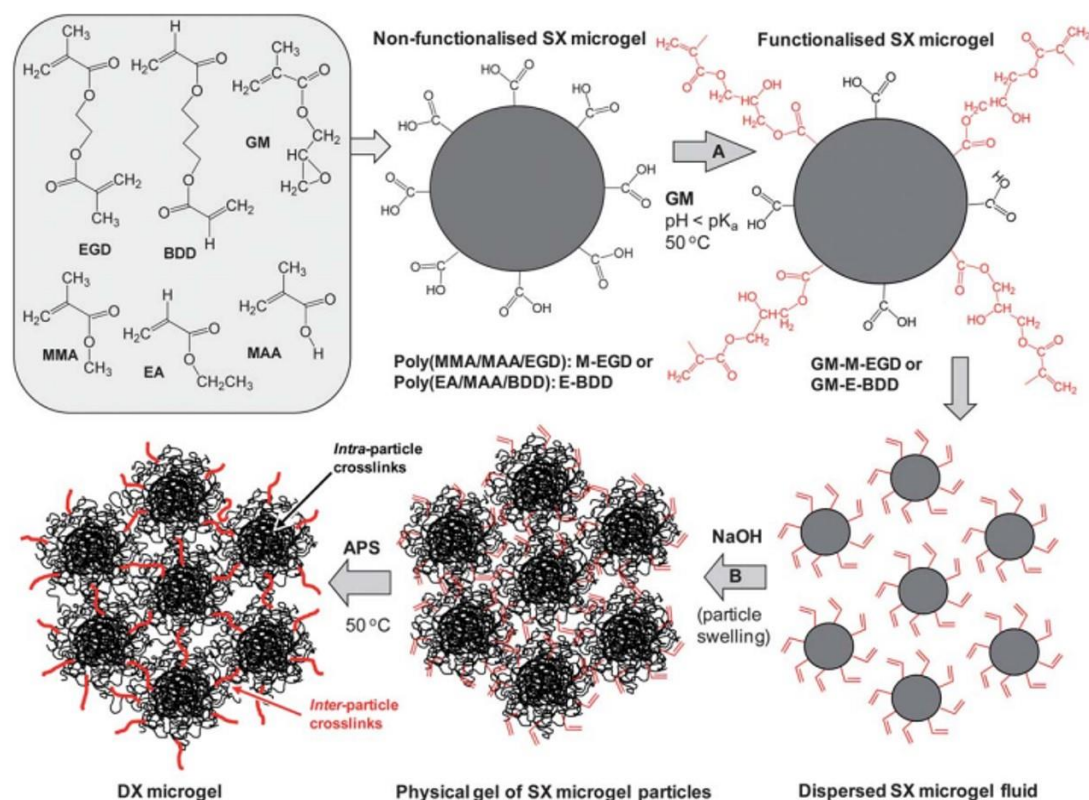


**Fig. 2.12.** The schematic diagram of DX gels formation. Step A is the surface of MG particles modified by vinyl groups. Step B is the particles swelling and contact. The final step is the formation of DX MGs.<sup>62</sup>

The main advantage of this DX gel system is that there is no extra small molecule (monomer or crosslinker) needed during the covalent macroscopic gel formation. The irreversible DX process provide the possibility for an injectable dispersion to form a load bearing gel in vivo for damaged soft tissues.<sup>76</sup>

### 2.1.9.2 Other architectures of microgel networks

As shown in the above section, the macroscopic gel can be achieved by the pH-triggered swelling following covalent linking of MGs in contact. There are also some

other methods to form the microgel networks such as microgel-mediated crosslinking, and physical microgel entrapment as shown in Fig. 2.13.<sup>77</sup> For the microgel-mediated crosslinking, this method is proposed to give gels with high mechanical performance by using microgel particles and the crosslinkers. The crosslinkers can form polymer chains between particles. The method using MG particles as building blocks and connected by additional crosslinkers was first reported by Hu et al.<sup>78</sup> The physical microgel entrapment method is usually applied in preparing hydrogel/microgel composites which the microgel particles are trapped in the secondary networks of hydrogels. Because the formation of hydrogel and microgels is independent, this method is generally used to design gels with special morphologies and mechanical properties that the migration of MGs is prevented by bulk hydrogel networks and the MGs particles are able to hide within hydrogels.<sup>79</sup> The PAMPS-PAAm double networks gel with super tough property is an example of this method.<sup>80</sup>

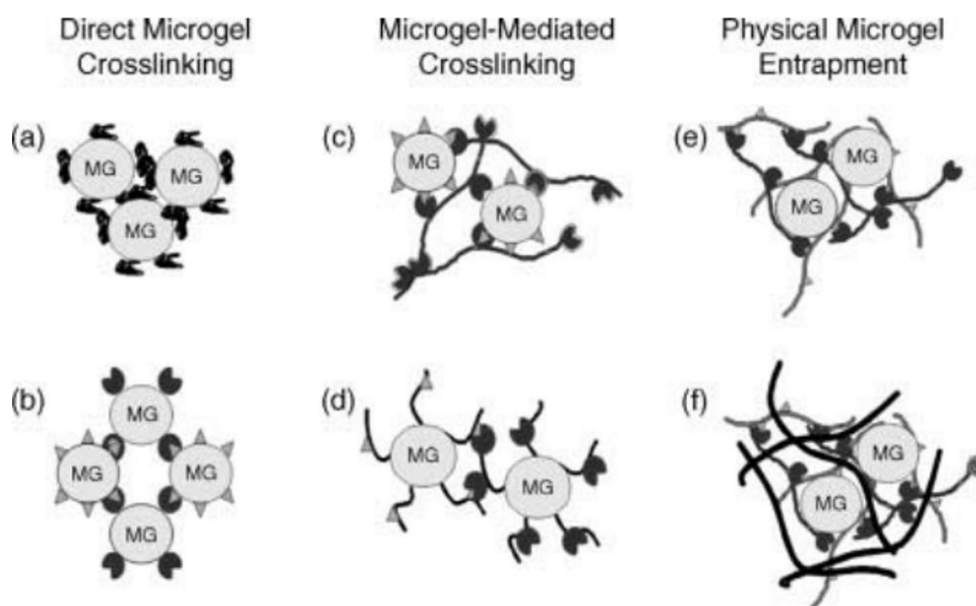


**Fig 2.13.** The formation of microgel networks by direct contact ((a) and (b)), microgel-mediated crosslinking ((c) and (d)) and physical microgel entrapment ((e) and (f)).<sup>77</sup>

## 2.2 Nanocomposites hydrogels

### 2.2.1 Nanocomposite strategy

Hydrogels are soft, high water content, multifunctional materials whose resemblance of nature living tissue makes them particularly suitable for biomedical applications.<sup>81</sup> Therefore, hydrogels are particularly suitable for use as a soft matrix in nanocomposites design. Hydrogels built using polymeric networks have their limitations. Two important factors for a hydrogel networks are the number of crosslinking junctions per unit volume and the average molecular weight,  $M_c$  or chain length between two junctions. In general, the increase of junctions will cause a decrease of  $M_c$  when preparing hydrogels.<sup>82</sup> Besides, the distribution of crosslinking cannot be homogeneous in real cases and becomes less uniform with higher crosslinking density. These facts cause relative weak performances in optical transparency and mechanical properties.<sup>82-83</sup> The lack of responsive properties of crosslinking networks is also reported by Xiang et al.<sup>84</sup> The development of composites strategy makes it possible to combine special properties from two or more materials into a single material. Therefore, many works have been done to improve the properties of hydrogels by using nanocomposites. Nanocomposite hydrogels are crosslinked polymer networks prepared in aqueous solution in the presence of nanometre-level fillers such as nanoparticles or nanofibers.<sup>85</sup> In general, it can be seen as nano-reinforcements distribute in the polymer networks(as the matrix). The introduced nano-reinforcements can be used as a function of crosslinker, attaching the polymer chains or introducing new properties to the hydrogel. The most common purpose for nano-reinforcements is to increase the modulus or ductility. Other properties of interest include thermal, electrical, optical, magnetic behaviours.<sup>86</sup> This technique for preparing novel nanocomposite hydrogels



leads to applications in the electronics, biosensors, wound-healing, catalysis, tissue engineering, drug delivery and other bio-engineering areas.<sup>85, 87-88</sup>

## 2.2.2 Hydrogels containing graphene oxide

### 2.2.2.1 The structure of graphene oxide

Graphene oxide (GO) is a 2D material composed of a parent graphene backbone and oxygen functional groups (see Fig. 2. 14).<sup>89</sup> Most of the synthesis methods for GO use chemical exfoliation of graphite powders with strong oxidising agents.<sup>90</sup> The history of studying GO started about 150 years ago. GO is well known for its excellent mechanical, thermal and electrical properties. Following the discovery of graphene at Manchester at 2004,<sup>91</sup> GO became one of the hottest topics in materials science. GO was widely studied in polymer composites, semiconductor sensors, biomedical applications, paper-like materials etc.<sup>92-93</sup>

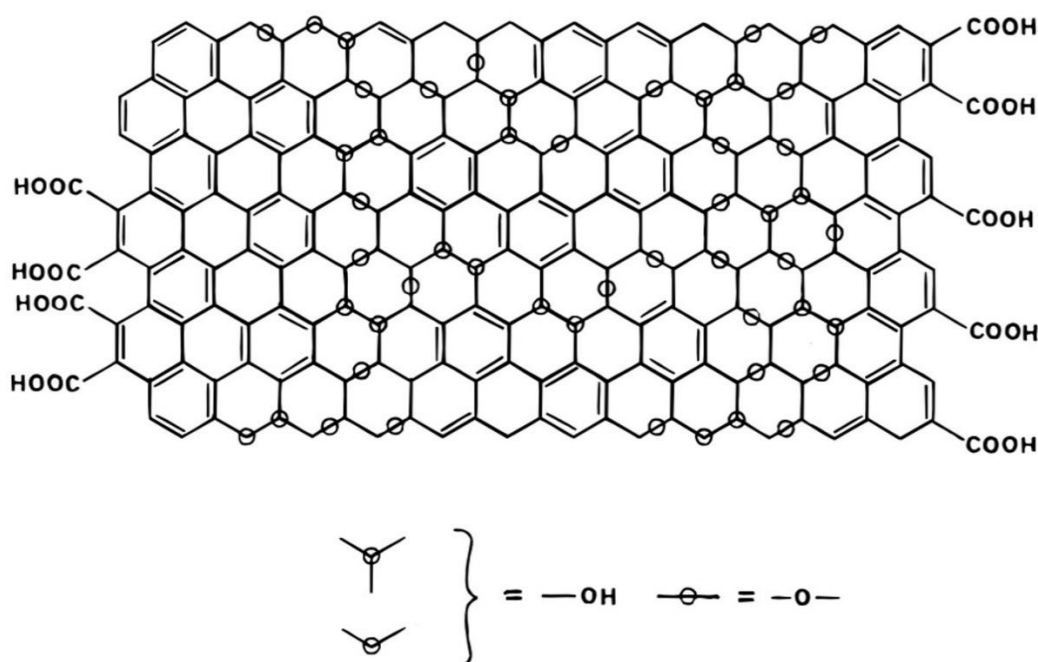


**Fig 2.14.** The structure of graphene oxide.<sup>94</sup>

A simple description of the structure of GO is graphene layers with oxygen groups on the surface. The exact structure of GO is still controversial.<sup>93</sup> There are many early studies on models for the structure of GO. The Lerf and Klinowski's model

(Fig. 2.14) which is the most widely used model to understand the structure of GO.<sup>94</sup> In their model, the GO is terminated by carboxyl and hydroxyl groups, while in the central part of GO two types of structures exist including unreacted benzene rings and oxidized aliphatic aromatic six-member rings. Layers of oxygen atoms exist on the surface of GO sheet. The latter concentration depends on the degree of oxidation. The negative charges are mobile and arrange on the oxygen layers, which could disable the nucleophilic attack to the carbon atoms. Therefore, the epoxy groups on GO are chemically inactive.

Another feature of GO is the hydrogen bonding network can be built in water via oxygen groups and water molecules, which is very necessary for application in hydrogels.<sup>95</sup> The hydrogen bonding network is a factor of mechanical properties for hydrogel composite containing GO. According to the study of Medhekar,<sup>96</sup> two kinds of H-bonds exist in GO solution: the intra-layer and inter-layer H-bonds. The structure of interlayer hydrogen bonding depends on water content. With high water content, the hydrogen bonding structure is uniform, and some water clusters are formed to improve the layer to layer distance. For the intra-layer hydrogen bonding, the networks are formed from the functional groups (epoxy groups, hydroxyl group, etc.) on the GO layers.

#### **2.2.2.2 Graphene oxide enhanced hydrogels**

The structure of GO means it is easy to disperse in water, because it has lots of hydrophilic groups on the surface and edges of graphene sheets (see Fig. 2.14). The excellent elastic strength (~30 GPa), thermal and electrical properties are attracting considerable research attentions on its composite for hydrogels.<sup>97</sup> Faghihi et al.<sup>98</sup> reported that GO can reinforce the mechanical properties of poly (acrylic acid)

hydrogel for soft tissue engineering. Lu et al.<sup>99</sup> mixed NIPAM microgel particles with GO and gained a novel thermal and photo responsive hydrogel with high responsive sensitivity. A ~144% improvement of critical tensile strength for hydrogels is achieved by adding only 0.1 wt.% of GO which is reported by Huang et al.<sup>100</sup> It is noteworthy that many of hydrogel/GO composite gels are reported as biocompatible materials.<sup>101</sup> Thus, the large and highly reactive surfaces of GO also can be used to transport and deliver medicine or DNA in nanocomposites hydrogels.<sup>102</sup>

### **2.2.3 Hydrogels contain carbon nanotubes**

#### **2.2.3.1 The structure and properties of carbon nanotubes**

The structure of carbon nanotubes (CNTs) is less complicated to understand compared with GO. It only consists of carbon atoms and can be imagined as rolled-up graphene sheets.<sup>103</sup> Two types of CNTs are termed base on the number of layers in one tube including multi-wall carbon nanotubes (MWNTs) and single-wall carbon nanotubes (SWNTs) (see Fig 2.15a). The first observation of MWNTs is by Iijima at 1991.<sup>104</sup> A TEM image of a MWNT is shown in Fig. 2.15b and the rolled-up structure is shown in the inset. Typically, the diameters of SWNTs are about 0.8 – 2 nm and for MWNTs about 5 - 20 nm.<sup>105</sup> The lengths for CNTs are diverse which depend on the synthesis process, the most common length used in research are from several nanometers to tens of microns. The longest CNT at present is about 550 mm.<sup>106</sup> Because of their special structure, CNTs are considered as materials with high aspect ratio and extremely high surface area.

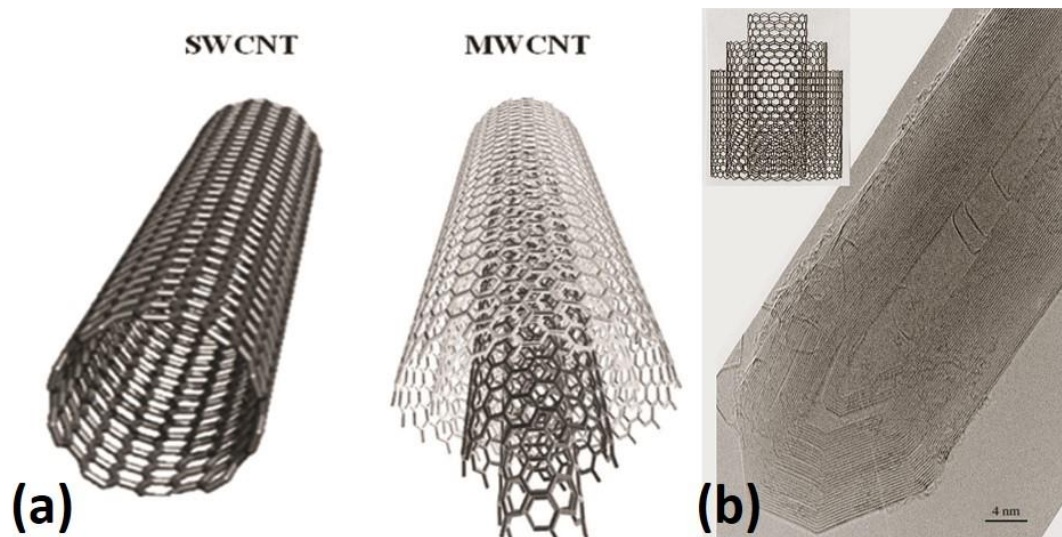


**Fig 2.15.** (a) The structures of SWNT and MWCNT. (b) The high resolution TEM image of MWNT. The inset shows the structure of MWNTs.<sup>103, 107</sup>

### 2.2.3.2 The applications of carbon nanotubes in nanocomposites hydrogels

The most attractive property of CNTs is their mechanical properties. In the axial direction, MWNTs are reported to have about 1 TPa of elastic modulus and 100 GPa of tensile strength.<sup>108</sup> Besides, the CNTs are widely used to introduce electrical properties to hydrogels. The conductivity of CNTs depends on their quality. In general, the MWNTs can be seen as conductive or semi-conductive materials while the SWNTs are mostly semi-conductive. Without considering the impurity and the defects on the wall, an individual SWNT is reported to have a thermal conductivity of  $3500 \text{ W m}^{-1} \text{ K}^{-1}$  at room temperature.<sup>105</sup> Therefore, the high mechanical strength, conductive properties, low mass density, very high surface area of CNTs are widely used in nanocomposites hydrogels. However, there are also several limitations of CNTs in biomaterials studies. Firstly, the CNTs are hydrophobic which could form large agglomerations in the water or hydrogels. Secondly, the strong van der Waals interaction made them difficult to disperse in the hydrogel in preparing process. Finally, the needle-like structure made them toxic in the human body. Fig. 2.16 shows the main applications for the CNTs nanocomposite hydrogels such as bio-

sensing, soft tissue engineering and biomedicine applications etc.<sup>109</sup> For example, Zhang et al.<sup>110</sup> reported pH-responsive PMMA/MWNTs composite hydrogels have a microporous structure which can be used in drug delivery. They functionalised the MWNTs with –COOH groups to improve the solubility. PAM/MWNTs hydrogels were introduced by Sudha et al.<sup>111</sup> The mechanical properties, electrical properties and thermal stability of gels were significantly increased by the MWNTs. Another important discovery for CNTs contained hydrogels is that the toxicity and carcinogenicity of CNTs was significantly reduced when the CNTs were trapped in hydrogel networks.<sup>112</sup> Because the hydrogel networks can prevent either the aggregate process of CNTs or the exposure of the needle-like structure. In our case, the MWNTs are ideal to composite with MG particles to improve the modulus and the electrically conductivity, so the application of DX MGs can in principle be expanded to electro-responsive materials<sup>113</sup> such as biosensing<sup>114</sup> and electronic skin.<sup>115</sup>

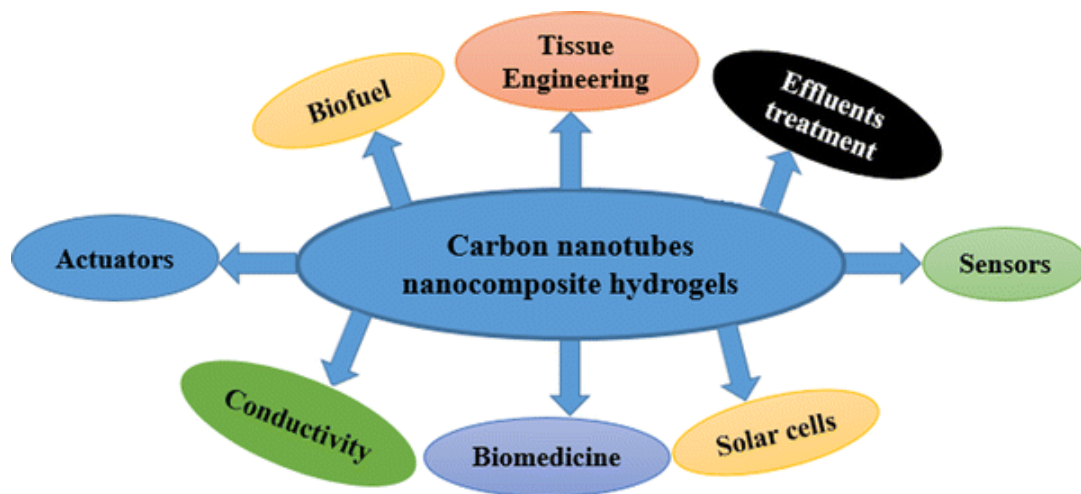


**Fig. 2.16.** The application of carbon nanotubes nanocomposites hydrogels.<sup>109</sup>

## 2.2.4 Mechanical properties of composites

To study the mechanical properties of nanocomposite hydrogels, the factors to describe compositions are generally used the volume fraction,  $\phi$  and the modulus,  $E$ . For two components composites, the composites can be idealised and simulated as a mixture of uniform matrix and continuous fibres. There are two geometry possibilities to study the modulus of a composite as shown in Fig. 2.17, which are the isostrain model and the isostress model.<sup>116</sup>

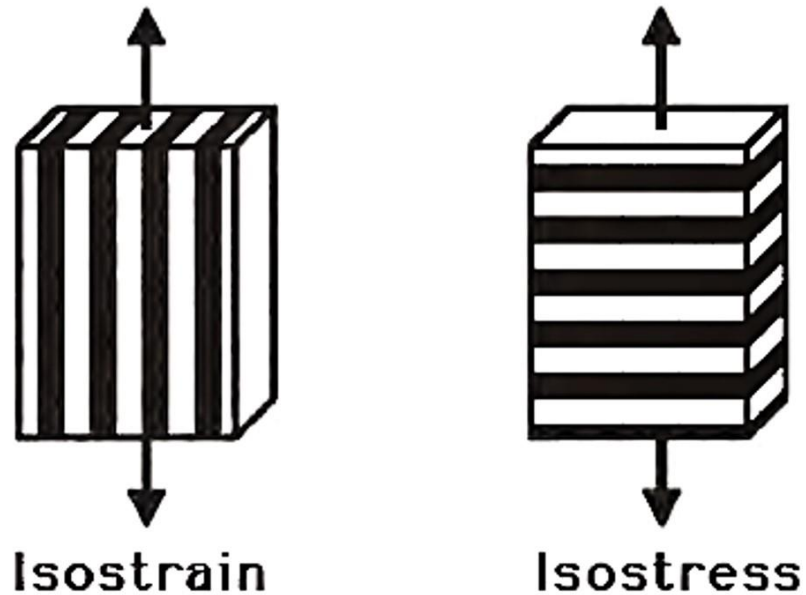


**Fig. 2.17.** The schematic diagram of isostrain and isostress conditions.

### 2.2.4.1 The isostrain condition

The isostrain condition assumes the strain on the reinforcement, and the matrix are equal, so this condition can be expressed as below with a further assumption that both reinforcement and matrix behave fully elastic. Therefore,

$$\varepsilon_c = \varepsilon_m = \varepsilon_r \quad (2.21)$$

Where  $\varepsilon_c$ ,  $\varepsilon_m$  and  $\varepsilon_r$  represent the strain on the composite, matrix and reinforcement, respectively.

So the stress of the matrix,  $\sigma_m$  and reinforcement  $\sigma_r$  can be expressed as:

$$\sigma_m = E_m \varepsilon_m \quad \text{and} \quad \sigma_r = E_r \varepsilon_r \quad (2.22)$$

The  $E_m$  and  $E_r$  are their moduli.

Under the condition of isostrain, the total stress on the composite is the sum of stress applied on the matrix and the reinforcement. So the total stress can be expressed as:

$$\sigma_c = \phi_m \sigma_m + \phi_r \sigma_r = \phi_m E_m \varepsilon_m + \phi_r E_r \varepsilon_r \quad (2.23)$$

The  $\phi_m$  and  $\phi_r$  are the volume fractions and

$$\phi_m + \phi_r = 1 \quad (2.24)$$

So the overall modulus of the composite,  $E_c$  can be expressed as:

$$E_c = \phi_m E_m + \phi_r E_r$$

$$\text{or } E_c = \phi_m E_m + (1 - \phi_m) E_r \quad (2.25)$$

#### 2.2.4.2 The isostress condition

The isostress condition describes the applied stress is perpendicular to the axial direction of reinforcement, also when the hard reinforcements are discrete in a soft matrix. Under this condition, the stress is uniform.

$$\sigma_c = \sigma_m = \sigma_r \quad (2.26)$$

So the strain of each composition under elastic deformation can be expressed as:

$$\varepsilon_m = \sigma_m / E_m \quad \text{and} \quad \varepsilon_r = \sigma_r / E_r \quad (2.27)$$

The overall strain in the direction of applied force is the sum of strain in each composition.

$$\varepsilon_c = \phi_m \varepsilon_m + \phi_r \varepsilon_r \quad (2.28)$$

So the modulus of the composite can be expressed as:

$$\frac{1}{E_c} = \frac{\varepsilon_c}{\sigma_c} = \frac{\phi_m \varepsilon_m}{\sigma_m} + \frac{\phi_r \varepsilon_r}{\sigma_r} = \frac{\phi_m}{E_m} + \frac{\phi_r}{E_r} \quad (2.29)$$

Rearranging equation 2.24 gives:

$$E_c = \frac{E_m E_r}{E_m \phi_r + E_r \phi_m} \quad (2.30)$$

### 2.2.4.3 Comparison of isostress and isostrain conditions

For most nanocomposites hydrogels, the modulus of reinforcement is much higher than the hydrogel matrix (i.e.  $E_r \gg E_m$ ). Both conditions indicate that the stiffness of composite can be improved by the increase of volume fraction of reinforcement. However, the stiffness of hydrogel can be more efficiently improved by the reinforcement under isostrain condition as shown in Fig. 2.18. In most cases, the situations of nanoparticles in hydrogels are more complex which may not perfectly fit either condition. However, these two are still used as the main predictors of stress-strain distribution in hydrogels and to understand the modulus of composites in terms of component concentration.<sup>117</sup>

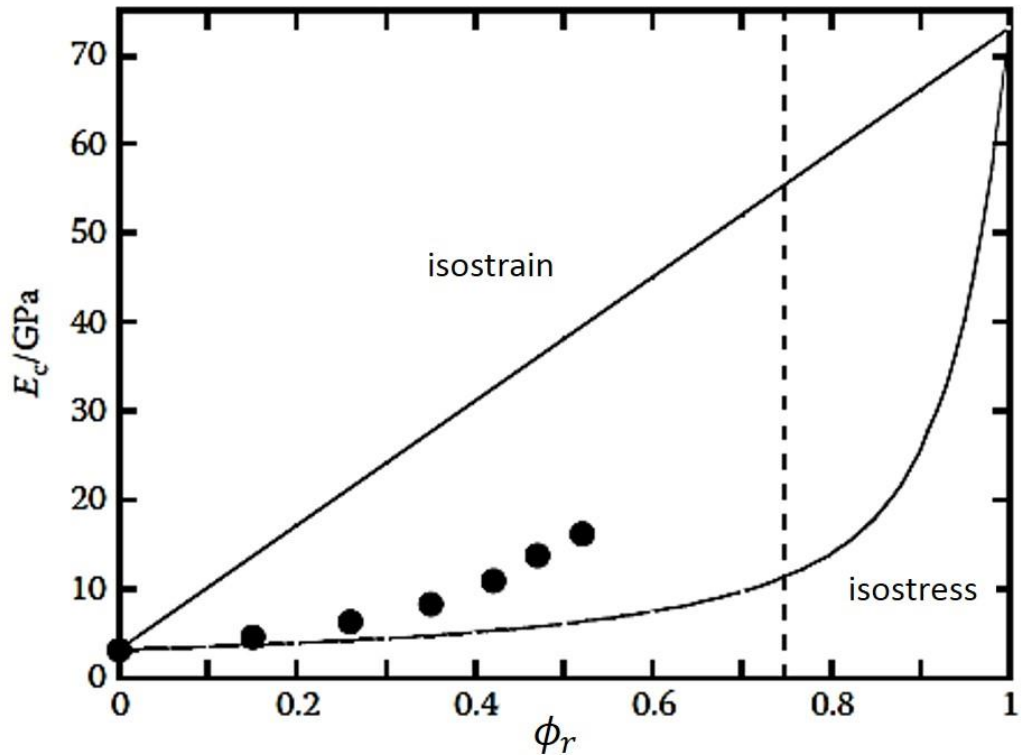


**Fig. 2.18.** The comparison of isostrain and isostress conditions. The black data points are shown a real case of an epoxy/carbon fibre composites.<sup>5</sup>



## 2.3 Instrumentation

Several characterisation techniques were performed to study the morphology, size distribution and properties of MGs, nano-fillers and their composites. The fundamental principles of frequently used techniques are outlined in this section.

### 2.3.1 Dynamic light scattering

Dynamic light scattering (DLS) is widely used for characterising the size of particles dispersed in a liquid. It is also referred to as photon correlation spectroscopy (PCS). This technique is based on measuring the intensity of scattered light by moving particles as a function of time. The particles in the solvent move in Brownian motion, which causes fluctuations of the scattered light intensity. The fluctuations can be converted to the mean translational diffusion coefficient which can be further converted to the particles size by using Stokes-Einstein equation<sup>118</sup>. Fig 2.19 shows typical set-up of a DLS instrument<sup>119</sup>. A vertically polarised laser beam is passed through the sample. The detector is fixed at a certain angle (usually at 90°), the scattered intensity was collected and transformed to electrical signals for the associated digital correlator.

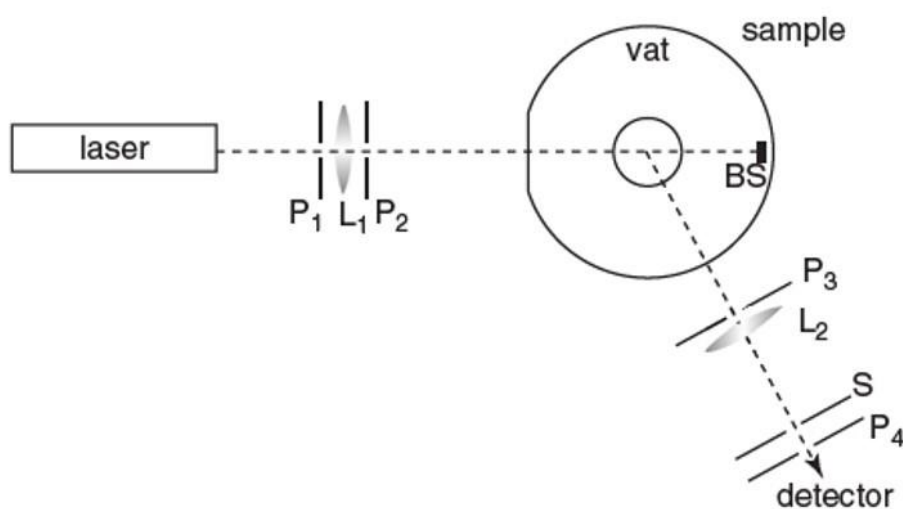


**Fig 2.19.** Scheme of the set-up for DLS instrument.<sup>119</sup>

Because the intensity is from the random Brownian motion of particles, the intensity autocorrelation was used as follows:

$$G(\tau) = \langle I(t)I(t + \tau) \rangle \quad (2.31)$$

where  $G(\tau)$  is the correlation coefficients functions,  $t$  is the time,  $I$  is the scattered light intensity at given time and  $\tau$  is the delay time of time interval.

For measuring the monodisperse particles, the  $G(\tau)$  is given by:

$$G(\tau) = A (1 + 2Be^{-\Gamma\tau}) \quad (2.32)$$

where A and B are constants.

$\Gamma$  relates to translational diffusion coefficient,  $D$  and scattering vector  $q$ :

$$\Gamma = Dq^2 \quad (2.33)$$

$q$  can be calculated by:

$$q = \frac{4\pi n}{\lambda_0} \sin \frac{\theta}{2} \quad (2.34)$$

Where the  $n$  is the refractive index of the medium,  $\lambda_0$  is the wavelength of the incident laser in vacuum and the  $\theta$  is the scattering angle.

$D$  can be related to Stokes-Einstein equation:

$$D = \frac{kT}{3\pi\eta d_h} \quad (2.35)$$

The  $k$  is the Boltzmann constant,  $T$  is the absolute temperature,  $\eta$  is the viscosity of medium and  $d_h$  is the hydrodynamic particle diameter.

In this study, DLS are used to examine the size of MG particles in various pH and therefore to study the swelling properties of particles.

### 2.3.2 Raman spectroscopy

Raman spectroscopy is a spectrum which provides the fingerprinting of molecular bond structures for sample identification and quantitation. It uses the inelastically scattered light from the photons of the molecular bond and therefore the vibration state of the molecule can be identified. Compared to other vibration spectrums, Raman spectrum does not require special sample preparation techniques; the samples can be liquid, solid or gas and they also can be placed on a transparent substrate like glass or plastic.<sup>120</sup>

In Raman spectroscopy, a monochromatic light source (a laser beam) illuminate on the sample and the scattered lights were collected. As shown in Fig. 2.20, three types of light are scattered from samples. The vast majority of the photons ( $\sim 99.9999\%$ ) are scattered in the Rayleigh scattering process as the wavelength of the incident and scattering lights are same. This is also known as the elastically scattering. The Raman scattering is the combination of the Stokes and anti-Stokes process. The intensity of each process depends on the population of the energy states in the molecule.<sup>121</sup> In low energy side, the Stokes process is stronger than anti-Stokes.

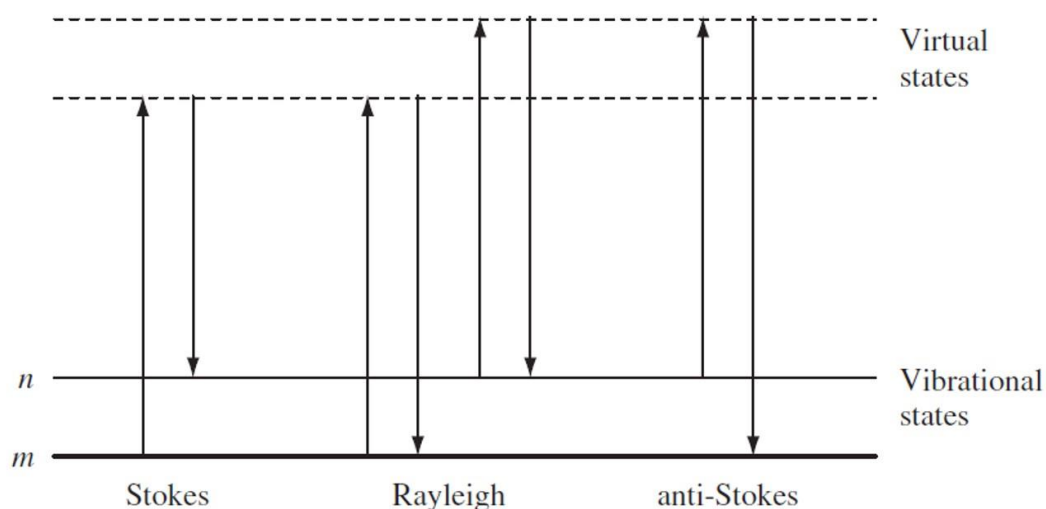


**Fig. 2.20.** Energy level diagram of Rayleigh and Raman scattering processes.<sup>121</sup>

A conventional Raman spectrometer (Fig. 2.21) contains four major components: the excitation source (the laser source); the sample illumination system and light collection optic system; the wavelength selector (Filter); the detectors and computer systems.<sup>122</sup> The main distinction of various Raman spectrometers is the wavelength range of the excitation source. In this thesis, the Raman was used to characterise the carbon nanostructures of the fillers (i.e. GO and CNTs), which are mainly composed of C-C bonds. For  $sp^2$ - $sp^2$  C-C bonds in the graphene structure, this displays a Raman band (G band) located at around  $1600\text{ cm}^{-1}$ . The  $sp^3$  carbon bonds from the defects on the GO sheets or walls of CNTs display a D band at around  $1350\text{ cm}^{-1}$  which associates with the presence of disordered carbons in the graphene structure.

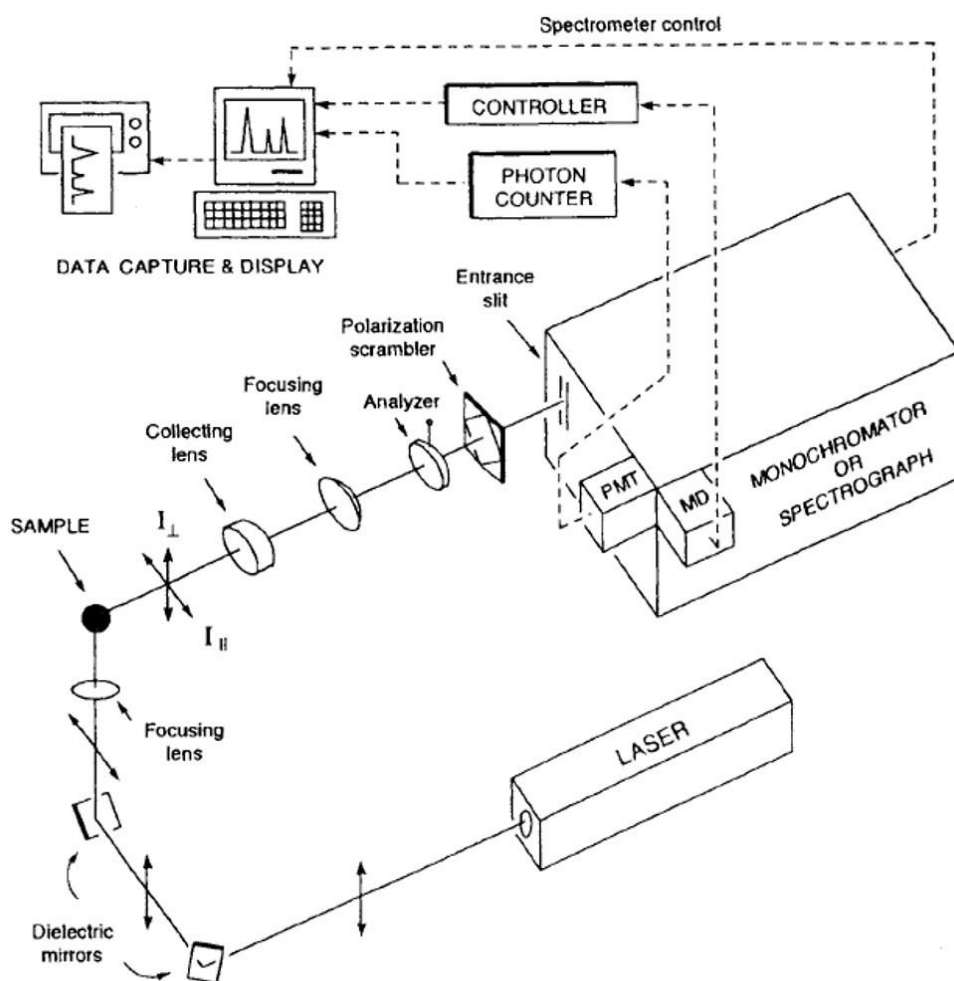


**Fig. 2.21.** A typical Raman Spectrometer.<sup>122</sup>

### 2.3.3 Dynamic rheology

Rheology is the study of deformation and flow of materials when forces are applied.<sup>123</sup> Materials are neither ideal solid nor ideal liquid exhibit both viscous and elastic behaviours. Therefore, the rheometer is used to measure the viscoelasticity of materials. Generally, it measures the stress, the applied force per area on the sample, and the strain, the infinitesimal deformation of materials. The mechanical properties of materials, the elastic modulus and the viscosity can be calculated by the stress/strain and the stress/strain rate, respectively. In the studies contained in this thesis, the rheology is studied by oscillatory dynamic rheology measurements.

If a tangential force is applied on the top surface of an ideal solid (Fig. 2.22), the shear stress,  $\sigma$  can be calculated by the ratio of force,  $F$  and top surface area,  $A$ :

$$\sigma = F/A \text{ (Pa)} \quad (2.36)$$

If the shearing velocity is  $V_0$ , the shear rate,  $D$  can be calculated by:

$$V_0 = dx/dt \text{ (m}\cdot\text{s}^{-1}\text{)} \quad (2.37)$$

$$D = dV_0/h_0 \text{ (s}^{-1}\text{)} \quad (2.38)$$

where  $h_0$  is the height of the solid.

The shear strain,  $\gamma$  can be calculated by:

$$\gamma = dx/h \quad (2.39)$$

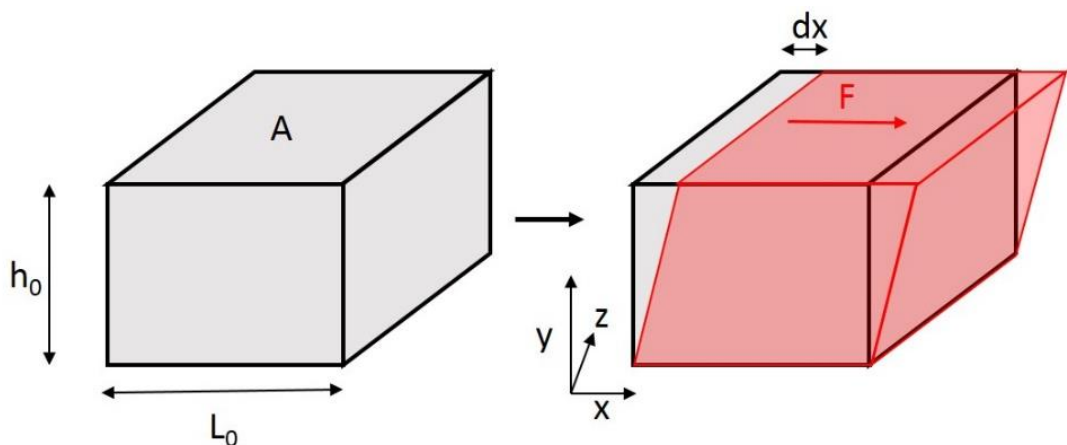


**Fig. 2.22** The shear deformation of an ideal solid.

The modulus  $G$  and viscosity  $\eta$  can be calculated by:

$$G = \sigma/\gamma \text{ (Pa)} \quad (2.40)$$

$$\eta = \sigma/D \text{ (Pa}\cdot\text{s)} \quad (2.41)$$

The dynamic rheology measurements are performed by an oscillatory rheometer which combined with a rotating plate on the top and a steady parallel plate on the bottom. It applies a sinusoidal strain on the samples:

$$\gamma(t) = \gamma_0 \sin \omega t \quad (2.42)$$

Where the  $\omega$  is the angular frequency,  $t$  is the time.

The sample can provide a stress to the rotating plate in response to the applied strain.

The responsive stress,  $\sigma(t)$  is measured:

$$\sigma(t) = \sigma_0 \sin(\omega t + \delta) \quad (2.43)$$

$\delta$  is the phase angle which depends on the response of the materials. If  $\delta$  is zero which means no lag in response, the sample is ideal elastic solid.

The modulus can be calculated with the responsive stress and applied strain by using equation 2.40 and 2.43:

$$G(t) = \frac{\sigma_0}{\gamma_0} \sin \omega t \cos \delta + \frac{\sigma_0}{\gamma_0} \cos \omega t \sin \delta \quad (2.44)$$

The storage modulus,  $G'$  and the loss modulus,  $G''$  are defined as:

$$G' = \frac{\sigma_0}{\gamma_0} \cos \delta \quad \text{and} \quad G'' = \frac{\sigma_0}{\gamma_0} \sin \delta \quad (2.45)$$

The loss tangent,  $\tan \delta$  is:

$$\tan \delta = G''/G' \quad (2.46)$$

For materials tested by oscillatory rheology measurements, the value of  $G'$  can be seen as a measure of elasticity or how much energy is stored; the values of  $G''$  can be seen as a measure of viscosity or how much energy is dissipated per unit strain. The viscoelasticity is assessed by  $\tan \delta$ .<sup>124-125</sup> For perfectly elastic networks, the value for

$\tan \delta$  is 0. When  $\tan \delta < 1$ , the sample performs more elastic behaviour than viscous. In our study, we use  $\tan \delta$  to define if a sample is a gel ( $\tan \delta < 1$ ) or a fluid ( $\tan \delta > 1$ ). The critical strain at  $\tan \delta = 1$  is the strain when the gel substantially breaks which can be used as a measure of ductility. The values for  $G'$  were used as a measure of elasticity or stiffness. Therefore, the modulus ( $G'$ ) and viscoelasticity ( $\tan \delta$ ) of SX and DX MGs can be examined over a range of frequencies and strain.

### 2.3.4 Scanning electron microscopy

Scanning electron microscopy (SEM) is one of the most popular instruments to obtain information on microstructure morphology and chemical composition of samples non-destructively.<sup>126</sup> A diagram of SEM is shown in Fig. 2.23 and showed that an electron is produced from an electron gun in the top of the column in SEM. The beam can focus on a tiny spot on the surface of specimens, and a computer can detect various of signals from the interaction between the sample and the beam. The signals include secondary electrons, backscattered electrons, Auger electrons, X-rays and perhaps light.<sup>127</sup> Subsequently, the image of specimen can be displayed on the computer screen base on the variations in brightness.<sup>128</sup> The signal of secondary electrons and backscattered electrons are the most common used for imaging because they can provide high spatial resolution and strong contrast to images. Diffracted backscattered electrons can be used for electron backscattered diffraction, it can be used to analysis the crystallography and the orientation information of the surface. The fixed wavelength of X-ray can be used for elemental analysis.

The configuration of SEM instrument includes AN electron gun, electromagnetic lenses and apertures, detecting system and deflectors. The electron gun provides and accelerates an electron beam with an energy of 1 to 30 keV in a high vacuum

environment. Subsequently, the beam is demagnified by the sets of lens and apertures to focus as a required spot with a diameter of 1 to 10 nm on the surface of the specimen. Signals are generated at a depth of  $\sim 1\ \mu\text{m}$  on the contact surface.<sup>126</sup>

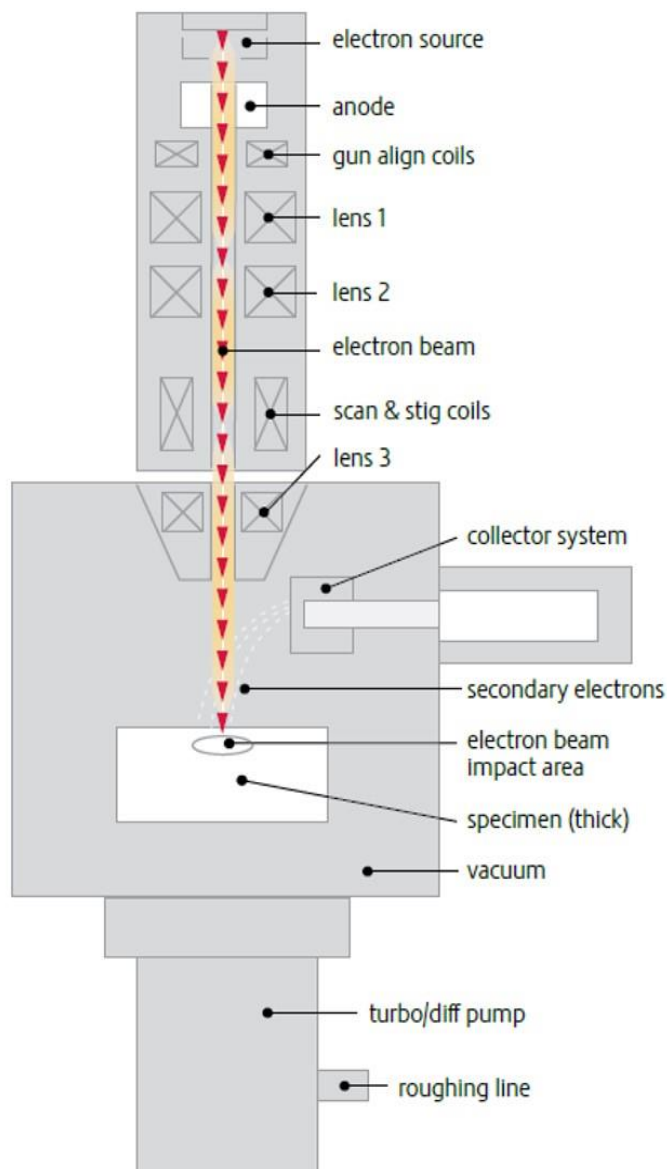


**Fig. 2.23.** Schematic diagram of the SEM.<sup>128</sup>

The aim of using SEM in this study is to observe the morphologies of samples including MG particles, CNTs, and freeze-dried SX or DX MGs. Most of our samples for SEM were polymers or contained polymer components. There are three major limitations to apply SEM on these samples.<sup>129</sup> Firstly, most of the polymers have low electron density, and hence display low contrast. Secondly, the polymers



are poor in propagating the negative charges which significantly decrease the resolution. Finally, the incident beam focused on the soft surface of samples results in a thermalised region that damages the sample surface. Therefore, all organic sample mentioned in this thesis are coated by a thin metal film (platinum or gold) to increase the conductivity. Besides, some conductive pathways (such as using silver paint) were painted to propagate the accumulated charges. Furthermore, the applied accelerating voltage in SEM was kept relatively low (3 - 10 kV) to avoid damages of sample surfaces.

### **2.3.5 Transmission electron microscopy**

Transmission electron microscope (TEM) is a directly visualised characterisation technique with ultra-high spatial and magnification, which also can be coupled with other quantitative understanding techniques.<sup>130</sup> The first TEM was built in Berlin at 1931 by Max Knoll and Ernst Ruska and was reported as not better than a light microscope. Nowadays, the resolution of TEM is consistently developed to an extraordinarily high resolution at the atomic level, and it appears in different forms of TEM such as scanning TEM, high resolution TEM and analytical electron microscope, etc. The resolution of the TEM depends on the wavelength of the beam. Since the wavelength of the electron beam from an electron gun ( $\sim 4 \times 10^{-12}$  m with 100 keV acceleration) is much smaller than the light source ( $\sim 500$  nm), TEM can obtain the resolution at the interatomic level compared to the greater than  $\sim 1000$  atoms resolution of light.

The configuration of TEM includes four main components: an electron column, a vacuum system, the necessary electronics (the lens the high voltage generator), and the controlling system.<sup>128</sup> Figure 2.24 shows a cross-section schematic of a typical

TEM. A beam of monochromatic electrons is emitted by the electron gun on the top. Similar to SEM, several condenser lenses are applied to control the spot size and the intensity, the high angle electrons are removed by the condenser aperture. The remaining focused electrons can transmit through the specimen which are further focused by the objective lens. The images can be displayed on a fluorescent screen coupled with a film camera or a direct electron detector. The darker areas on a fluorescent screen or TEM images represent a lower amount of electrons can be transmitted through while the lighter areas can transmit and collect more electrons. The application of TEM in this thesis is to observe the size and structure of GO, CNTs and MG particles.

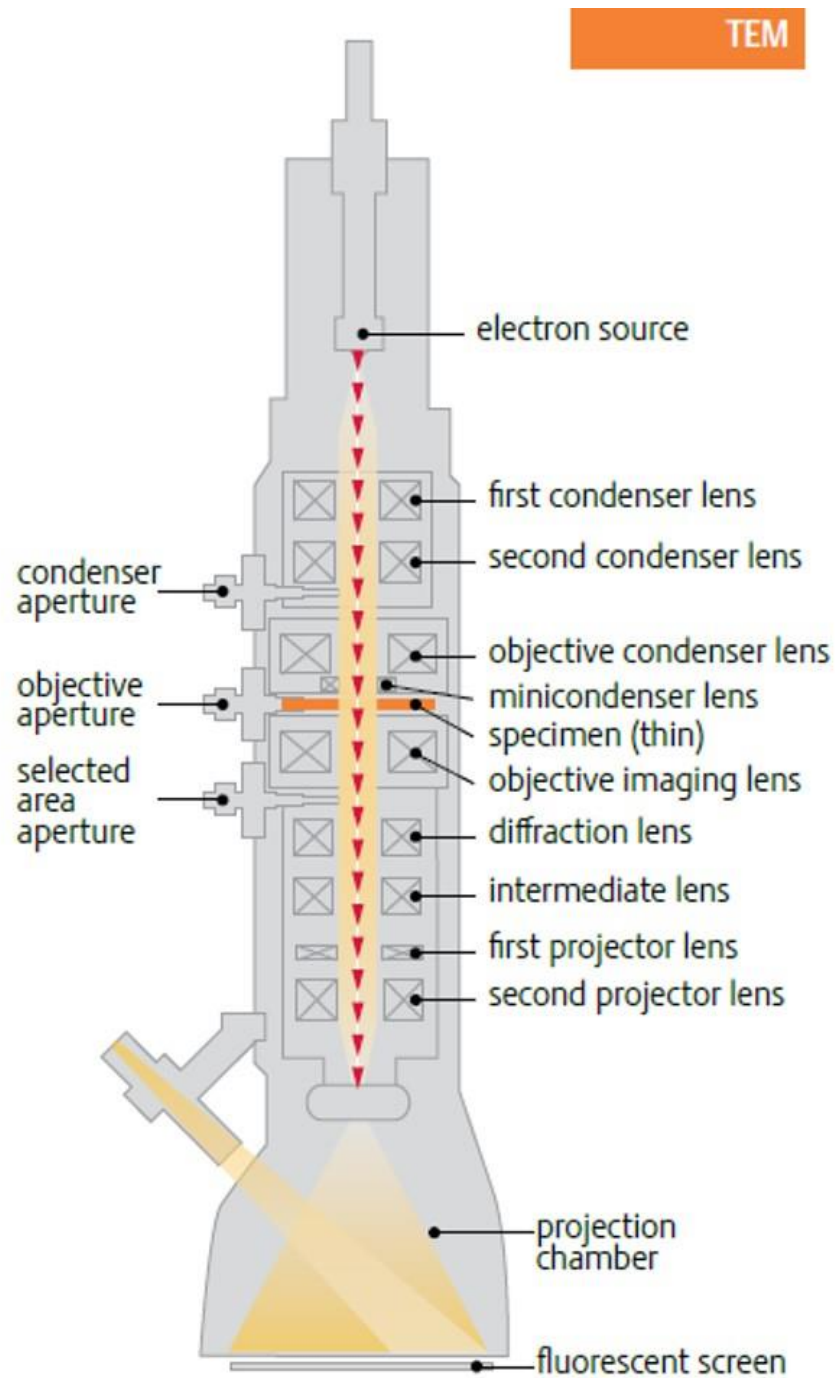


**Fig. 2.24.** Schematic diagram of the TEM.<sup>128</sup>

## 2.4 References

1. Saunders, B. R.; Vincent, B., Microgel particles as model colloids: theory, properties and applications. *Adv. Colloid Interface Sci.* **1999**, 80, 1-25.
2. Baker, W. O., Microgel, A New Macromolecule. *Ind. Eng. Chem.* **1949**, 41, 511-520.
3. Pelton, R.; Hoare, T., Microgels and Their Synthesis: An Introduction. In *Microgel Suspensions*, Wiley-VCH Verlag GmbH & Co. KGaA: 2011; pp 1-32.
4. Vincent, B.; Saunders, B., Interactions and Colloid Stability of Microgel Particles. In *Microgel Suspensions*, Wiley-VCH Verlag GmbH & Co. KGaA: 2011; pp 133-162.
5. Young, R. J.; Lovell, P. A., *Introduction to polymers*. 3rd ed.; CRC Press: Boca Raton, Fla. ; London, 2011; p. 668.
6. Needles, H. L.; Whitfield, R. E., Free-Radical Chemistry of Peptide Bonds. I. Dealkylation of Substituted Amides1. *J. Org. Chem.* **1964**, 29, 3632-3634.
7. Theis, A.; Davis, T. P.; Stenzel, M. H.; Barner-Kowollik, C., Probing the reaction kinetics of vinyl acetate free radical polymerization via living free radical polymerization (MADIX). *Polymer* **2006**, 47, 999-1010.
8. Okay, O.; Funke, W., Steric stabilization of reactive microgels from 1,4-divinylbenzene. *Die Makromolekulare Chemie, Rapid Commun.* **1990**, 11, 583-587.
9. Li, K.; Stöver, H. D. H., Synthesis of monodisperse poly(divinylbenzene) microspheres. *J. Polym. Sci., Part A: Polym. Chem.* **1993**, 31, 3257-3263.
10. Cheng, C. M.; Micale, F. J.; Vanderhoff, J. W.; El-Aasser, M. S., Synthesis and characterization of monodisperse porous polymer particles. *J. Polym. Sci., Part A: Polym. Chem.* **1992**, 30, 235-244.
11. He, J. Y., Crosslinking effect on the deformation and fracture of monodisperse polystyrene-co-divinylbenzene particles. *Express Polym. Lett.* **2013**, 7, 365-374.
12. Jin, J. M.; Lee, J. M.; Ha, M. H.; Lee, K.; Choe, S., Highly crosslinked poly(glycidyl methacrylate-co-divinyl benzene) particles by precipitation polymerization. *Polymer* **2007**, 48, 3107-3115.
13. Landin, D. T.; Macosko, C. W., Cyclization and reduced reactivity of pendant

vinyls during the copolymerization of methyl methacrylate and ethylene glycol dimethacrylate. *Macromolecules* **1988**, 21, 846-851.

14. Maunsky, J.; Klaban, J.; Dušek, K., Vinyl-Divinyl Copolymerization: Copolymerization and Network Formation from Styrene and p- and m-Divinylbenzene. *J. Macromol. Sci.: Part A - Chemistry* **1971**, 5, 1071-1085.

15. Storey, B. T., Copolymerization of styrene and p-divinylbenzene. Initial rates and gel points. *Journal of Polymer Science Part A: General Papers* **1965**, 3, 265-282.

16. Okay, O.; Kurz, M.; Lutz, K.; Funke, W., Cyclization and Reduced Pendant Vinyl Group Reactivity during the Free-Radical Crosslinking Polymerization of 1,4-Divinylbenzene. *Macromolecules* **1995**, 28, 2728-2737.

17. Pelton, R. H.; Chibante, P., Preparation of aqueous latices with N-isopropylacrylamide. *Colloids Surf.* **1986**, 20, 247-256.

18. Dupin, D.; Fujii, S.; Armes, S. P.; Reeve, P.; Baxter, S. M., Efficient Synthesis of Sterically Stabilized pH-Responsive Microgels of Controllable Particle Diameter by Emulsion Polymerization. *Langmuir* **2006**, 22, 3381-3387.

19. Suzuki, D.; Kobayashi, C., Raspberry-Shaped Composite Microgel Synthesis by Seeded Emulsion Polymerization with Hydrogel Particles. *Langmuir* **2014**, 30, 7085-7092.

20. Cunningham, V. J.; Alswieleh, A. M.; Thompson, K. L.; Williams, M.; Leggett, G. J.; Armes, S. P.; Musa, O. M., Poly(glycerol monomethacrylate)-Poly(benzyl methacrylate) Diblock Copolymer Nanoparticles via RAFT Emulsion Polymerization: Synthesis, Characterization, and Interfacial Activity. *Macromolecules* **2014**, 47, 5613-5623.

21. Smith, W. V.; Ewart, R. H., Kinetics of Emulsion Polymerization. *J. Chem. Phys.* **1948**, 16, 592-599.

22. Thickett, S. C.; Gilbert, R. G., Emulsion polymerization: State of the art in kinetics and mechanisms. *Polymer* **2007**, 48, 6965-6991.

23. Cho, I.; Lee, K.-W., Morphology of latex particles formed by poly(methyl methacrylate)-seeded emulsion polymerization of styrene. *J. Appl. Polym. Sci.* **1985**, 30, 1903-1926.

24. Rodriguez, B. E.; Wolfe, M. S.; Fryd, M., Nonuniform Swelling of Alkali Swellable Microgels. *Macromolecules* **1994**, 27, 6642-6647.

25. Morrison, I. D.; Ross, S., *Colloidal Dispersions: Suspensions, Emulsions, and*

*Foams*. Wiley: 2002; p 656.

26. Schramm, L. L., Colloid Stability. In *Emulsions, Foams, and Suspensions*, Wiley-VCH Verlag GmbH & Co. KGaA: 2006; pp 117-154.

27. Shaw, D. J., 8 - Colloid stability. In *Introduction to Colloid and Surface Chemistry (Fourth Edition)*, Butterworth-Heinemann: Oxford, 1992; pp 210-243.

28. Hamaker, H. C., The London—van der Waals attraction between spherical particles. *Physica* **1937**, 4, 1058-1072.

29. Everett, D. H., Chapter 3 Why are Colloidal Dispersions Stable? II Interparticle Forces. In *Basic Principles of Colloid Science*, The Royal Society of Chemistry: 1988; pp 30-53.

30. Long, R. P.; Ross, S., The effects of the overlap of double layers on electrophoretic mobilities of polydisperse suspensions. *J. Colloid Interface Sci.* **1968**, 26, 434-445.

31. Bohinc, K.; Kralj-Iglič, V.; Iglič, A., Thickness of electrical double layer. Effect of ion size. *Electrochim. Acta* **2001**, 46, 3033-3040.

32. Wang, H.; Pilon, L., Accurate Simulations of Electric Double Layer Capacitance of Ultramicroelectrodes. *J. Phys. Chem. C* **2011**, 115, 16711-16719.

33. Stojek, Z., The Electrical Double Layer and Its Structure. In *Electroanalytical Methods: Guide to Experiments and Applications*, Scholz, F.; Bond, A. M.; Compton, R. G.; Fiedler, D. A.; Inzelt, G.; Kahlert, H.; Komorsky-Lovrić, Š.; Lohse, H.; Lovrić, M.; Marken, F.; Neudeck, A.; Retter, U.; Scholz, F.; Stojek, Z., Eds. Springer Berlin Heidelberg: Berlin, Heidelberg, 2010; pp 3-9.

34. Shaw, D. J., 7 - Charged interfaces. In *Introduction to Colloid and Surface Chemistry (Fourth Edition)*, Butterworth-Heinemann: Oxford, 1992; pp 174-209.

35. Moreno, R.; Ferrari, B., Nanoparticles Dispersion and the Effect of Related Parameters in the EPD Kinetics. In *Electrophoretic Deposition of Nanomaterials*, Dickerson, H. J.; Boccaccini, R. A., Eds. Springer New York: New York, NY, 2012; pp 73-128.

36. Derjaguin, B., A theory of interaction of particles in presence of electric double layers and the stability of lyophobic colloids and disperse systems. *Prog. Surf. Sci.* **1993**, 43, 1-14.

37. Derjaguin, B.; Landau, L., Theory of the stability of strongly charged lyophobic sols and of the adhesion of strongly charged particles in solutions of

electrolytes. *Prog. Surf. Sci.* **1993**, 43, 30-59.

38. Verwey, E. J. W., Theory of the Stability of Lyophobic Colloids. *J Phys Colloid Chem.* **1947**, 51, 631-636.

39. Besra, L.; Liu, M., A review on fundamentals and applications of electrophoretic deposition (EPD). *Prog. Mater Sci.* **2007**, 52, 1-61.

40. Islam, A. M.; Chowdhry, B. Z.; Snowden, M. J., Heteroaggregation in colloidal dispersions. *Adv. Colloid Interface Sci.* **1995**, 62, 109-136.

41. Napper, D. H.; Netschey, A., Studies of the steric stabilization of colloidal particles. *J. Colloid Interface Sci.* **1971**, 37, 528-535.

42. Napper, D. H., Steric stabilization. *J. Colloid Interface Sci.* **1977**, 58, 390-407.

43. Bonham, J. A.; Faers, M. A.; van Duijneveldt, J. S., Non-aqueous microgel particles: synthesis, properties and applications. *Soft Matter* **2014**, 10, 9384-9398.

44. Thorne, J. B.; Vine, G. J.; Snowden, M. J., Microgel applications and commercial considerations. *Colloid. Polym. Sci.* **2011**, 289, 625-646.

45. Farooqi Zahoor, H.; Khan Shanza, R.; Begum, R.; Ijaz, A., Review on synthesis, properties, characterization, and applications of responsive microgels fabricated with gold nanostructures. In *Reviews in Chemical Engineering*, 2016; Vol. 32, p 49.

46. Yue, M.; Hoshino, Y.; Miura, Y., Design rationale of thermally responsive microgel particle films that reversibly absorb large amounts of CO<sub>2</sub>: fine tuning the pK<sub>a</sub> of ammonium ions in the particles. *Chem. Sci.* **2015**, 6, 6112-6123.

47. Nguyen, B. T.; Wang, W.; Saunders, B. R.; Benyahia, L.; Nicolai, T., pH-Responsive Water-in-Water Pickering Emulsions. *Langmuir* **2015**, 31, 3605-3611.

48. Shi, S.; Wang, Q.; Wang, T.; Ren, S.; Gao, Y.; Wang, N., Thermo-, pH-, and Light-Responsive Poly(N-isopropylacrylamide-co-methacrylic acid)-Au Hybrid Microgels Prepared by the in Situ Reduction Method Based on Au-Thiol Chemistry. *J. Phys. Chem. B* **2014**, 118, 7177-7186.

49. Zelzer, M.; Todd, S. J.; Hirst, A. R.; McDonald, T. O.; Ulijn, R. V., Enzyme responsive materials: design strategies and future developments. *Biomater. Sci.* **2013**, 1, 11-39.

50. Klinger, D.; Landfester, K., Stimuli-responsive microgels for the loading and release of functional compounds: Fundamental concepts and applications. *Polymer*

**2012**, 53, 5209-5231.

51. Fisher, O. Z.; Engineering, T. U. o. T. a. A. B., *Novel PH-Responsive Microgels and Nanogels as Intelligent Polymer Therapeutics*. University of Texas at Austin: 2008.
52. Saunders, J. M.; Tong, T.; Le Maitre, C. L.; Freemont, T. J.; Saunders, B. R., A study of pH-responsive microgel dispersions: from fluid-to-gel transitions to mechanical property restoration for load-bearing tissue. *Soft Matter* **2007**, 3, 486-494.
53. Saunders, B. R.; Laajam, N.; Daly, E.; Teow, S.; Hu, X.; Stepto, R., Microgels: From responsive polymer colloids to biomaterials. *Adv. Colloid Interface Sci.* **2009**, 147–148, 251-262.
54. Reyes-Ortega, F., 3 - pH-responsive polymers: properties, synthesis and applications. In *Smart Polymers and their Applications*, Woodhead Publishing: 2014; pp 45-92.
55. Thaiboonrod, S.; Berkland, C.; Milani, A. H.; Ulijn, R.; Saunders, B. R., Poly(vinylamine) microgels: pH-responsive particles with high primary amine contents. *Soft Matter* **2013**, 9, 3920-3930.
56. Hunt, J. A.; Chen, R.; van Veen, T.; Bryan, N., Hydrogels for tissue engineering and regenerative medicine. *J. Mater. Chem. B* **2014**, 2, 5319-5338.
57. Li, Z.; Fan, Z.; Xu, Y.; Lo, W.; Wang, X.; Niu, H.; Li, X.; Xie, X.; Khan, M.; Guan, J., pH-Sensitive and Thermosensitive Hydrogels as Stem-Cell Carriers for Cardiac Therapy. *ACS Applied Materials & Interfaces* **2016**, 8, 10752-10760.
58. Freemont, T. J.; Saunders, B. R., pH-Responsive microgel dispersions for repairing damaged load-bearing soft tissue. *Soft Matter* **2008**, 4, 919-924.
59. Xu, W.; He, X.; Zhong, M.; Hu, X.; Xiao, Y., A novel pH-responsive hydrogel based on natural polysaccharides for controlled release of protein drugs. *RSC Adv.* **2015**, 5, 3157-3167.
60. Abbaszad Rafi, A.; Mahkam, M.; Davaran, S.; Hamishehkar, H., A Smart pH-responsive Nano-Carrier as a Drug Delivery System: A hybrid system comprised of mesoporous nanosilica MCM-41 (as a nano-container) & a pH-sensitive polymer (as smart reversible gatekeepers): Preparation, characterization and in vitro release studies of an anti-cancer drug. *Eur. J. Pharm. Sci.* **2016**, 93, 64-73.
61. Kost, J.; Langer, R., Responsive polymeric delivery systems. *Adv. Drug Del. Rev.* **2012**, 64, Supplement, 327-341.



62. Liu, R.; Milani, A. H.; Freemont, T. J.; Saunders, B. R., Doubly crosslinked pH-responsive microgels prepared by particle inter-penetration: swelling and mechanical properties. *Soft Matter* **2011**, 7, 4696-4704.
63. Lally, S.; Liu, R.; Supasuteekul, C.; Saunders, B. R.; Freemont, T., Using osmotic deswelling of microgel particles to control the mechanical properties of pH-responsive hydrogel composites. *J. Mater. Chem.* **2011**, 21, 17719-17728.
64. Cui, Z.; Wang, W.; Obeng, M.; Chen, M.; Wu, S.; Kinloch, I.; Saunders, B. R., Using intra-microgel crosslinking to control the mechanical properties of doubly crosslinked microgels. *Soft Matter* **2016**, 12, 6985-6994.
65. Flory, P. J., *Principles of Polymer Chemistry*. Cornell University Press: 1953; p 672.
66. Arndt, K.-F.; Krah, F.; Richter, S.; Steiner, G., Swelling-Related Processes in Hydrogels. In *Hydrogel Sensors and Actuators: Engineering and Technology*, Gerlach, G.; Arndt, K.-F., Eds. Springer Berlin Heidelberg: Berlin, Heidelberg, 2010; pp 69-136.
67. Hirotsu, S., Static and time-dependent properties of polymer gels around the volume phase transition. *Phase Transit.* **1994**, 47, 183-240.
68. Vasheghani-Farahani, E.; Vera, J. H.; Cooper, D. G.; Weber, M. E., Swelling of ionic gels in electrolyte solutions. *Ind. Eng. Chem. Res.* **1990**, 29, 554-560.
69. Lally, S.; Mackenzie, P.; LeMaitre, C. L.; Freemont, T. J.; Saunders, B. R., Microgel particles containing methacrylic acid: pH-triggered swelling behaviour and potential for biomaterial application. *J. Colloid Interface Sci.* **2007**, 316, 367-375.
70. Loxley, A.; Vincent, B., Equilibrium and kinetic aspects of the pH-dependent swelling of poly(2-vinylpyridine-co-styrene) microgels. *Colloid. Polym. Sci.* **1997**, 275, 1108-1114.
71. Daly, E.; Saunders, B. R., A Study of the Effect of Electrolyte on the Swelling and Stability of Poly(N-isopropylacrylamide) Microgel Dispersions. *Langmuir* **2000**, 16, 5546-5552.
72. Tan, B. H.; Tam, K. C.; Lam, Y. C.; Tan, C. B., Microstructure and Rheology of Stimuli-Responsive Nanocolloidal Systems Effect of Ionic Strength. *Langmuir* **2004**, 20, 11380-11386.
73. Mohanty, P. S.; Nojd, S.; Bergman, M. J.; Nagele, G.; Arrese-Igor, S.; Alegria, A.; Roa, R.; Schurtenberger, P.; Dhont, J. K. G., Dielectric spectroscopy of ionic microgel suspensions. *Soft Matter* **2016**.

74. Ngai, T.; Auweter, H.; Behrens, S. H., Environmental Responsiveness of Microgel Particles and Particle-Stabilized Emulsions. *Macromolecules* **2006**, 39, 8171-8177.
75. Peppas, N.; Langer, R., New challenges in biomaterials. *Science* **1994**, 263, 1715-1720.
76. Saunders, B. R., Doubly Crosslinked Microgels. In *Hydrogel Micro and Nanoparticles*, Wiley-VCH Verlag GmbH & Co. KGaA: 2012; pp 141-167.
77. Hoare, T., Macroscopic Microgel Networks. In *Hydrogel Micro and Nanoparticles*, Wiley-VCH Verlag GmbH & Co. KGaA: 2012; pp 281-315.
78. Hu, Z.; Lu, X.; Gao, J.; Wang, C., Polymer Gel Nanoparticle Networks. *Adv. Mater.* **2000**, 12, 1173-1176.
79. Sivakumaran, D.; Maitland, D.; Hoare, T., Injectable Microgel-Hydrogel Composites for Prolonged Small-Molecule Drug Delivery. *Biomacromolecules* **2011**, 12, 4112-4120.
80. Haque, M. A.; Kurokawa, T.; Gong, J. P., Super tough double network hydrogels and their application as biomaterials. *Polymer* **2012**, 53, 1805-1822.
81. Meenach, S. A.; Anderson, K. W.; Hilt, J. Z., Hydrogel Nanocomposites: Biomedical Applications, Biocompatibility, and Toxicity Analysis. In *Safety of Nanoparticles: From Manufacturing to Medical Applications*, Webster, J. T., Ed. Springer New York, New York, 2009; pp 131-157.
82. Haraguchi, K.; Takehisa, T., Nanocomposite Hydrogels: A Unique Organic–Inorganic Network Structure with Extraordinary Mechanical, Optical, and Swelling/De-swelling Properties. *Adv. Mater.* **2002**, 14, 1120.
83. Takigawa, T.; Araki, H.; Takahashi, K.; Masuda, T., Effects of mechanical stress on the volume phase transition of poly(N-isopropylacrylamide) based polymer gels. *J. Chem. Phys.* **2000**, 113, 7640-7645.
84. Xiang, Y.; Peng, Z.; Chen, D., A new polymer/clay nano-composite hydrogel with improved response rate and tensile mechanical properties. *Eur. Polym. J.* **2006**, 42, 2125-2132.
85. Schexnailder, P.; Schmidt, G., Nanocomposite polymer hydrogels. *Colloid. Polym. Sci.* **2009**, 287, 1-11.
86. Campbell, S. B.; Hoare, T., Externally addressable hydrogel nanocomposites for biomedical applications. *Curr. Opin. Chem. Eng.* **2014**, 4, 1-10.

87. Li, H.; Yang, J.; Hu, X.; Liang, J.; Fan, Y.; Zhang, X., Superabsorbent polysaccharide hydrogels based on pullulan derivate as antibacterial release wound dressing. *J. Biomed. Mater. Res. A* **2011**, 98A, 31-39.
88. Zhu, C.-H.; Hai, Z.-B.; Cui, C.-H.; Li, H.-H.; Chen, J.-F.; Yu, S.-H., In Situ Controlled Synthesis of Thermosensitive Poly(N-isopropylacrylamide)/Au Nanocomposite Hydrogels by Gamma Radiation for Catalytic Application. *Small* **2012**, 8, 930-936.
89. Dimiev, A. M.; Eigler, S., *Graphene Oxide: Fundamentals and Applications*. Wiley: 2016; p 464.
90. Krishnan, D.; Kim, F.; Luo, J.; Cruz-Silva, R.; Cote, L. J.; Jang, H. D.; Huang, J., Energetic graphene oxide: Challenges and opportunities. *Nano Today* **2012**, 7, 137-152.
91. Novoselov, K. S.; Geim, A. K.; Morozov, S. V.; Jiang, D.; Zhang, Y.; Dubonos, S. V.; Grigorieva, I. V.; Firsov, A. A., Electric Field Effect in Atomically Thin Carbon Films. *Science* **2004**, 306, 666-669.
92. Geim, A. K.; Novoselov, K. S., The rise of graphene. *Nat. Mater.* **2007**, 6, 183-191.
93. Dreyer, D. R.; Park, S.; Bielawski, C. W.; Ruoff, R. S., The chemistry of graphene oxide. *Chem. Soc. Rev.* **2010**, 39, 228-240.
94. Lerf, A.; He, H.; Forster, M.; Klinowski, J., Structure of Graphite Oxide Revisited. *J. Phys. Chem. B* **1998**, 102, 4477-4482.
95. Liu, R.; Liang, S.; Tang, X.-Z.; Yan, D.; Li, X.; Yu, Z.-Z., Tough and highly stretchable graphene oxide/polyacrylamide nanocomposite hydrogels. *J. Mater. Chem.* **2012**, 22, 14160-14167.
96. Medhekar, N. V.; Ramasubramaniam, A.; Ruoff, R. S.; Shenoy, V. B., Hydrogen Bond Networks in Graphene Oxide Composite Paper: Structure and Mechanical Properties. *ACS Nano* **2010**, 4, 2300-2306.
97. Yu, Y.; De Andrade, L. C. X.; Fang, L.; Ma, J.; Zhang, W.; Tang, Y., Graphene oxide and hyperbranched polymer-toughened hydrogels with improved absorption properties and durability. *J. Mater. Sci.* **2015**, 50, 3457-3466.
98. Faghihi, S.; Gheysour, M.; Karimi, A.; Salarian, R., Fabrication and mechanical characterization of graphene oxide-reinforced poly (acrylic acid)/gelatin composite hydrogels. *J. Appl. Phys.* **2014**, 115, 083513.

99. Lu, N.; Liu, J.; Li, J.; Zhang, Z.; Weng, Y.; Yuan, B.; Yang, K.; Ma, Y., Tunable dual-stimuli response of a microgel composite consisting of reduced graphene oxide nanoparticles and poly(N-isopropylacrylamide) hydrogel microspheres. *J. Mater. Chem. B* **2014**, 2, 3791-3798.
100. Huang, Y.; Zhang, M.; Ruan, W., High-water-content graphene oxide/polyvinyl alcohol hydrogel with excellent mechanical properties. *J. Mater. Chem. A* **2014**, 2, 10508-10515.
101. Wang, Y.; Li, Z.; Wang, J.; Li, J.; Lin, Y., Graphene and graphene oxide: biofunctionalization and applications in biotechnology. *Trends Biotechnol.* **2011**, 29, 205-212.
102. Gao, L.; Lian, C.; Zhou, Y.; Yan, L.; Li, Q.; Zhang, C.; Chen, L.; Chen, K., Graphene oxide–DNA based sensors. *Biosens. Bioelectron.* **2014**, 60, 22-29.
103. Monthieux, M.; Serp, P.; Flahaut, E.; Razafinimanana, M.; Laurent, C.; Peigney, A.; Bacsa, W.; Broto, J.-M., Introduction to Carbon Nanotubes. In *Springer Handbook of Nanotechnology*, Bhushan, B., Ed. Springer Berlin Heidelberg: Berlin, Heidelberg, 2007; pp 43-112.
104. Iijima, S., Helical microtubules of graphitic carbon. *Nature* **1991**, 354, 56-58.
105. De Volder, M. F. L.; Tawfick, S. H.; Baughman, R. H.; Hart, A. J., Carbon Nanotubes: Present and Future Commercial Applications. *Science* **2013**, 339, 535-539.
106. Zhang, R.; Zhang, Y.; Zhang, Q.; Xie, H.; Qian, W.; Wei, F., Growth of Half-Meter Long Carbon Nanotubes Based on Schulz–Flory Distribution. *ACS Nano* **2013**, 7, 6156-6161.
107. Choudhary, V.; Gupta, A., *Polymer/Carbon Nanotube Nanocomposites*. InTech: 2011.
108. Peng, B.; Locascio, M.; Zapol, P.; Li, S.; Mielke, S. L.; Schatz, G. C.; Espinosa, H. D., Measurements of near-ultimate strength for multiwalled carbon nanotubes and irradiation-induced crosslinking improvements. *Nat. Nano.* **2008**, 3, 626-631.
109. Adewunmi, A. A.; Ismail, S.; Sultan, A. S., Carbon Nanotubes (CNTs) Nanocomposite Hydrogels Developed for Various Applications: A Critical Review. *J. Inorg. Organomet. Polym. Mater.* **2016**, 26, 717-737.
110. Zhang, C.-H.; Luo, Y.-L.; Chen, Y.-S.; Wei, Q.-B.; Fan, L.-H., Preparation and Theophylline Delivery Applications of Novel PMAA/MWCNT-COOH Nanohybrid Hydrogels. *J. Biomater. Sci. Polym. Ed.* **2009**, 20, 1119-1135.

111. Sudha; Mishra, B. M.; Kumar, D., Effect of Multiwalled Carbon Nanotubes on the Conductivity and Swelling Properties of Porous Polyacrylamide Hydrogels. *Particul. Sci. Technol.* **2014**, 32, 624-631.
112. Serrano, M. C.; Gutiérrez, M. C.; del Monte, F., Role of polymers in the design of 3D carbon nanotube-based scaffolds for biomedical applications. *Prog. Polym. Sci.* **2014**, 39, 1448-1471.
113. Spizzirri, U. G.; Hampel, S.; Cirillo, G.; Nicoletta, F. P.; Hassan, A.; Vittorio, O.; Picci, N.; Iemma, F., Spherical gelatin/CNTs hybrid microgels as electro-responsive drug delivery systems. *Int. J. Pharm.* **2013**, 448, 115-122.
114. Li, H.; Wang, D. Q.; Chen, H. L.; Liu, B. L.; Gao, L. Z., A Novel Gelatin–Carbon Nanotubes Hybrid Hydrogel. *Macromol. Biosci.* **2003**, 3, 720-724.
115. Park, J.; Lee, Y.; Hong, J.; Lee, Y.; Ha, M.; Jung, Y.; Lim, H.; Kim, S. Y.; Ko, H., Tactile-Direction-Sensitive and Stretchable Electronic Skins Based on Human-Skin-Inspired Interlocked Microstructures. *ACS Nano* **2014**, 8, 12020-12029.
116. Chung, Y. W., *Introduction to Materials Science and Engineering*. CRC Press: 2006; p 304.
117. Normand, V.; Pudney, P. D. A.; Aymard, P.; Norton, I. T., Weighted-average isostrain and isostress model to describe the kinetic evolution of the mechanical properties of a composite gel: Application to the system gelatin:Maltodextrin. *J. Appl. Polym. Sci.* **2000**, 77, 1465-1477.
118. Alexander, M.; Dalgleish, D. G., Dynamic Light Scattering Techniques and Their Applications in Food Science. *Food Biophys.* **2006**, 1, 2-13.
119. Merkus, H. G., *Particle Size Measurements: Fundamentals, Practice, Quality*. Springer Netherlands: 2009; p 534.
120. Kneipp, K.; Kneipp, H.; Itzkan, I.; Dasari, R. R.; Feld, M. S., Ultrasensitive Chemical Analysis by Raman Spectroscopy. *Chem. Rev.* **1999**, 99, 2957-2976.
121. Smith, E.; Dent, G., *Modern Raman Spectroscopy: A Practical Approach*. Wiley: 2005; p 224.
122. Ferraro, J. R.; Nakamoto, K.; Brown, C. W., Chapter 2 - Instrumentation and Experimental Techniques. In *Introductory Raman Spectroscopy (Second Edition)*, Academic Press: San Diego, 2003; pp 95-146.
123. Chen, D. T. N.; Wen, Q.; Janmey, P. A.; Crocker, J. C.; Yodh, A. G., Rheology of Soft Materials. *Annu. Rev. Condens. Matter Phys.* **2010**, 1, 301-322.

124. Motyka, A. L., An introduction to rheology with an emphasis on application to dispersions. *J. Chem. Educ.* **1996**, 73, 374-380.
125. Schramm, G., *A practical approach to rheology and rheometry*. 2nd Edition ed.; Haake Karlsruhe: 1994; p 290.
126. Zhou, W.; Apkarian, R.; Wang, Z. L.; Joy, D., Fundamentals of Scanning Electron Microscopy (SEM). In *Scanning Microscopy for Nanotechnology: Techniques and Applications*, Springer New York: New York, NY, 2007; pp 1-40.
127. Vernon-Parry, K. D., Scanning electron microscopy: an introduction. *III-Vs Review* **2000**, 13, 40-44.
128. FEI, *An Introduction to electron microscopy*. 2010.
129. Gaillard, C.; Stadelmann, P. A.; Plummer, C. J. G.; Fuchs, G., Practical method for high-resolution imaging of polymers by low-voltage scanning electron microscopy. *Scanning* **2004**, 26, 122-130.
130. Williams, D. B.; Carter, C. B., *Transmission Electron Microscopy: A Textbook for Materials Science*. Springer US: 2009.

## Chapter 3: Microgel/Graphene oxide composites

### 3.1 Abstract

Earlier studies in our group have shown that concentrated dispersions of pH-responsive microgel (MG) particles can form macroscopic gels.<sup>1</sup> However, the mechanical properties of such gels were limited by the chain elasticity of polymers. In this chapter, we mixed low concentrations of graphene oxide (GO) with MG particles and formed composite DX MG/GO gels. The MG / GO mixture formed physical gels of SX MG/GO and were further proceed to be DX MG/GO gels by a free-radical reaction from pendant vinyl groups. The influence of the GO concentration on the mechanical properties of the SX MG/GO and DX MG/GO gels was investigated using dynamic rheology and static axial compression measurements. An isostrain model was used to describe the modulus of composites. The data support that the inclusion of GO can increase the modulus and tune the mechanical properties by adjusting the concentration of GO. The composite DX gels with only 1 wt.% of GO introduced significantly improved the stiffness compared to the GO free gels. Moreover, a Live / dead assay on the composite suggested that the composites were biocompatible. This new composite hydrogel was designed as a potential material for soft tissue engineering applications.

## 3.2 Introduction

The properties of hydrogels are attracting large interest and their structural complexity is increasing.<sup>2</sup> Remarkable improvements in gel modulus<sup>3</sup>, ductility<sup>4</sup>, swelling ratios<sup>5</sup> and toughness<sup>6</sup> have been achieved. The MGs and DX MGs were introduced in Chapter 2. In this study, we investigate DX MGs prepared in the presence of low concentrations of GO which are expected to provide a potential mechanical property enhancement, which was the aim of this research.

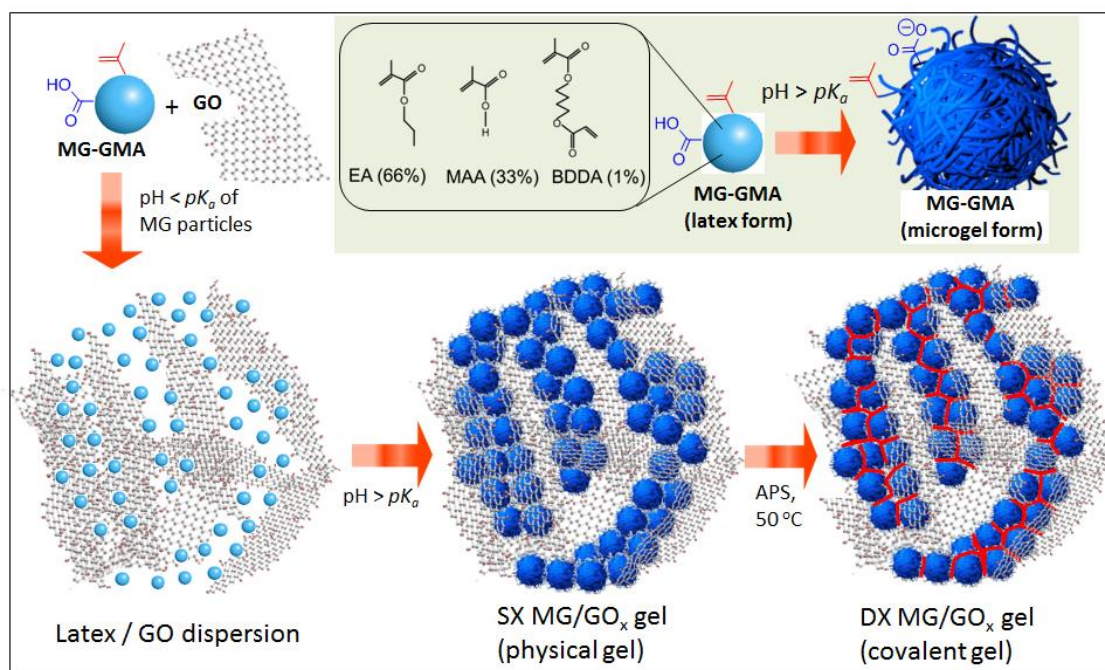
The MGs studied here were prepared by a seed-feed emulsion polymerisation. The as-made poly(ethyl acrylate-*co*-methacrylic acid-*co*-1,4-butanediol diacrylate) MG particles (poly(EA/MAA/BDDA)) were functionalised by glycidyl methacrylate (GMA) to introduce the pendant vinyl groups. These non-functionalised and functionalised MG particles are abbreviated as NF MG and SX MG particles. These MG particles can swell with increasing pH, and the phenomenon of this swelling process can be described as a transformation from a white latex liquid to a transparent physical gel.<sup>7</sup> After gel formation, the DX process can be achieved via a free-radical coupling of vinyl groups among the particle-particle contact area<sup>1</sup>. This liquid to gel process has been proved to be suitable for injectable medicine which can be applied to the restoration of degenerated intervertebral discs (IVDs)<sup>8</sup>.

Graphene has outstanding mechanical, electrical and thermal properties<sup>9-13</sup>. GO as a well-known member of the graphene family, is rich with hydrophilic groups distributed in the entire sheets<sup>14</sup>. The oxidised groups contribute solubility and most of them can form hydrogen bonds or be chemical reactive<sup>11</sup>. Therefore, GO is water-dispersable which is suitable for blending with hydrogels.<sup>9</sup> Furthermore, GO has received a lot of attention because of its high aspect ratio and high modulus<sup>15</sup> which



are also frequently applied in studies of novel gels.<sup>16-18</sup> The biological applicability of GO is also well known,<sup>19-21</sup> which showed promising potential for soft tissue engineering<sup>22</sup>.

The composite gel preparation is shown in Scheme 1. The chemical structures of monomers are shown on the top. The DX process was started with a mixed dispersion of SX MG in latex form and GO dispersion. The physical gel was formed by pH-triggered swelling of the MG particles and it is termed as SX MG/GO<sub>x</sub>, where *x* is the weight concentration of GO. Subsequently, the covalently interlinked gels were achieved by heating in the presence of an initiator (APS), and this is termed as DX MG/GO<sub>x</sub>. In this chapter the morphology, swelling and mechanical properties of SX MG/GO and DX MG/GO composite gels are studied. The main aim of this chapter is to investigate how added GO enhances the mechanical properties of the DX gels, and assess if it has the potential for application in soft tissue engineering.



**Scheme 3.1.** The depiction of the preparation of DX MG/GO gels. The structures of monomers and particles were shown the in the top. The pH-triggered swelling and the DX process of MG/GO composite gel is shown in the bottom.

### **3.3 Experimental**

#### **3.3.1 Materials**

Graphite (Graphexel grade 2369), EA, MAA, BDDA, GMA, H<sub>2</sub>SO<sub>4</sub>, NaNO<sub>3</sub>, NaOH, KMnO<sub>4</sub>, H<sub>2</sub>O<sub>2</sub>, APS, phosphate buffered saline (PBS, pH = 7.4 bioreagent) were all purchased from Sigma-Aldrich. All reagents were the highest purity available and were used as received. Biological reagents were prepared using Dulbecco's modified Eagle's medium (DMEM, Gibco), fetal bovine serum (FBS, Gibco) and antibiotic/antimycotic (Sigma-Aldrich). All water was of ultrahigh purity and was distilled and deionised.

#### **3.3.2 Synthesis of graphene oxide**

Preparation of GO was achieved using "modified Hummers method".<sup>23</sup> Graphite powder (5 g) and concentrated H<sub>2</sub>SO<sub>4</sub> (170 ml) were introduced into a 5 L flask with stirring and an ice bath was placed on the bottom. NaNO<sub>3</sub> (3.75 g, 0.04 mol.) was added and stirring continued for 5 h. KMnO<sub>4</sub> (25 g, 0.16 mol.) was carefully added to prevent the temperature of the mixture exceeding 20 °C. After all of the additives were dissolved, the ice bath was removed and the mixture was heated at 35 °C with stirring for 2 h. The dispersion was further stirred at room temperature for seven days. After the reaction, a washing method was applied to obtain exfoliated the GO dispersion. The product was slowly dispersed into H<sub>2</sub>SO<sub>4</sub> solution (5 wt.%, 550 ml) and stirred for 3 h. Then, aqueous H<sub>2</sub>O<sub>2</sub> (15 g, 30 vol.%) was slowly added over a period of 5 min. The mixture became a gold coloured dispersion and stirring was continued for a further 2 h. The suspension was diluted with 500 ml of 3 wt% H<sub>2</sub>SO<sub>4</sub> containing 0.5 wt% H<sub>2</sub>O<sub>2</sub> solution and left overnight. The product was centrifuged at 9000 rpm for 20 min, and the clear supernatant liquid was removed. The remaining

viscous liquid was washed with a further 3 wt.%  $\text{H}_2\text{SO}_4$  / 0.5 wt.%  $\text{H}_2\text{O}_2$  solution (500 ml). The washing process was repeated nine times, and then the mixture was further purified by dialysis for 7 days. The final pH of the purified, exfoliated, GO dispersion was 7.2.

### **3.3.3 Synthesis of poly(EA/MAA/BDDA) microgel**

The synthesis of the MG was conducted using seed-feed emulsion polymerisation method according to a previously published method<sup>24</sup> and is briefly described here. The MG particles contained about 33 wt.% of MAA on total monomer mass. A co-monomer solution (250 g) containing EA (167 g, 1.88 mol), MAA (83 g, 0.83 mol), BDDA (2.5 g, 0.01 mol) was prepared. A total of 31.5 g of the co-monomer solution was used for the seed formation. The solution was added to water (518 g) containing SDS (1.8 g, 6.0 mmol) and then  $\text{K}_2\text{HPO}_4$  (3.15 g of a 7 wt.% solution) and APS (10 g of a 2 wt.% solution) were added. The seed was prepared at 80 °C with mechanical stirring under nitrogen for 30 min. Then the remaining monomers were added at a uniform rate over a period of 1.5 h. The reaction was continued for a further 2 h. The product was purified by extensive dialysis using water.

### **3.3.4 Synthesis of GMA-functionalised poly(EA/MAA/BDDA) microgel**

MG dispersion (100 g of 10 wt.% dispersion) was mixed with GMA (16.6 g, 0.12 mol). The pH of the mixture was adjusted to about 5.4 using NaOH solution (0.05 M). The mixture was heated at 50 °C for 8 h. After the reaction, chloroform was used to wash the product twice and then removed using rotary evaporation. The MG-GMA dispersion was further purified by extensive dialysis.

### **3.3.5 Preparation of SX MG/GO physical gels and DX MG/GO covalent gels**

To prepare the composite gels a thoroughly mixed dispersion containing MG-GMA and GO was first prepared at a pH of about 4.7. As an example, the DX MG/GO<sub>1.0</sub> composite was prepared by thoroughly mixing MG-GMA (6.67 g of 15 wt.% dispersion) and GO (22.22 g of 0.45 wt.% dispersion). (For the other DX MG/GO<sub>x</sub> systems the masses of GO were reduced accordingly.) The mixed dispersion was concentrated to ~ 10 g using rotary evaporation at room temperature. An aqueous solution (0.2 g) of APS and NaOH was then added with stirring. The added solution contained 3.4 wt % of APS, and the concentration of NaOH was 4 M. The gel had a final pH of ~7.2. This process triggered the formation of an SX MG/GO physical gel. To form the DX MG/GO gel, the SX MG/GO mixture was heated at 50 °C for 8 h. All the gels studied in this work contained a MG particle concentration of 10 wt.%, and the pH values were adjusted to ~ 7.2. The SX MG/GO physical gels were studied in the absence of added APS.

### **3.3.6 Physical measurements**

Titration measurements were performed using a Mettler Toledo DL 15 titrator in the presence of aqueous 0.1 M NaCl. TGA measurements were performed using a TA Instrument Q500 with a heating rate of 10 °C / min. Photon correlation spectroscopy (PCS) measurements were performed using a BI-9000 Brookhaven light scattering apparatus (Brookhaven Instrument Cooperation) equipped with a 20 mW HeNe Laser and the detector was set at a scattering angle of 90°. TEM data were obtained using a JEOL JEM-2011F operating at an accelerating voltage of 200 kV. Zeta potential data were obtained using a Malvern Nano ZS using a GO concentration of 0.01 wt.% and a background electrolyte concentration (NaNO<sub>3</sub>) of 0.01 M. The rheological properties of the gels were measured using a TA Instruments AR-G2

temperature-controlled rheometer equipped with an environmental chamber. The measurement geometry used a 20 mm flat disc. Frequency-sweep and strain-sweep data were measured at 25 °C. For the frequency-sweep data a strain of 1% was used. The strain sweep data were measured using a frequency of 1 Hz. The compression tests were conducted using an Instron Series 5569 load frame equipped with a 100 N compression testing head. The compression rate was 2 mm/min, and the average size of the gel cylinders was 10.8 mm in height and 9.6 mm in diameter, respectively. MG and GO particle size and the morphology of GO, MG and composites were probed by SEM using a Philips xl30 instrument. Before observation, the gel samples were rapidly freeze-dried using liquid nitrogen. The SEM samples were coated by platinum before the examination.

### **3.3.7 Assessment of cytotoxicity**

The operational details and results of cytotoxicity measurements are provided by Daman Adlam (Manchester University). Human nucleus pulposus (NP) cells were cultured in Dulbecco's modified Eagle's medium supplemented with 10% fetal bovine serum and antibiotic / antimycotic at 37 °C in a humidified 5% CO<sub>2</sub> atmosphere. Cells were harvested by trypsinisation and seeded at a density of  $2 \times 10^4$  cells/well into 24-well culture plates containing 13 mm diameter sterile glass coverslips. After 24 h in culture, sterile toroid-shaped composites (inset of Fig. 3.17(a)) were introduced into wells and cultured for a further 10 days. After this time the coverslips were removed and cell viability assessed by live / dead assay (Invitrogen, UK) on the NP cells exposed to gels versus controls. Images were taken with an Olympus BX51 fluorescence microscope and a Leitz Diavert inverted light microscope.

## 3.4 Results and discussion

### 3.4.1 Microgel characterisation

In this study, the non-functionalised MG, functional MG and doubly crosslinked MG were abbreviated as NF MG, SX MG and DX MG. The chemistry of functionalisation for introducing vinyl groups to MG is described in Fig 3.1. The GMA is believed to have reacted with the carboxylic groups in the MG particles via a ring-opening reaction. There are two reaction mechanism routes to modify the MG particles with GMA. As shown in Fig. 3.1, the GMA can attack either a 3° carbon atom (position **1**) or a 2° carbon atom (position **2**). For an epoxide ring, the carbocation is more stable in 3° carbon than 2° carbon and therefore the main product is the reaction in position **1**. This proposal follows from the work of Reis et al.,<sup>25</sup> which showed that ~87.5% of -COOH groups in polymers were attached to position **1** at pH 3.5 for related species.

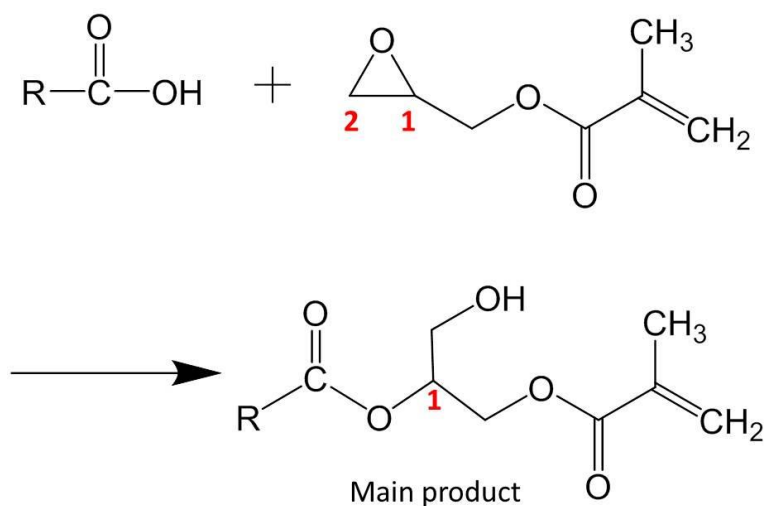


**Fig. 3.1.** The main mechanism of GMA functionalisation reaction.

#### 3.4.1.1 Potentiometric titration

The potentiometric titration was performed to calculate the functional degree of SX MG. As shown in Fig. 3.2, the difference in MAA content between NF MG and SX

MG was caused from the GMA functionalisation. Therefore, the difference (= 3.0 mol. %) can be defined as functionalisation degree of SX MG (Table 3.1). The  $pK_a$  values were also measured. The  $pK_a$  value of SX MG (6.6) was larger than NF MG (6.4) that is due to the acid content consumed during functionalisation.

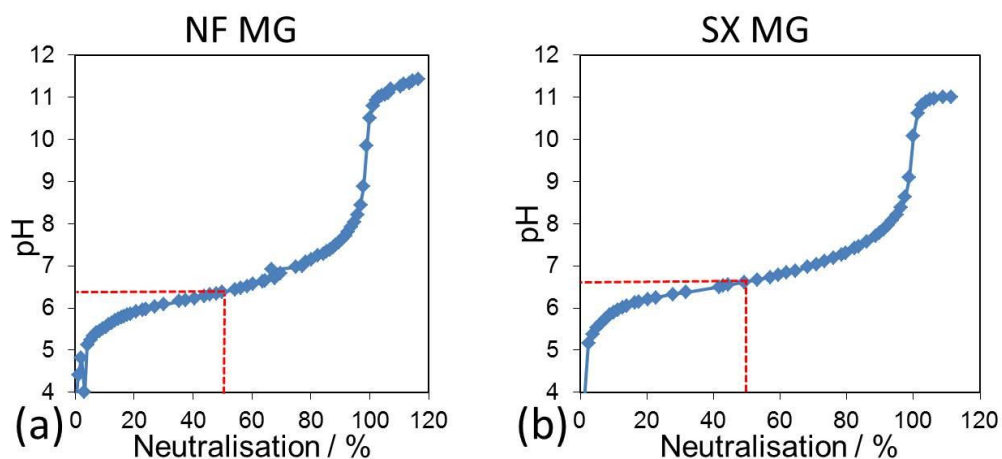


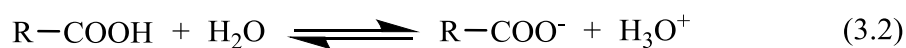
**Fig. 3.2.** Potentiometric titration data for (a) NF MG and (b) SX MG.

The calculation of  $pK_a$  was derived as below:

For the pH of a solution:

$$pH = -\log_{10} [H_3O^+] \quad (3.1)$$

The situation for MG solution is the titration of a weak acid (R-COOH) with a strong base (NaOH). The dynamic equilibrium of R-COOH is represented as following equation:



The  $pK_a$  of R-COOH is:

$$pK_a = -\log_{10} ([H_3O^+][R-COO^-]/[R-COOH]) \quad (3.3)$$

where the symbol of “[ ]” indicate concentrations. The process of titration is adding NaOH to decrease [R-COOH]. At the half way point of the titration, the value of [R-COOH] is equal to [R-COO<sup>-</sup>]. Hence, the  $pK_a$  values of MG are equal to the pH value at 50% neutralisation.

**Table 3.1.** Characterisation data for MGs particles.

Abbreviation	mol.% GMA	$d_{n(SEM)}/$ nm <sup>a</sup>	$d_{h(4)}/$ nm	$d_{h(8)}/$ nm	$Q_{(8)}$	$pK_a$
NF MG	0	120 [10%]	119.4	306.7	16.9	6.4
SX MG	3.0	125 [16%]	120.2	306.5	16.6	6.6

<sup>a</sup> The values in the “[ ]” indicate coefficient of variation.

#### 3.4.1.2 PCS measurements

The swelling properties of NF MG and SX MG particles were examined by PCS measurements over a range of pH values (Fig. 3.3). The pH-responsive curves for both particles were very similar. Considering the very close values for their MAA contents and  $pK_a$  values as shown in Table 3.1, the swelling of particles should not be significantly different. The pH-responsive swelling can be described by using SX MG as an example. The particles at pH = 4 had a hydrodynamic diameter of 120 nm. We defined the particles in this pH as the collapsed state. The particles size,  $d_h$  starts to increase when the pH approaches its  $pK_a$  and then the MG particles exhibited pH-dependent swelling with a maximum diameter at about 310 nm at pH = 7.4. After this pH, the size is constant because the particles swell to most of its maximum volume.

The volume swelling ratio ( $Q$ ) of particles was calculated by the following equation:

$$Q = \left( \frac{d_h(x)}{d_h(4)} \right)^3 \quad (3.4)$$

where  $d_h$  is the hydrodynamic diameter and  $x$  represents the pH value. A volume swelling ratio of 16.6 at pH = 8 can be calculated based on this diameter and that of the fully collapsed particles. According to previously work,<sup>26</sup> this  $Q$  value is suitable for gel formation and can be further considered for biomaterial applications.



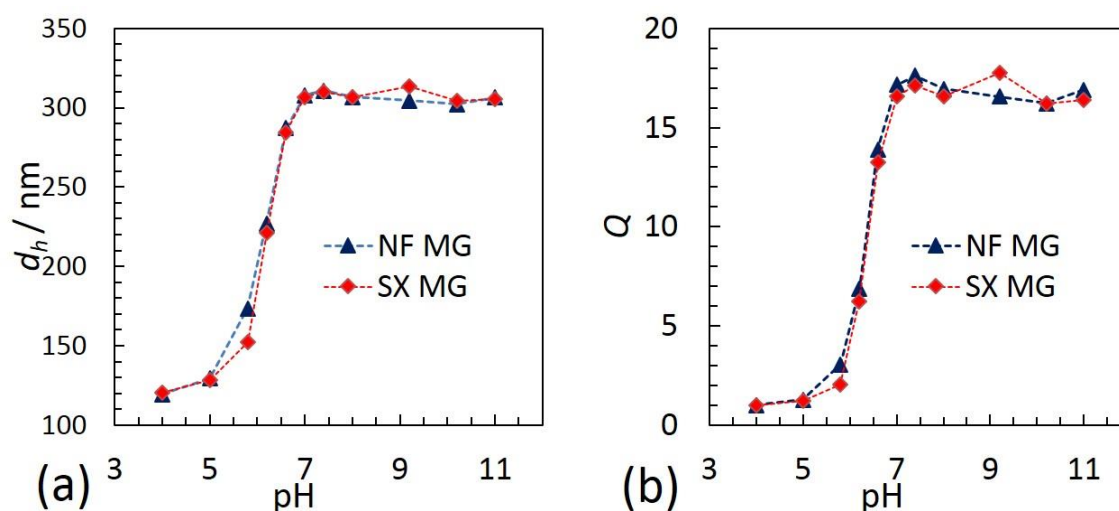


**Fig. 3.3.** (a) Hydrodynamic diameters and (b) particle volume-swelling ratios ( $Q$ ) of NF MG and SX MG in a range of pH from 4 to 11.

### 3.4.1.3 SEM investigations

SEM images were used to observe the size and the morphologies of the MG particles. As shown in Fig 3.4, both NF MG particles and SX MG particles are circular (in 2D) with the size of about 120 nm and 125 nm in diameter, respectively. There was no obvious different observed from the SEM images of the two MGs and so GMA functionalisation did not affect the morphology of MG particles.

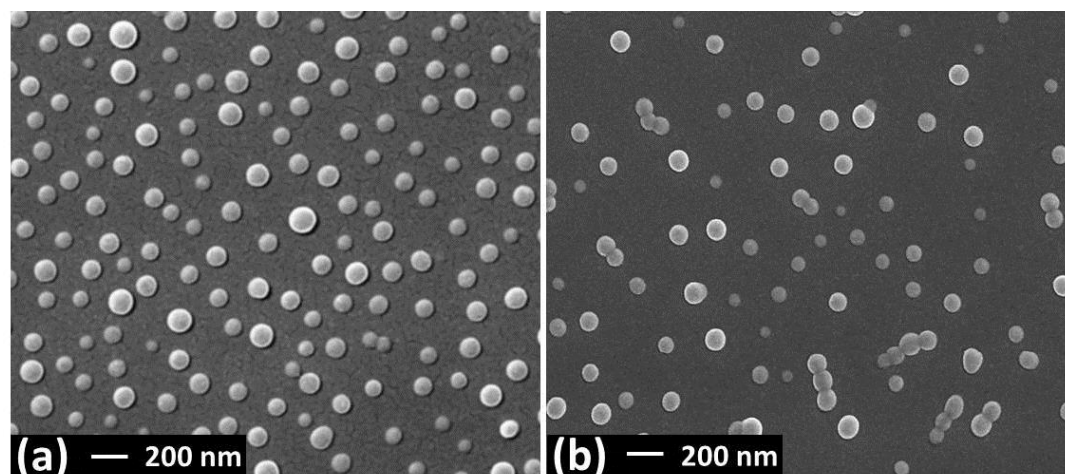


**Fig. 3.4.** SEM images of (a) NF MG and (b) SX MG particles.

One interesting question for SEM samples concerns whether the particles deformed as a consequence of sample preparation? Because it is difficult to deduce from Fig. 3.4 if the particles are pancake shape or spherical shape. The samples were prepared

by slowly drying several dilute MG solution droplets. A cross section SEM was performed (Fig 3.5). The SEM images showed that the particles were slightly deformed when dried on the substrate. The particles in Figure were hemispheres which showed the particles were only deformed in the part which contact to the substrate. Considering platinum coating layer for this sample is about 12 nm, the real diameter of particles is probably slightly lower than  $d_{sem}$ .

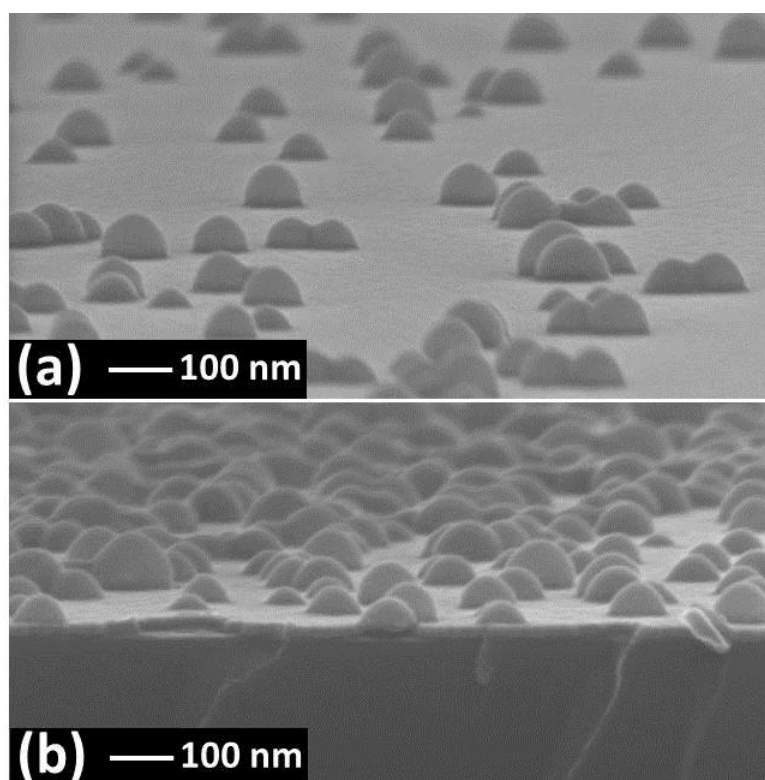


**Fig. 3.5.** SEM images of SX MG cross-section sample. The particles were on a silicon substrate (lower part in (b)). The layer (upper layer in (b)) on the substrate was the platinum coating layer with a thickness of  $\sim 12$  nm.

### 3.4.2 Graphene oxide characterisation

#### 3.4.2.1 SEM and TEM characterisation

The GO solution was synthesised by chemical exfoliation of graphite powder. The as-made GO had inhomogeneous size and number of layers. A TEM image for GO is shown in Fig. 3.6a, and a folded sheet is evident. A representative SEM image (Fig. 3.6b) indicated an average sheet diameter of  $\sim 2$   $\mu\text{m}$ . The morphology of sheet-like GO is as expected and similar to that reported in literature.<sup>27</sup>

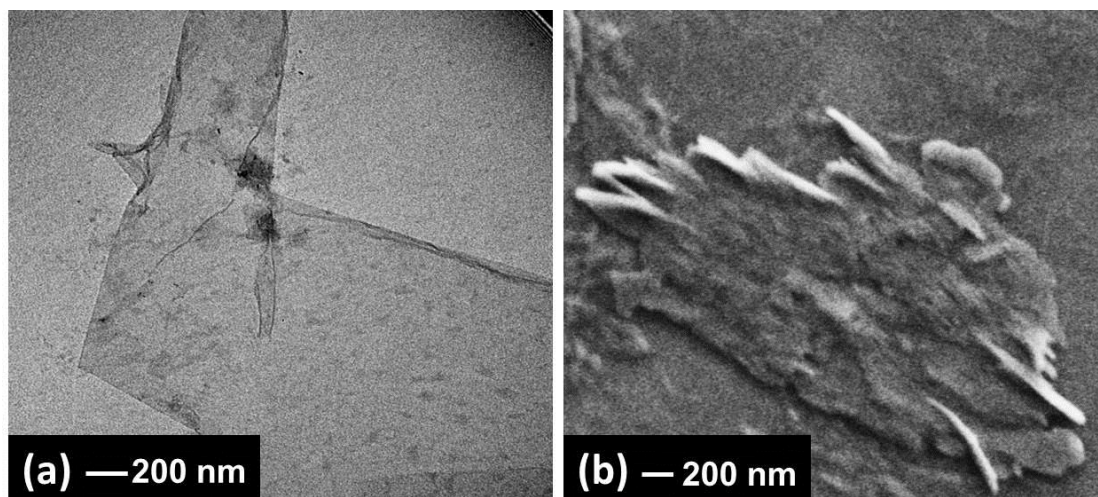


**Fig. 3.6.** (a) TEM image of a GO sheet and (b) SEM image of a GO sheet.

#### **3.4.2.2 Raman spectroscopy**

The Raman spectrum (Fig. 3.7) is typical of that reported for GO<sup>28</sup> and graphite with the G band at  $\sim 1650\text{ cm}^{-1}$  and the D band at  $\sim 1350\text{ cm}^{-1}$ . In Fig 3.7b, the intensity of the D band is similar to the G band while the G band is a much higher and sharper peaks than D band for graphite (Fig. 3.7a). The quality of the “graphene family” materials is normally defined by the D band which indicates the defects on the carbon rings. The G band is due to C-C ( $\text{sp}^2\text{-sp}^2$ ) structures in the graphene layer. The difference in these bands confirmed the reaction of oxidisation broke structure of graphite and showed the evident for the formation of graphene oxide. The combination of these GO properties is consistent with those reported for GO in the literature.<sup>13, 29-30</sup>

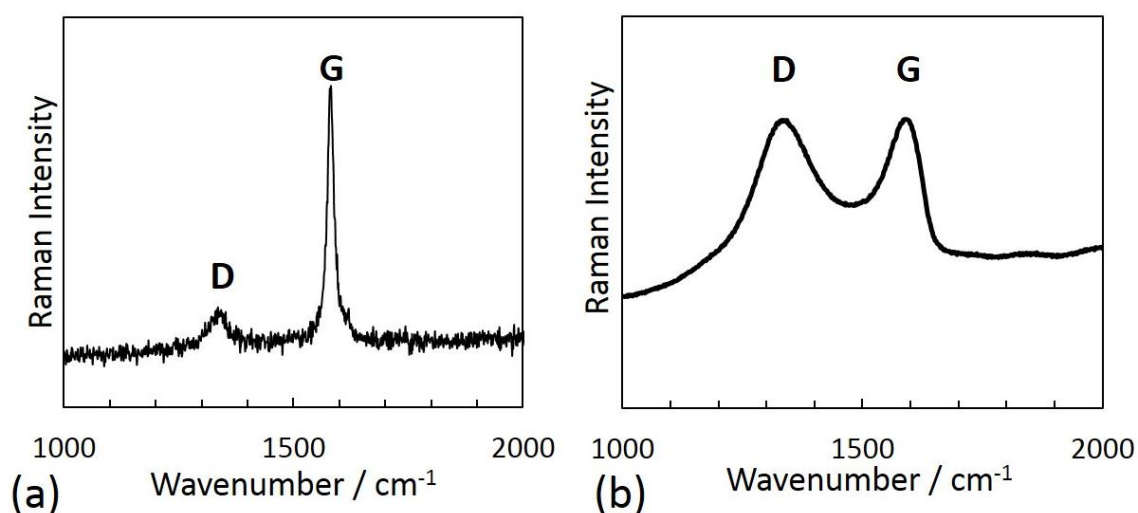


**Fig. 3.7.** Raman spectra for as supplied graphite powder (a) and GO (b). Note that (b) is the normalised Raman spectrum. The unit of Raman intensity is arbitrary unit.

### 3.4.2.3 Gel point of GO dispersion

The GO dispersions are also known to form gels.<sup>31</sup> The gel formation from GO solution might have an effect on the composite gel when mixing with SX MG solution because both GO and MG are negatively charged. The zeta potential measured for GO (0.1 wt.% of 0.001M NaNO<sub>3</sub> solution,) was - 63.5 mV, and this suggests a very strong negative charge for GO sheets in water. To study the gel point of GO solution, a tube inversion experiment was performed. The images of tubes containing different GO concentrations ( $C_{GO}$ ) for this study are shown in Fig. 3.8. It is shown that the GO solution can form a gel when the  $C_{GO}$  approach to 0.4 wt.%

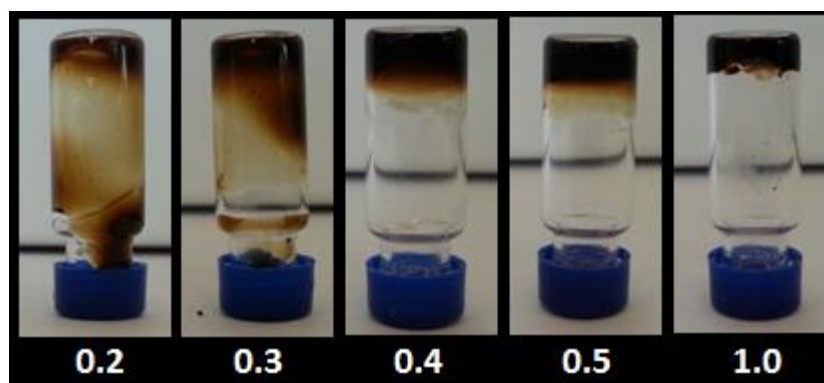


**Fig. 3.8.** Digital photographs of GO water dispersions. The concentrations in wt.% are shown in white values.

### 3.4.3 Composite gel characterisation

The SX MG/GO composite gels were prepared by blending the SX MG and GO dispersions. The composites were abbreviated as SX MG/GO<sub>x</sub> or DX MG/GO<sub>x</sub>, which represent the composite dispersion or chemical gel, respectively. The value of *x* represents the total weight concentration of GO. The concentration of MG was 10 wt.% and was constant. The physical gel formation of SX MG/GO<sub>x</sub> (Fig. 3.9a) was achieved by increasing the pH from ~4.3 (as prepared) to ~7.2 with a colour change from brown to dark brown. The colour change is due to the MG particles becoming transparent at high pH, exposing the original colour of the GO dispersion. At pH = 4.3 (< *pK<sub>a</sub>* of the MG particles), the SX MG/GO dispersions were free-flowing fluid (Fig. 3.9a). The fluid-to-gel transition of occurred (Fig. 3.9b) when increasing the pH to 7.2 (> *pK<sub>a</sub>*). In this state the swollen MG particles filled most of the space and prevented translation of nearest-neighbour particles (and GO) due to excluded volume effects. The SX MG/GO gels at pH of 7.2 could be injected through a narrow gauge syringe (1.1 × 50 mm, diameter × length) and were able to be molded into shapes after injection (Fig. 3.9b). The injectability is essential for a possible medical material. The DX MG/GO composite gel could be achieved by heating the SX MG/GO physical gel in the presence of APS (Fig. 3.9c).

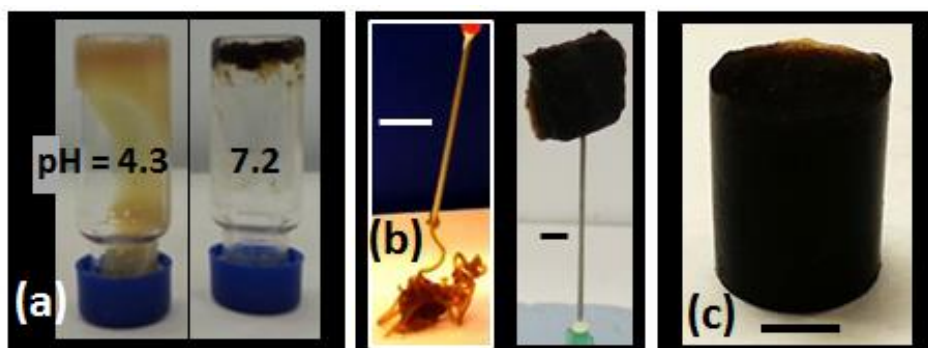


**Fig. 3.9.** Digital photos of composites, (a) The pH-triggered fluid-to-gel transition of SX MG/GO<sub>0.50</sub>. (b) The SX MG/GO gels were injectable and also mouldable as can be seen from the SX MG/GO<sub>1.0</sub> gel. (c) DX MG/GO gels were prepared as cylinders by using DX MG/GO<sub>1.0</sub> gel as an example. The scale bars for (b) and (c) are 5 mm.



### 3.4.3.1 Morphology of composite gel

The morphology of the freeze-dried DX MG/GO gels were studied by SEM. The GO free gel was also studied as a control. Fig. 3.10a and 3.10b show SEM image for freeze-dried DX MG/GO<sub>1.0</sub> in the as-made state. Fig. 3.10c and 3.10d show the freeze-dried DX MG gel. The morphologies for both gels were porous and typical of that reported for freeze-dried hydrogel or conventional hydrogel / GO composites<sup>32-34</sup>.

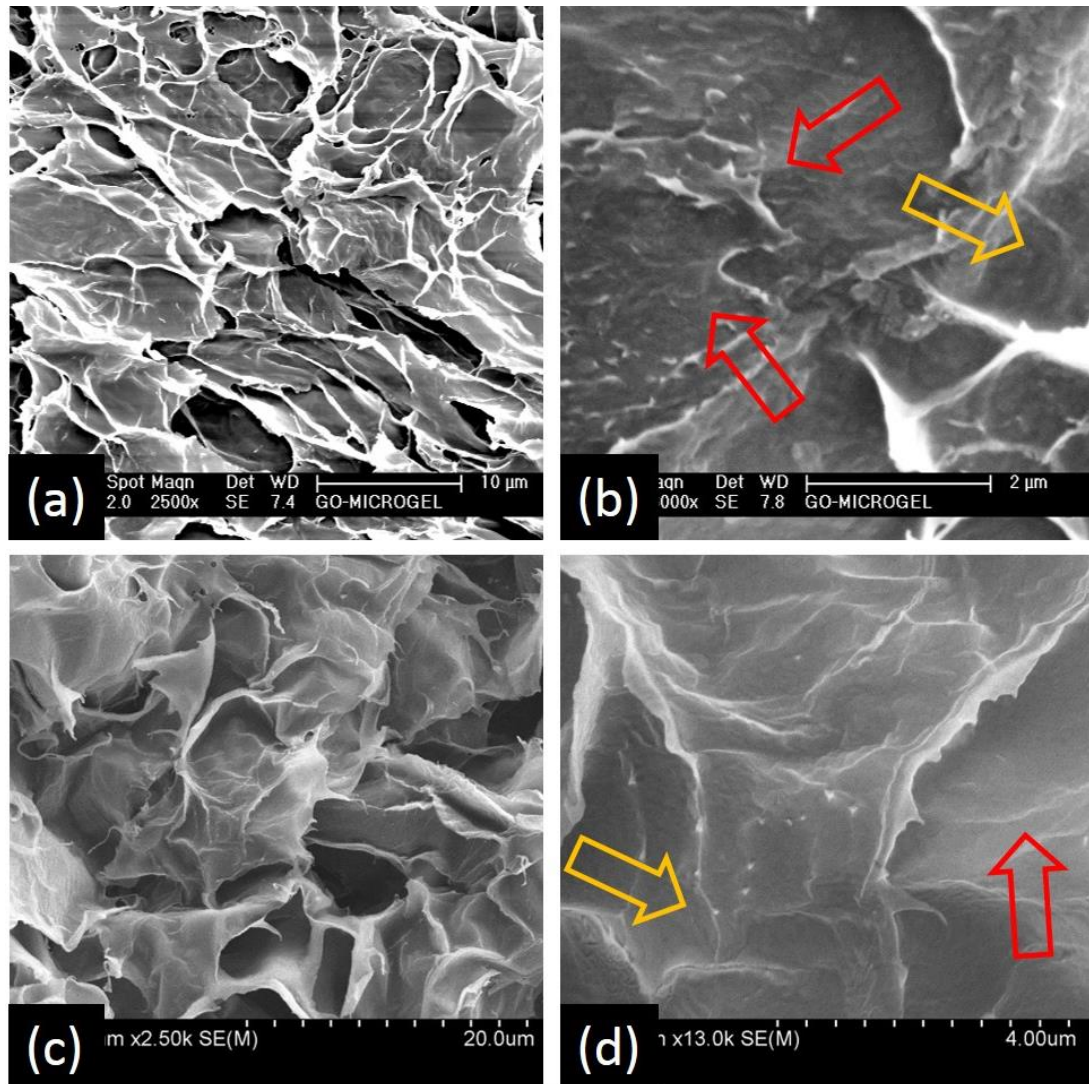


**Fig. 3.10.** SEM of DX MG/GO<sub>1.0</sub> gel ((a) and (b)) and DX MG ((c) and (d)). (b) and (d) are higher magnification images. The yellow arrows show the spherical particles on the gel surface. The red arrows indicate the different roughness on the surfaces of gel walls.

The spherical particles for both gels can be seen on the surface as shown in Fig. 3.10b and 3.10d. Because the morphology of composite DX gel and GO free DX gel

are very similar, the GO sheets were less evident to see. One possible evidence of GO in Fig 3.10b is that the surfaces of gel wall for DX MG/GO<sub>1.0</sub> are rougher (red arrows) than the ones shown for DX MG (red arrows in 3.10d). The presence of GO prevented forming smooth surface when the gels were freeze dried.

### 3.4.3.2 Thermogravimetric analysis and SEM of heat-triggered DX MG/GO

As shown in Fig 3.10, the GO sheets were hidden in the MG matrix. In order to reveal the structure of GO sheets without the presence of MG, a freeze-dried DX MG/GO<sub>1.0</sub> hydrogel was heated at 550°C under N<sub>2</sub> for 1 h to remove most of MG component. This process was conducted because GO has superior thermal stability compare to conventional polymers<sup>35</sup>. After the heating process, ~ 10 % of mass remained and we estimated most of them are from GO sheets (Fig 3.12). During the thermal treatment, the GO sheets might be reduced to graphene sheets. SEM images (Fig. 3.11) showed the evident that some of the graphene-like sheets were exposed. The exposed GO sheets had a space-filling morphology. This morphology supports our proposal that they formed a percolated network throughout the DX MG/GO gels.

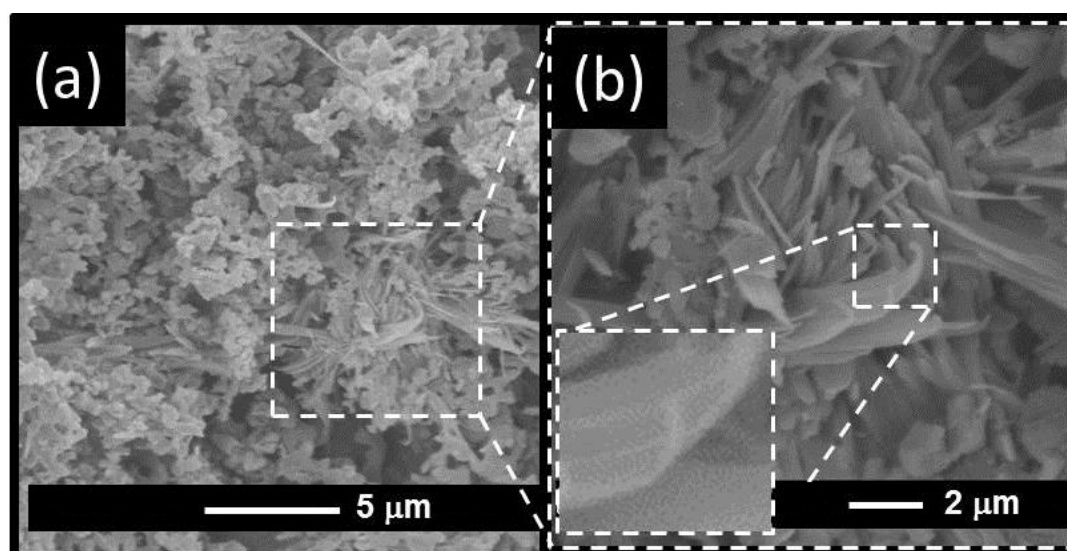


**Fig. 3.11.** SEM Images are shown for freeze-dried DX MG/GO<sub>1.0</sub> after being heated to 550°C under N<sub>2</sub>. The inset for (b) shows GO sheets.

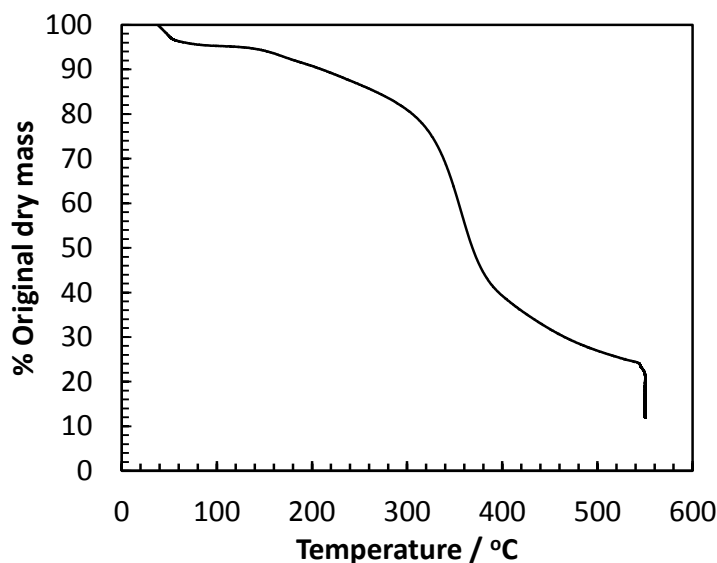


**Fig. 3.12.** Thermo gravimetric analysis data for DX MG/GO<sub>1.0</sub>. The sample was heated under a nitrogen atmosphere, and the temperature was maintained at 550 °C after the heating ramp was completed.

### 3.4.3.3 Frequency sweep dynamic rheology

The mechanical properties of GO dispersion and SX MG/GO and DX MG/GO gels were studied using dynamic rheology measurements. The frequency-sweep dynamic rheology data for GO dispersion, SX MG/GO and DX MG/GO gels are shown in Fig. 3.13a, b and c, respectively. For these systems, the storage modulus ( $G'$ ) is greater than the loss modulus ( $G''$ ) invariably. The moduli followed the order: DX > SX > GO with the same values of  $C_{GO}$ , and the  $G'$  and  $G''$  value were weakly frequency dependent. Therefore, we can consider those gels as viscoelastic solids. The  $G'$  and  $G''$  are known as following a power law<sup>36-39</sup>:

$$G' \sim G'' \sim \omega^{n'} \quad (3.5)$$

Where  $\omega$  is the oscillation frequency, and  $n'$  is called frequency exponent or relaxation exponent.

Here, the value for  $n'$  can be seen as a measure of viscoelastic behaviour of gels. In Fig. 3.13d, we used the frequency dependence behaviour of  $G'$  and  $G''$  in Fig 3.13 a-



c to fit the power law, and the values for  $n'$  were plotted versus  $C_{GO}$  in Fig .3.13d which showed a decreasing order that  $GO > SX\ MG/GO > DX\ MG-GO$ . The small value for  $n'$  is related to the elastic networks structure and viscoelastic properties.<sup>40</sup> The presence of swelled MG particles (to form  $SX\ MG/GO$ ) occupied most of the space in the composites (with considerable excluded volume), which resulted in a more discontinuous GO phase compare to GO dispersion. When the  $SX$  gels were covalently inter-linked to form  $DX\ MG/GO$ , the GO become further discontinuous. These results indicate that the presence of covalently inter-linked MG particles significant reduced the freedom of GO which leads to a more elastic response to the applied strain and a lower  $n'$  value. Both experimental observations (Fig. 3.9a) and rheology data showed that the GO dispersions were very viscous and formed gels. We conclude from the rheology data that percolation concentration for GO in MG dispersion should be lower than 0.25 wt.%. This conclusion is consistent with similar results from Vasu et al.<sup>31</sup>

The values for  $G'$  and  $G''$  provide measures of the proportion of energy stored and dissipated, respectively, per unit strain<sup>41</sup>. They are the elastic and viscous modulus, respectively. The behaviours of  $G'$  with the same  $C_{GO}$  in Fig. 3.13e have an order that  $GO < SX\ MG/GO < DX\ MG-GO$ , it followed what we observed above which caused by the physical and covalent gel formation. Moreover, the  $G'$  was also increased by increasing  $C_{GO}$  as more rigid components were introduced, as expected.

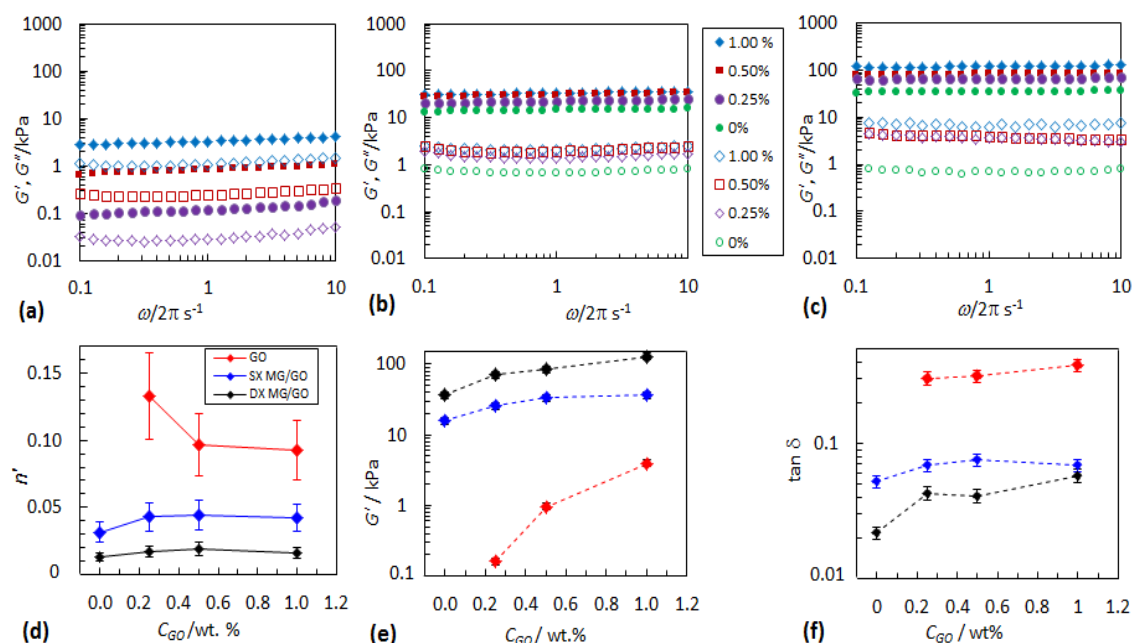


**Fig. 3.13.** Frequency-sweep studies for various gels containing GO. (a), (b) and (c) showed the  $G'$  (close symbols) and  $G''$  (open symbols) data in a range of frequency for GO dispersion, SX MG/GO physical gels and DX MG/GO gels, respectively. (c), (d) and (e) showed the relaxation component,  $G'$  and  $\tan \delta$  as the function of  $C_{GO}$ . The legend in (b) applied to (a) and (c). The legend in (d) applied to (e) and (f).

The value for  $\tan \delta$  is proportion to the energy dissipated by the gel under strain if  $G'$  is constant. In Fig 3.13f, the pure GO dispersion has greatest  $\tan \delta$  values because the GO sheets in dispersion were weakly linked together. Because the attractive interactions of GO sheets are from Van der Waals interaction and hydrogen bonding,<sup>42-43</sup> both of which are weaker than the covalent bonds. Therefore, the GO gels showed a most viscous behaviour. Compared to GO gels, the inclusion of swelled MG particles (SX MG/GO) greatly decreased  $\tan \delta$  (Fig. 3.13f) and another significant decrease was caused by the DX process. The physical and covalently interlinked MG particle matrixes were both effective in decreasing dissipation and must have greatly restricted the ability of the GO sheets to move in response to strain. Another discovery from Fig 3.13f is that the  $\tan \delta$  of DX MG/GO was increased as the  $C_{GO}$  increased.  $\tan \delta$  of DX MG/GO<sub>1.0</sub> was much lower than DX MG. Therefore, we proposed that the GO sheets were not involved in the covalent inter-crosslinking.

Instead, they caused a greater degree of movement within the DX MG/GO gels (and hence increased dissipation).

#### **3.4.3.4 Strain sweep dynamic rheology**

Strain-sweep dynamic rheology of GO was performed to study the strain-induced network breaking mechanism of gels. The data for GO dispersions, SX MG/GO and DX MG/GO were shown in Fig 3.14a – c, respectively. For ideal polymer networks, the  $G'$  was constant at low strain and started to decrease at the strain where the polymer network starts to fail. The relative  $G''$  was constant at low strain and started to increase to a maximum value (i.e. the gel point) and then decrease. The critical point is also defined where  $G'$  and  $G''$  crossed. It usually indicates the breakdown of gel structure occur when  $\tan \delta = 1$ . This phenomenon can be seen in Fig 3.14b and 3.14c. Conversely, the GO gels (Fig. 3.14a) had low ductility in that  $G'$  cannot keep constant and decreased at about 0.2%. This tendency for  $G'$  to decrease at low strain for GO gels was reported by Vasu et al.<sup>31</sup> Besides, no clearly evidence for a maxima of  $G''$  for GO gels can be found and both the  $G'$  and  $G''$  data were both decrease with increasing strain.

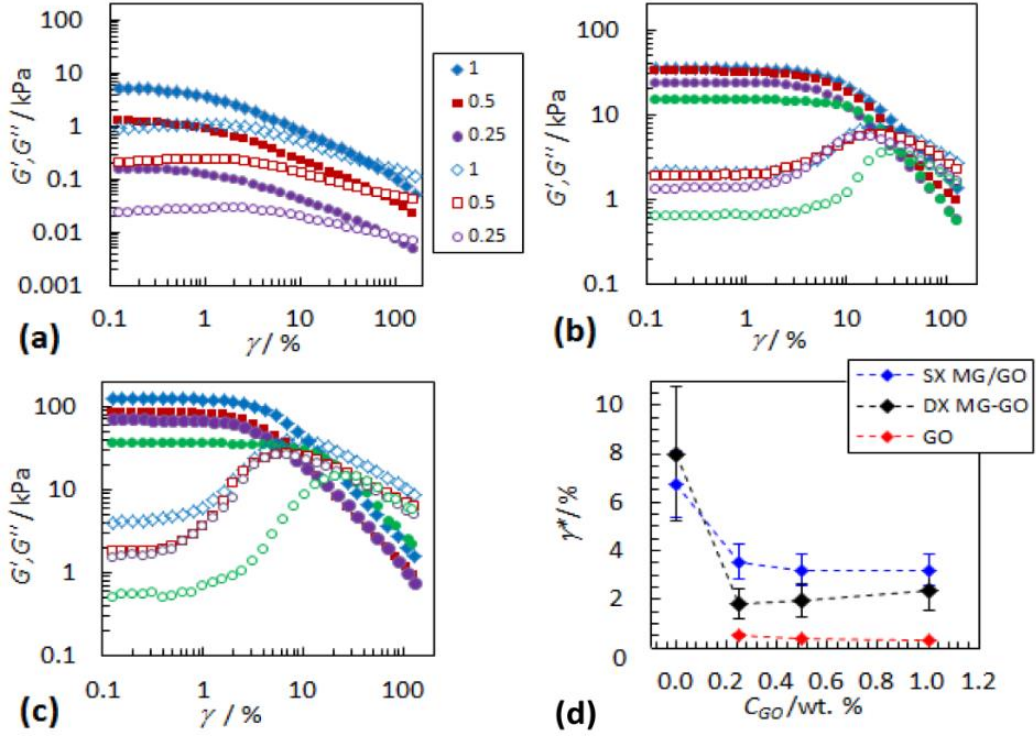


**Fig. 3.14.** Strain-sweep data showing the variation of  $G'$  (closed symbols) and  $G''$  (open symbols) with strain ( $\gamma$ ) are shown for GO (a), SX MG/GO (b) and DX MG/GO (c). The legend for (a) applies to (b) and (c). (d) shows the  $\Delta G''_n$  (see text) dependence on GO concentration ( $C_{GO}$ ). (e) shows the variation of the yield strain ( $\gamma^*$ ) with  $C_{GO}$ .

The cross-over of  $G'$  and  $G''$  (i.e.  $\tan \delta = 1$ ) is used as a measure of ductility. However, as the behaviour of GO gel is unified with composite gels, we applied another general approach for brittle viscoelastic solids<sup>44</sup> to study the ductility of gels. We define a yield strain ( $\gamma^*$ ) at where modulus was reduced by 10% compared to the initial value. The data for  $\gamma^*$  were plotted in Fig 3.14d, and it shows that the GO gels were very brittle, which is due to the percolated network of stiff GO sheets. The inclusion of GO and the continuous MG phase provide the highest  $\gamma^*$  value for SX MG/GO gels. However, the ductility of SX MG/GO is less than SX MG which also due to the inclusion of stiff phase. The  $\gamma^*$  value for DX MG/GO were in the middle of SX MG/GO and GO dispersion which due to the covalent MG phase have less ability to restore the gel structure under excessive strain. Moreover, the  $\gamma^*$  value for SX MG/GO and DX MG/GO gels do not significantly depend on the  $C_{GO}$  values.

These data matched with our early proposal that a percolated GO network was contained in MG particle phase. It suggests that the failure mechanism of both SX MG/GO and DX MG/GO are more similar to GO gels. Considering these results and the size of GO sheets, we think that the GO sheets were not involved in the crosslinking of MG gel phase.

#### **3.4.3.5 Isostrain condition for DX/MG composite.**

We consider the composites had two phases: the DX MG phase which can be seen as the hydrogel matrix, and the GO phase which can be seen as the stiff reinforcement. Two models were widely used to describe the mechanical properties of a biphasic composite which are the isostrain and isostress models. Considering the discussion above it suggests that there is a lack of interaction between GO and MG and the modulus linearly increased with the GO concentration. The isostrain model that assumes the interaction between filler and matrix is in a perfect condition that the stress can transfer between filler and matrix without loss. For the DX MG/GO composites, it consists of a relatively low modulus phase (MG phase) dispersed within a high modulus phase (GO sheets). The isostrain model can be applied using the following equation:

$$G' = G'_{GO}\Phi_{GO} + G'_{MG}\Phi_{MG} \quad (3.6)$$

where the  $G'$  is the storage modulus of the composite, and the  $G'_{GO}$  and  $G'_{MG}$  are the storage moduli for GO and DX MG, respectively. The  $\Phi_{GO}$  and  $\Phi_{MG}$  are the volume fractions of GO and DX MG gel networks.

For the biphasic composite system:

$$\Phi_{GO} + \Phi_{MG} = 1 \quad (3.7)$$

The  $\Phi_{GO}$  can be calculated from  $C_{GO}$  using the following equation (3.9) by assuming the density of GO ( $\rho_{GO}$ ) and MG ( $\rho_{MG}$ ) are 1.2 and 1.8 g cm<sup>-3</sup>, respectively.<sup>1, 15</sup>

$$C_{GO} = \frac{100 \rho_{GO} \Phi_{GO}}{\rho_{GO} \Phi_{GO} + \rho_{MG} \Phi_{MG}} \quad (3.8)$$

Put equation (3.7) into (3.8) and rearrange, we get:

$$\Phi_{GO} = \frac{1}{1 + \frac{\rho_{GO}}{\rho_{MG}} \times \frac{100 - C_{GO}}{C_{GO}}} \quad (3.9)$$

The equation (3.6) can be derived by following steps:

$$\begin{aligned} G' &= G'_{GO} \Phi_{GO} + G'_{MG} \Phi_{MG} \\ &= G'_{GO} \Phi_{GO} + G'_{MG} (1 - \Phi_{GO}) \\ &= G'_{MG} + \Phi_{GO} (G'_{GO} - G'_{MG}) \end{aligned} \quad (3.10)$$

Here, we can plot  $G'$  versus  $\Phi_{GO}$  by using our experimental data. A linear curve was shown in Fig. 3.15 which fitted equation (3.10) ( $R^2 = 0.97$ ,  $R^2$  is coefficient of determination). The values of 14.67 MPa and 36.3 kPa for  $G'_{GO}$  and  $G'_{MG}$  were calculated by using the gradient and intercept. The value for  $G'_{MG}$  matches the earlier work in our group.<sup>1</sup> However, the value for  $G'_{GO}$  was much lower than what is reported. Dikin et al.<sup>15</sup> reported a tensile modulus of 32 GPa for “GO paper”, which is four orders of magnitude higher than  $G'_{GO}$ .

The reason why  $G'_{GO}$  is much lower is that the GO sheets were dispersed within a gel. The MG-GO and GO-GO were not tightly contacted, and the GO sheets had freedom to move under strain. The interactions that transfer stress between the GO sheets and DX MG domains most likely involve water-mediated hydrogen bonding and also reversible hydrophobic interactions. These interactions were very inefficient

to transfer or distribute the load within the DX MG/GO gels compared to dry GO paper.<sup>15</sup>

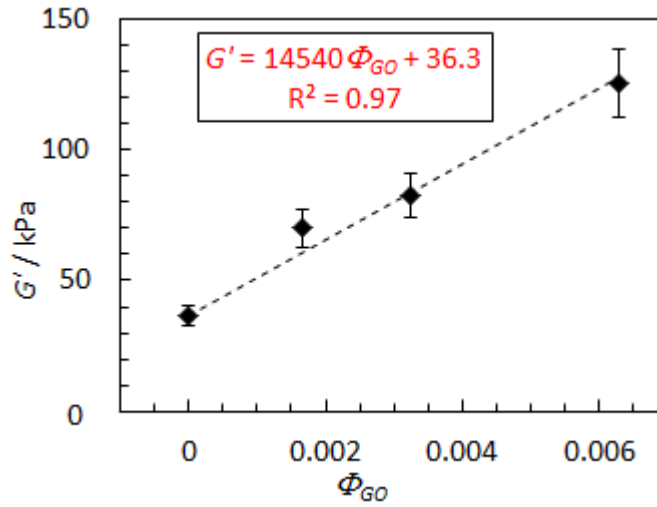


**Fig. 3.15.** The fitting curve of storage modulus on the volume fraction of GO within the DX MG/GO network.

#### 3.4.3.6 Static axial compression tests

Static axial compression tests were performed for DX gels to further study their mechanical properties. The stress versus extension ratio data for selected samples with different  $C_{GO}$  is shown in Fig. 3.16a which gave an idea of the distinction from various  $C_{GO}$ . The extension ratio,  $\lambda$  can be calculated by:

$$\lambda = 1 - \varepsilon \quad (3.11)$$

Where  $\varepsilon$  is the strain. For the DX MG/GO composites, the average data for strain at break ( $\varepsilon_{max}$ ), stress at break ( $\sigma_{max}$ ) and compression modulus ( $E$ ) as a function of  $C_{GO}$  were shown in Fig 3.16b and c. The  $\varepsilon_{max}$  values can be used to measure the ductility of materials. The data showed that DX MG has the highest value for  $\varepsilon_{max}$  while the data for the DX MG/GO gels is lower. For the DX MG/GO gels in Fig 3.16b, the value of  $C_{GO}$  did not significantly affect the  $\varepsilon_{max}$  values. However, the values of  $\sigma_{max(T)}$  were increased by  $C_{GO}$ . The trend of  $\varepsilon_{max}$  followed what was found in strain-sweep rheology data (Fig 3.14d).

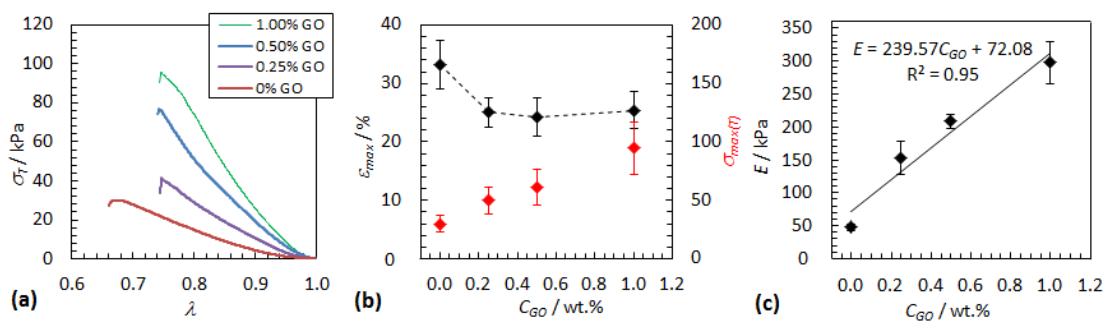


**Fig. 3.16.** Static compression data for various gels. (a) shows the selected stress versus extension ratio ( $\lambda$ ) curves for different DX MG/GO gels. (b) shows the effects of GO concentration on the maximum strain ( $\epsilon_{max}$ ) and maximum true stress ( $\sigma_{T(max)}$ ). The variation of modulus with  $C_{GO}$  is shown in (c).

The values for  $E$  were calculated from the gradients of the initial 10% part of stress-strain curves. The plot of  $E$  versus  $C_{GO}$  was shown in Fig. 3.16c which showed a linear relationship. This trend also followed the trend of  $G'$  established from rheology. From this trend, it is clear that the modulus of DX MG/GO can be tuned by controlling  $C_{GO}$ , which could be useful in the context of IVD repair.<sup>8</sup> We also achieve a highest  $E$  value at present (DX MG/GO<sub>1.0</sub>) in the DX MG system.

#### 3.4.3.7 Live / dead assay of DX composite gel

Since the DX MG/GO gels are designed for future application in soft tissue repair applications, a preliminary biocompatible test was performed. The biocompatibility of DX MG/GO<sub>0.5</sub> gels was investigated by culturing human NP cells in direct contact with composites for ten days and cell viability was assessed by live / dead assay (Fig. 3.17 and Fig. 3.18). Annular DX MG/GO<sub>0.5</sub> composites (Fig 3.17h) were introduced into 24-well culture plates containing cultures of human NP cells on glass coverslips. Live cells in the assay are distinguished by the presence of calcein (green) whereas, dead cells are stained with ethidium homodimer-1 (red). Fig. 3.17a - c shows live / dead assay fluorescent microscopy images of NP cells in contact with the gel and a very high proportion of live cells were evident (greater than  $\sim 95\%$  from our images). Fig. 3.18a - c shows the adherence and morphology of NP cells in culture with the



DX MG-GO<sub>0.50</sub> composite. It follows that there was a high proportion of viable, adherent NP cells present after ten days of culture in direct contact with DX MG/GO<sub>0.50</sub>. The biocompatibility of DX MG-GO can be expected under this condition. This result is similar to the result for GO-free DX MGs.<sup>8</sup>

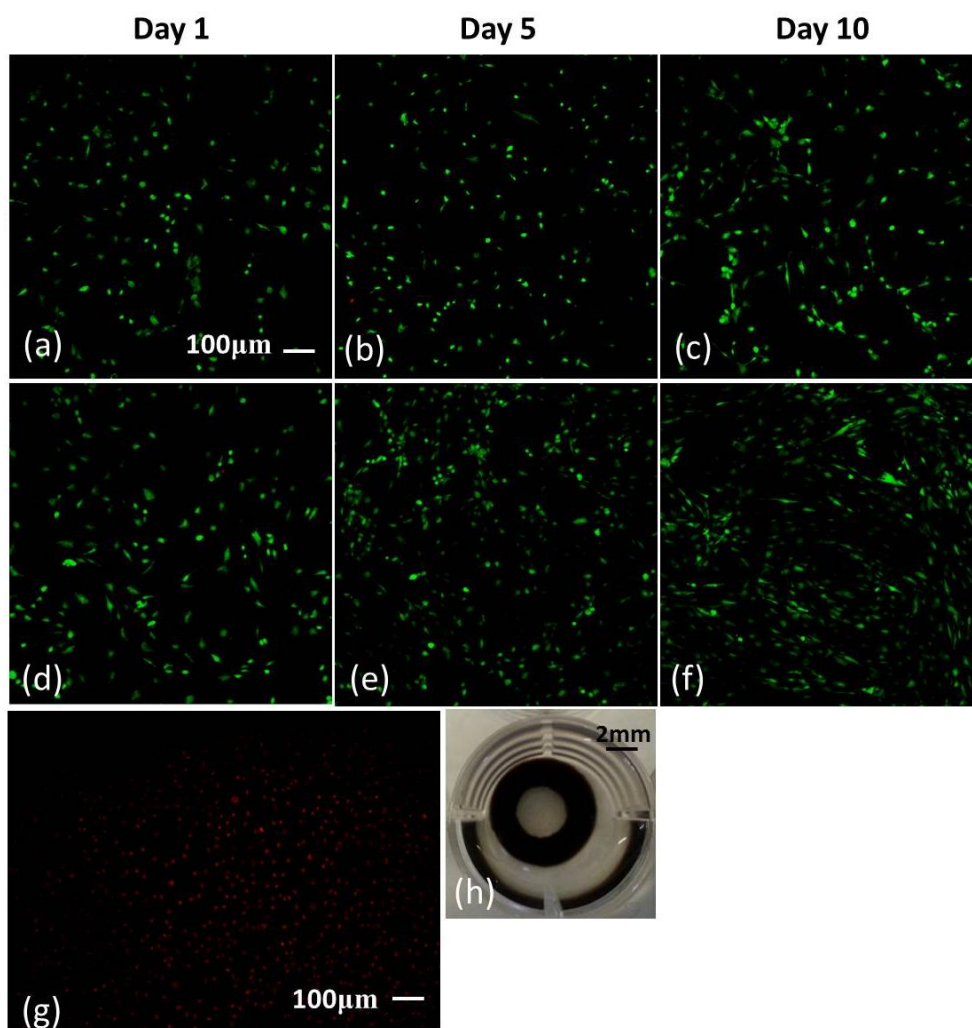


**Fig. 3.17.** Cell challenge experiments for DX MG/GO gels. Live / Dead assays for Nucleus pulposus cells contacted DX MG/GO<sub>0.5</sub> in a period of 10 days (a) – (c), the Live control samples are shown in (d) – (f) and the dead control sample is shown in (g). Nucleus pulposus cells contacted DX MG/GO<sub>0.5</sub> under a toroid-shaped gel (h) in a well plate.

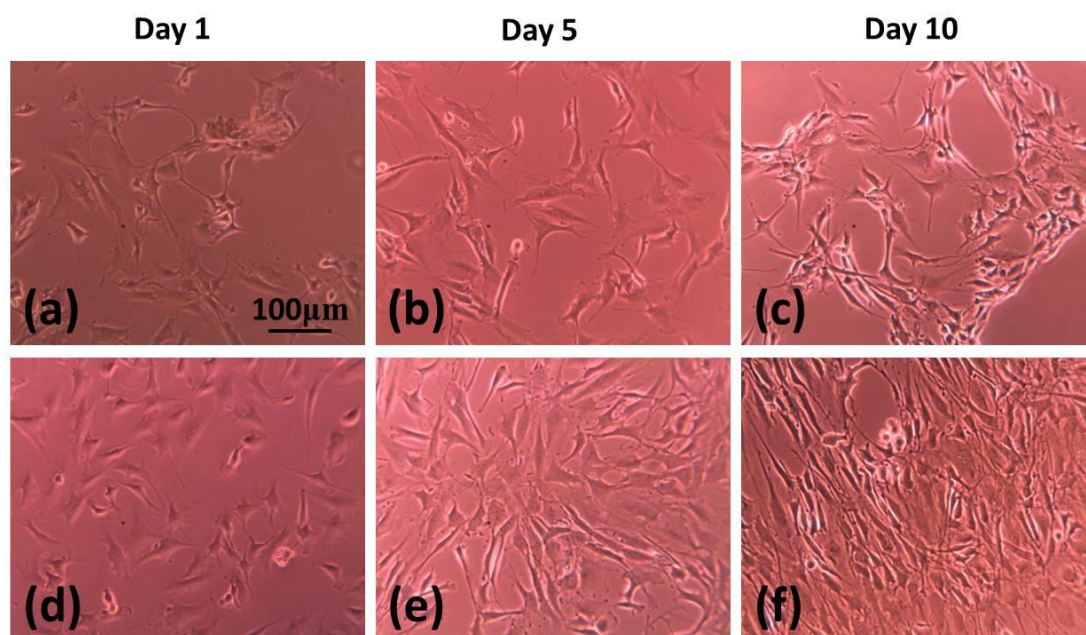


**Fig. 3.18.** The morphology of cells in Live / Dead assays. The Nucleus pulposus cells contacted DX MG/GO<sub>0.5</sub> in a period of 10 days (a) – (c), the Live control samples are shown in (d) – (f).

### 3.5 Conclusions

In this chapter, a new composited material containing pH-responsive MG and GO was studied. The morphology and mechanical properties of both SX MG/GO and DX MG/GO were studied. The good dispersion of GO sheets in MG phase was confirmed by SEM. The modulus values ( $G'$  and  $E$ ) for DX MG/GO were found to be proportional to  $C_{GO}$ . The modulus values can be tuned to about five times more than GO-free sample with only 1 wt.% of GO introduced. The modulus data could be described by using an isostrain model. The high modulus values for the SX MG/GO guarantee they could form mouldable gels. Besides, the shear thinning properties of SX MG/GO also guarantee the injectability. The inclusion of GO changed the failure mechanism for the gels to one that resembled that of pure GO gels. The results of live / dead assay showed that the DX MG/GO<sub>0.5</sub> gel was not cytotoxic to NP cells. Considering the excellent mechanical performance of these novel gel composites, they can be considered as a promising candidate for injectable load-supporting soft tissue repair therapies in the future.

### 3.6 References

1. Liu, R.; Milani, A. H.; Freemont, T. J.; Saunders, B. R., Doubly crosslinked pH-responsive microgels prepared by particle inter-penetration: swelling and mechanical properties. *Soft Matter* **2011**, 7, 4696-4704.
2. Richtering, W.; Saunders, B. R., Gel architectures and their complexity. *Soft Matter* **2014**, 10, 3695-702.
3. Shin, S. R.; Aghaei-Ghareh-Bolagh, B.; Dang, T. T.; Topkaya, S. N.; Gao, X.; Yang, S. Y.; Jung, S. M.; Oh, J. H.; Dokmeci, M. R.; Tang, X. S.; Khademhosseini, A., Cell-laden microengineered and mechanically tunable hybrid hydrogels of gelatin and graphene oxide. *Adv. Mater.* **2013**, 25, 6385-91.
4. Haraguchi, K.; Takehisa, T., Nanocomposite Hydrogels: A Unique Organic–Inorganic Network Structure with Extraordinary Mechanical, Optical, and Swelling/De-swelling Properties. *Adv. Mater.* **2002**, 14, 1120-1124.
5. Therien-Aubin, H.; Wu, Z. L.; Nie, Z.; Kumacheva, E., Multiple shape transformations of composite hydrogel sheets. *J. Am. Chem. Soc.* **2013**, 135, 4834-9.
6. Gong, J., Why are double network hydrogels so tough? *Soft Matter* **2010**, 6, 2583-2590.
7. Lane, T.; Holloway, J. L.; Milani, A. H.; Saunders, J. M.; Freemont, A. J.; Saunders, B. R., Double network hydrogels prepared from pH-responsive doubly crosslinked microgels. *Soft Matter* **2013**, 9, 7934-7941.
8. Milani, A. H.; Freemont, A. J.; Hoyland, J. A.; Adlam, D. J.; Saunders, B. R., Injectable doubly cross-linked microgels for improving the mechanical properties of degenerated intervertebral discs. *Biomacromolecules* **2012**, 13, 2793-801.
9. Chabot, V.; Higgins, D.; Yu, A.; Xiao, X.; Chen, Z.; Zhang, J., A review of graphene and graphene oxide sponge: material synthesis and applications to energy and the environment. *Energy Env. Sci.* **2014**, 7, 1564-1596.
10. Balandin, A. A., Thermal properties of graphene and nanostructured carbon materials. *Nat. Mater.* **2011**, 10, 569-581.
11. Maiti, U. N.; Lee, W. J.; Lee, J. M.; Oh, Y.; Kim, J. Y.; Kim, J. E.; Shim, J.; Han, T. H.; Kim, S. O., 25th Anniversary Article: Chemically Modified/Doped Carbon Nanotubes & Graphene for Optimized Nanostructures & Nanodevices. *Adv. Mater.* **2014**, 26, 40-67.

12. Rafiee, M. A.; Rafiee, J.; Wang, Z.; Song, H.; Yu, Z.-Z.; Koratkar, N., Enhanced Mechanical Properties of Nanocomposites at Low Graphene Content. *ACS Nano* **2009**, 3, 3884-3890.
13. Young, R. J.; Kinloch, I. A.; Gong, L.; Novoselov, K. S., The mechanics of graphene nanocomposites: A review. *Comp. Sci. Tech.* **2012**, 72, 1459-1476.
14. Lerf, A.; He, H.; Forster, M.; Klinowski, J., Structure of Graphite Oxide Revisited || . *J. Phys. Chem. B* **1998**, 102, 4477-4482.
15. Dikin, D. A.; Stankovich, S.; Zimney, E. J.; Piner, R. D.; Dommett, G. H.; Evmenenko, G.; Nguyen, S. T.; Ruoff, R. S., Preparation and characterization of graphene oxide paper. *Nature* **2007**, 448, 457-60.
16. Huang, Y.; Zhang, M.; Ruan, W., High-water-content graphene oxide/polyvinyl alcohol hydrogel with excellent mechanical properties. *J. Mater. Chem. A* **2014**, 2, 10508-10515.
17. Cong, H. P.; Wang, P.; Yu, S. H., Highly elastic and superstretchable graphene oxide/polyacrylamide hydrogels. *Small* **2014**, 10, 448-53.
18. Bai, H.; Li, C.; Wang, X.; Shi, G., A pH-sensitive graphene oxide composite hydrogel. *Chem. Comm.* **2010**, 46, 2376-8.
19. Layek, R. K.; Nandi, A. K., A review on synthesis and properties of polymer functionalized graphene. *Polymer* **2013**, 54, 5087-5103.
20. Liu, J.; Cui, L.; Losic, D., Graphene and graphene oxide as new nanocarriers for drug delivery applications. *Acta Biomater.* **2013**, 9, 9243-9257.
21. Qu, G.; Wang, X.; Liu, Q.; Liu, R.; Yin, N.; Ma, J.; Chen, L.; He, J.; Liu, S.; Jiang, G., The ex vivo and in vivo biological performances of graphene oxide and the impact of surfactant on graphene oxide's biocompatibility. *J. Environ. Sci.* **2013**, 25, 873-881.
22. Chung, C.; Kim, Y.-K.; Shin, D.; Ryoo, S.-R.; Hong, B. H.; Min, D.-H., Biomedical Applications of Graphene and Graphene Oxide. *Acc. Chem. Res.* **2013**, 46, 2211-2224.
23. Hummers, W. S.; Offeman, R. E., Preparation of Graphitic Oxide. *J. Am. Chem. Soc.* **1958**, 80, 1339-1339.
24. Dalmont, H.; Pinprayoon, O.; Saunders, B. R., Study of pH-Responsive Microgels Containing Methacrylic Acid: Effects of Particle Composition and Added

Calcium. *Langmuir* **2008**, 24, 2834-2840.

25. Reis, A. V.; Fajardo, A. R.; Schuquel, I. T. A.; Guilherme, M. R.; Vidotti, G. J.; Rubira, A. F.; Muniz, E. C., Reaction of Glycidyl Methacrylate at the Hydroxyl and Carboxylic Groups of Poly(vinyl alcohol) and Poly(acrylic acid): Is This Reaction Mechanism Still Unclear? *J. Org. Chem.* **2009**, 74, 3750-3757.

26. Lally, S.; Bird, R.; Freemont, T. J.; Saunders, B. R., Microgels containing methacrylic acid: effects of composition on pH-triggered swelling and gelation behaviours. *Colloid. Polym. Sci.* **2009**, 287, 335-343.

27. Huang, Y.; Liang, J.; Chen, Y., An Overview of the Applications of Graphene-Based Materials in Supercapacitors. *Small* **2012**, 8, 1805-1834.

28. Xu, C.; Wang, X., Fabrication of flexible metal-nanoparticle films using graphene oxide sheets as substrates. *Small* **2009**, 5, 2212-7.

29. Wang, X.; Bai, H.; Shi, G., Size Fractionation of Graphene Oxide Sheets by pH-Assisted Selective Sedimentation. *J. Amer. Chem. Soc.* **2011**, 133, 6338-6342.

30. Zhu, Y.; Murali, S.; Cai, W.; Li, X.; Suk, J. W.; Potts, J. R.; Ruoff, R. S., Graphene and Graphene Oxide: Synthesis, Properties, and Applications. *Adv. Mater.* **2010**, 22, 3906-3924.

31. Vasu, K. S.; Krishnaswamy, R.; Sampath, S.; Sood, A. K., Yield stress, thixotropy and shear banding in a dilute aqueous suspension of few layer graphene oxide platelets. *Soft Matter* **2013**, 9, 5874.

32. Ma, X.; Li, Y.; Wang, W.; Ji, Q.; Xia, Y., Temperature-sensitive poly(N-isopropylacrylamide)/graphene oxide nanocomposite hydrogels by in situ polymerization with improved swelling capability and mechanical behavior. *Eur. Polym. J.* **2013**, 49, 389-396.

33. Sahu, A.; Choi, W. I.; Tae, G., A stimuli-sensitive injectable graphene oxide composite hydrogel. *Chem. Comm.* **2012**, 48, 5820-2.

34. Fan, J.; Shi, Z.; Lian, M.; Li, H.; Yin, J., Mechanically strong graphene oxide/sodium alginate/polyacrylamide nanocomposite hydrogel with improved dye adsorption capacity. *J. Mater. Chem. A* **2013**, 1, 7433.

35. Kavitha, T.; Kang, I.-K.; Park, S.-Y., Poly(acrylic acid)-Grafted Graphene Oxide as an Intracellular Protein Carrier. *Langmuir* **2013**, 30, 402-409.

36. Kjøniksen, A.-L.; Nyström, B., Effects of Polymer Concentration and Cross-Linking Density on Rheology of Chemically Cross-Linked Poly(vinyl alcohol) near the

Gelation Threshold. *Macromolecules* **1996**, 29, 5215-5222.

37. Lairez, D.; Adam, M.; Emery, J. R.; Durand, D., Rheological behavior of an epoxy/amine system near the gel point. *Macromolecules* **1992**, 25, 286-289.

38. Madbouly, S. A.; Otaigbe, J. U., Rheokinetics of Thermal-Induced Gelation of Waterborne Polyurethane Dispersions. *Macromolecules* **2005**, 38, 10178-10184.

39. Sollich, P.; Lequeux, F.; Hébraud, P.; Cates, M. E., Rheology of Soft Glassy Materials. *Phys. Rev. Lett.* **1997**, 78, 2020-2023.

40. Winter, H. H.; Mours, M., Rheology of Polymers Near Liquid-Solid Transitions. In *Neutron Spin Echo Spectroscopy Viscoelasticity Rheology*, Springer Berlin Heidelberg: Berlin, Heidelberg, 1997; pp 165-234.

41. Goodwin, J. W.; Hughes, R. W., Rheology for Chemists An Introduction. The Royal Society of Chemistry: 2000.

42. Dreyer, D. R.; Park, S.; Bielawski, C. W.; Ruoff, R. S., The chemistry of graphene oxide. *Chem. Soc. Rev.* **2010**, 39, 228-40.

43. Godfrin, M. P.; Guo, F.; Chakraborty, I.; Heeder, N.; Shukla, A.; Bose, A.; Hurt, R. H.; Tripathi, A., Shear-directed assembly of graphene oxide in aqueous dispersions into ordered arrays. *Langmuir* **2013**, 29, 13162-7.

44. Chougnnet, A.; Audibert, A.; Moan, M., Linear and non-linear rheological behaviour of cement and silica suspensions. Effect of polymer addition. *Rheol. Acta* **2007**, 46, 793-802.

## **Chapter 4: Microgel / multi-walled carbon nanotubes composites**

### **4.1 Abstract**

In this chapter, new types of composites were constructed using vinyl-functionalised pH-responsive MG particles and multi-walled carbon nanotubes (CNTs) and studied. The mixed MG/CNT dispersion has the same ability to form injectable and mouldable physical gels as MG/GO. However, the DX MG/CNT gels are different to DX MG/GO because they are electrically conductive gels. Moreover, the MGs played the dual roles of a dispersant for the CNTs and a macro-crosslinker for the composite. TEM and SEM showed the evidence of attraction between the MG particles and the CNTs, which is believed to form after ultrasonication to stabilise the CNT dispersion. Both the ductility and the stiffness of the composites increased with increasing CNT concentration which was examined by dynamic rheology and static axial compression measurements. The conductive percolation threshold was found to be 0.015 wt.%. Cytotoxicity tests were also performed for DX MG/CNT which indicated that the composites had low cytotoxicity. These conductive composites may have future applications as injectable gels for soft-tissue repairing with biomechanical monitoring, myocardial patches or electronic skin.



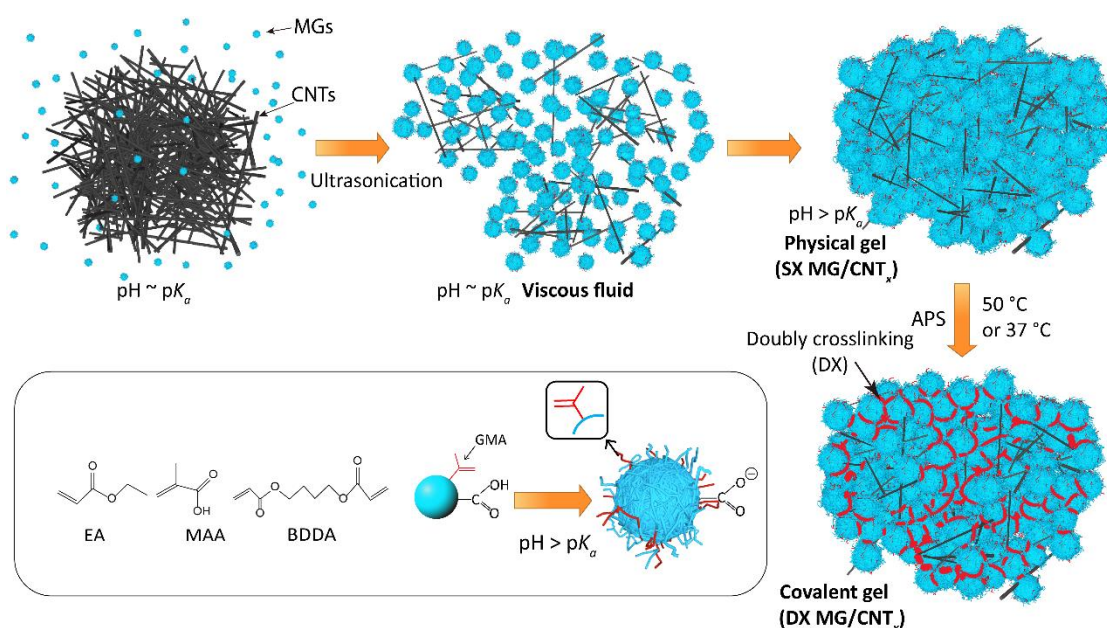
## 4.2 Introduction

In Chapter 3, the study of MG/GO composites showed the possibility to gain mechanically enhanced SX MG/GO and DX MG/GO gels. The mechanical properties of DX MG gels can be tuned by adding carbon reinforcements. In the present study we expand the work using another type of reinforcement to introduce new properties to DX gels such as electrical conductivity. Hence, in this study multi-wall carbon nanotubes (CNTs) was used in place of GO. The MG/CNT composite study should not only benefit in understanding the interactions of fillers and MGs in MG composite system but also increase the conductivity of the gel. The conductive injectable gel system might be a potential biomaterial for IVD repair or electronic skin.<sup>1-2</sup>

Similar to graphene, CNTs are famous for the high aspect ratio nanostructure,<sup>3</sup> low density,<sup>4</sup> mechanical and electrical properties which have made them be widely applied in nanocomposites<sup>5</sup>. Hydrogel composites containing a low content of CNTs are ideal for biosensors<sup>6</sup>, drug delivery<sup>7</sup> and tissue engineering<sup>8-9</sup> applications. However, CNTs tend to form aggregates in water due to their very large attractive forces (van der Waals interaction),<sup>10</sup> this significantly increases the difficulties in dispersing CNTs and preparing hydrogel composites. The high hydrophobicity of CNTs requires the use of surfactants, linear polymers or bespoke polymers for dispersing in aqueous.<sup>11-13</sup> However, the total content of CNT in hydrogel composites is usually relative low. In this study we used MG particles and the swollen MGs could be used to stabilise dispersions of CNTs and enable further preparation of DX MG/CNT gel composites.

The MG system investigated here is the same as that studied in Chapter 3. The

structure of MG particles and the formation of the gel composites involved using concentrated MG dispersions (and pH-triggered particle swelling) are depicted in Scheme 4.1. The MG particles were in their collapsed (latex) form at low pH ( $\text{pH} < \text{p}K_a$ ). The viscosity of concentrated MG dispersions increased and they formed viscous fluids when the pH approached their  $\text{p}K_a$ . The state of viscous fluid was defined separately because this dispersion is able to disperse CNTs during ultrasonication. If the pH is too low, the MG particles tend to form aggregates which caused by ultrasonication. A fluid-to-gel transformation occurred when the pH increased to above the  $\text{p}K_a$  that produced a SX MG/CNT physical gel. The vinyl groups of the swollen MG particles then came into close contact enabling conversion of the physical gels into DX MG/CNT gels.



**Scheme 4.1. Dispersion of CNTs using MGs and DX MG/CNT formation.** The CNTs were dispersed in a viscous fluid of partially swollen MG particles. The pH was increased to trigger further MG swelling, and formed a physical gel (SX MG/CNT). In the presence of APS, covalent interlinking (shown in red) occurred and the DX MG/CNT gel composite formed after heating for 8 hours.  $x$  is the concentration of CNTs used in composites.

The aim of this chapter is to understand the construction of MG/CNT composites and investigate the role of MG particles in dispersing CNT. The characterisation of the MG and CNT building blocks used for gel composite construction are studied first.

Subsequently, the interaction between the MGs and CNTs are examined, and the morphology, mechanical, electrical and pH-responsive properties of the DX MG/CNT gel composites are studied. We show that both the modulus and ductility increased with the increasing CNT concentration and a mechanism for this unusual behaviour is proposed. The electrical conductivity data showed a very low percolation threshold for CNT within the DX MG/CNT composites.

## 4.3 Experimental

### 4.3.1 Materials

CNTs (multi-walled, outer-diameter  $\times$  length 6 - 13 nm  $\times$  2.5 - 20  $\mu$ m), EA (99%), MA (99%), MAA (99%), BDDA, (90%), GMA (97%), NaOH (97%), APS (98%), SDS ( $\geq$  92.5%), K<sub>2</sub>HPO<sub>4</sub> (97%), PBS (phosphate buffered saline, pH = 7.4 bioreagent),  $\alpha$ -MEM medium (minimum essential medium eagle,  $\alpha$  modification), FBS (foetal bovine serum) and L-ascorbic acid-2 phosphate were all purchased from Sigma-Aldrich and used as received. All water was distilled and deionised.

### 4.3.2 Preparation of MG dispersion

The synthesis of poly(EA/MAA/BDDA) MG used the seed-feed emulsion polymerisation method. Briefly, a mixed monomer solution (250 g) of EA (62.9 mol.%), MAA (36.6 mol.%), BDDA (0.5 mol.%) was prepared. Seed formation was conducted using a portion of the monomer mixture (31.5 g) after addition of water (517.5 g) containing the SDS (1.8 g), K<sub>2</sub>HPO<sub>4</sub> (3.15 g of 7 wt.% solution) and APS (10 g of 2 wt.% solution). The seed was formed at 80 °C with mechanical stirring in a nitrogen atmosphere. The remaining monomer solution was added uniformly with a rate of 2.4 g/min. After feed completion the temperature was maintained for a further 2 h. The product was extensively dialysed against water for 3 weeks. The method for functionalisation was the same as given in Chapter 3, Section 3.3.3, which is, heating the mixture of 100 g MG (10 wt.%) dispersion with 16.6 g GMA (0.12 mol.) for 8 h and following by extensive dialysis.

#### **4.3.3 Preparation of SX/CNT<sub>x</sub> dispersions**

The MG content for all gels used in this study was 10 wt.% unless otherwise stated. To prepare SX MG/CNT<sub>x</sub> mixed dispersions as viscous fluids ( $x$  is the wt.% of CNTs) the pH of a concentrated mixed dispersion containing 10 wt.% MG was adjusted to 6.8 using NaOH solution (0.5 M) and then the appropriate mass of CNTs added. Mechanical stirring (700 rpm) was used until a mixed dispersion was formed. The mixture was then placed into an ice bath and an ultrasonic probe was used (ultrasonic processor, 750 W) for 60 min and combined with mechanical stirring. Ultrasonication used sequential power step cycles of “on” (30 s) and “off” (30 s). The total sonication time was 30 min and the energy used was ~ 96 kJ.

#### **4.3.4 Preparation of DX MG/CNT<sub>x</sub> composite gels**

The DX MG/CNT gel composites were prepared at 37 or 50 °C. The following example describes the preparation of DX MG/CNT<sub>1.0</sub>. The latter was prepared by adding NaOH (4 M, 40 µl) and also APS solution (3.4 wt %, 230 µl) to the mixed MG/CNT<sub>1.0</sub> viscous dispersion (6 g) described above. The final pH was adjusted to 7.4. The crosslinking process was initiated by heating at 50 °C for 8 h within sealed molds. Identical methods were used for the preparation of the other DX MG/CNT<sub>x</sub> gel composites. DX MG/CNT gel composites were also prepared at physiological temperature (37 °C). In these cases, APS solution (3.4 wt %, 230 µl) and TEMED (0.08 M, 200 µl) were added to the parent viscous mixed dispersions. The crosslinking process was initiated by heating at 37°C for 20 min.

#### 4.3.5 Physical Measurements

Potentiometric titration measurements were performed using a Mettler Toledo DL 15 titrator in the presence of a supporting electrolyte (0.1 M NaCl). Photon correlation spectroscopy (PCS) measurements were performed using a BI-9000 Brookhaven light scattering apparatus equipped with a 20 mW HeNe laser and the detector was set at a scattering angle of  $90^\circ$ . SEM images were obtained using a Philips FEGSEM instrument. Samples were dried at room temperature (MG particles) or by freeze-drying (gels). TEM measurements were obtained using a JEOL JEM-2011F operating at an accelerating voltage of 200 kV and the samples were supported by 200 mesh carbon supported film on copper TEM grids. TGA measurements were performed in  $N_2$  atmosphere using a TA Instrument Q500 with a heating rate of  $10^\circ\text{C} / \text{min}$ . The electrical conductivity measurements were performed on the gel composite samples in the hydrated state using a Jandel multi-height four-point probe station with cylindrical tungsten carbide four probe head (spacing 1.0 mm between each probe head). The measurement results were recorded by Keithley 2440 multimeter. The samples were prepared inside the O-rings with a constant diameter of 20.8 mm and thickness of 2.4 mm.

The swelling tests for the DX microgels were performed by placing the samples in the buffer solutions for 7 days. The buffers were refreshed every day. To measure the weight and the volume change, a sample was removed from buffer solution, the excess solution from the surface carefully removed using an absorbent tissue and the sample weighed and then returned to the buffer solution. The volume swelling ratio

of the gel composites ( $Q_v$ ) was calculated from the difference of the sample weight before and after swelling by using the following equation:

$$Q_v = \frac{\rho_{mix}(Q_m - 1)}{\rho_s} + 1 \quad (4.1)$$

Where  $Q_m$  is the weight swelling ratio,  $\rho_s$  is the density of water, and the  $\rho_{mix}$  were calculated by polymer ( $\rho_{gel} = 1.2 \text{ g}\cdot\text{cm}^{-3}$ ) and CNT ( $\rho_{CNT} = 2.1 \text{ g}\cdot\text{cm}^{-3}$ ) densities as below:

$$\rho_{mix} = \rho_{gel}x_{gel} + \rho_{CNT}x_{CNT} \quad (4.2)$$

Where  $x_{gel}$  and  $x_{CNT}$  are the weight fractions.

Dynamic rheology measurements were conducted using a TA Instruments AR-G2 temperature-controlled rheometer equipped with an environmental chamber. A parallel plate geometry (20 mm) was used. For the frequency-sweep data a strain of 1% was used; whilst for the strain-sweep data a frequency of 1 Hz was used. The compression tests were conducted using an Instron series 5569 load frame equipped with a 100 N compression testing head. Nominal stress and strain values are reported.

#### 4.3.6 Cytotoxicity studies

The cytotoxicity measurements were performed by Dr. Mi Zhou (Faculty of Medical and Human science, Univerisity of Manchester): Adipose derived human mesenchymal stem cells (MSCs) were grown in  $\alpha$ -MEM medium supplemented with 10 % v/v FBS, *L*-ascorbic acid-2 phosphate (10  $\mu$ M), 1x Glutamax (Life Invitrogen, UK) and an antibiotic mixture of penicillin (100 units/ml), streptomycin (100  $\mu$ g/ml) and amphotericin (0.25  $\mu$ g/ml) were used for cytotoxicity studies of the gel composites. Cells were regularly passaged at 80% confluence and cells at passage 3 were used in the cytotoxicity assessments. The gel composites were fabricated into

round disc-like shape with a diameter of 12 mm. Prior to assessments, the hydrogels were pre-soaked in PBS for 24 h. MSCs were trypsinized and cultured in a density of 20,000 cells/cm<sup>2</sup> into 6-well plates. The cells were allowed to adhere to the bottom of the well for 24 h before exposure to the hydrogels. The hydrogels in tissue culture inserts were then introduced into the wells and were maintained for a further 7 days. Cell viability and proliferation was measured respectively at 1, 4, and 7 days post hydrogel introduction. At each time point, samples were incubated in a Live / Dead solution containing calcein AM and ethidium homodimer-1 (Life Invitrogen, UK), and the cells were imaged using an Olympus BX51 fluorescence microscope fixed with a Qimaging Retiga-SRV camera. Other samples were incubated at the same time in normal medium containing Alamar Blue solution (Life Invitrogen, UK) for 2 h and fluorescence changes of the medium supernatant were measured at a 560 nm EX (excitation) / 590 nm EM (emission) setting using a BioTek FLx800 fluorescence plate reader combined with a Gen5 data analysis software.



## 4.4 Results and discussion

### 4.4.1 Microgel characterisation

The hydrodynamic size and pH- responsive swelling behaviours of the SX MG particles were examined by DLS measurements. The content of MAA groups and GMA groups contained in the MG particles were determined by potentiometric titration data. The morphology of the MG particles was observed from SEM images. These aspects are discussed below.

#### 4.4.1.1 Potentiometric titration

Titration data (Fig. 4.1) gave the apparent  $pK_a$  values for SX MG particles of 6.3 and 38.2 mol.% of MAA content. As shown in Table 4.1, the mol.% of GMA functionalisation groups was 8.0 %. The values were calculated by the difference of MAA groups before and after the GMA functionalisation.

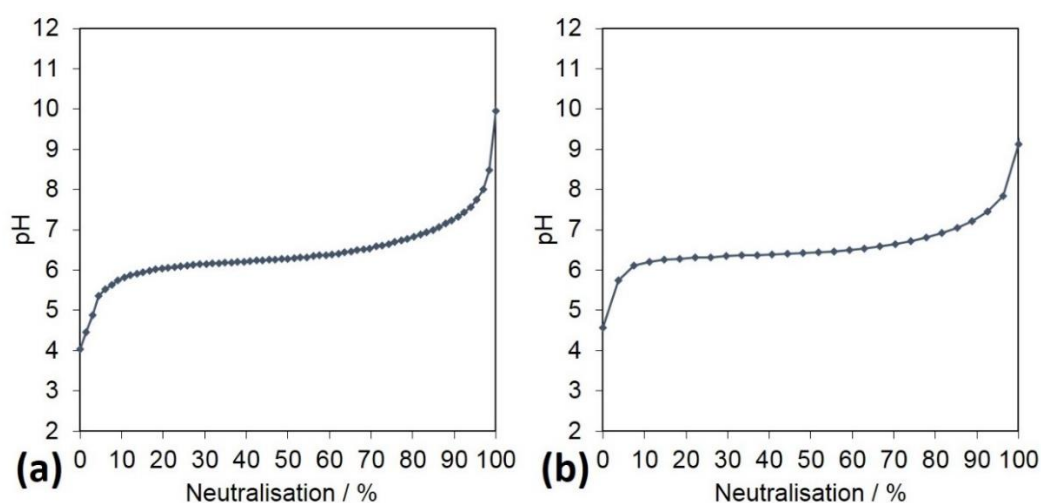


**Fig. 4.1.** Potentiometric titration data for SX MG before (a) and after (b) the GMA functionalisation.

**Table 4.1.** Characterisation data for the MG.

Abbreviation	Mol.% MAA <sup>a</sup>	Mol.% GMA <sup>a</sup>	$d_{n(SEM)}$ <sup>b</sup> / nm	$d_{h(4)}$ <sup>c</sup> / nm	$d_{h(10)}$ <sup>c</sup> / nm	$Q_{(10)}$	$pK_a$
SX MG	38.2	8.0	74 (12)	77	278	47	6.3

<sup>a</sup> Calculated from potentiometric titration data. <sup>b</sup> Number-average diameters determined from SEM. The number in brackets is the coefficient of variation. <sup>c</sup> The hydrodynamic diameters ( $d_h$ ) at pH 4.0 and 10.0.

#### 4.4.1.2 DLS measurements

The swelling behaviour of SX MG was examined using DLS data. The SX particles were pH-responsive (Fig. 4.2) with a hydrodynamic diameter ( $d_h$ ) of 77 nm at pH = 4. The latter size was defined as collapsed size. This size is much smaller than what we found in Chapter 3 (125 nm). The smaller size is due to the smaller amount of initiator introduced during polymerisation of the present MG particles. With increasing pH the MG-GMA particles exhibited pH-dependent swelling with a maximum  $d_h$  of 278 nm at pH = 10 ( $d_{h(10)}$ ). The maximum volume swelling ratio,  $Q_v$  ( $= (d_{h(10)}/d_{h(4.0)})^3$ ) is 47. In the following works, most of the gels were prepared at pH = 7.4 which is a common target pH for biomaterial applications.

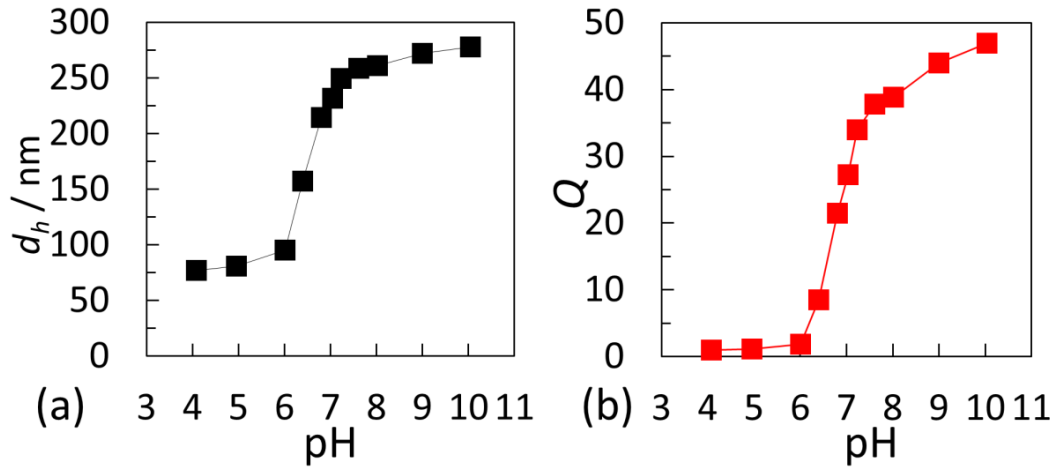


**Fig. 4.2.** (a) Hydrodynamic diameters and (b) particle volume-swelling ratios ( $Q$ ) of SX MG particles over a range of pH values.

#### 4.4.1.3 Scanning Electron Microscopy

The spherical MG particles were observed by SEM (see Fig 4.3). The number-average diameter ( $d_{SEM}$ ) of SX MG particles is about 74.0 nm (coefficient of variation = 12%). The values for  $d_{SEM}$  are slightly larger than the collapsed size of the particles determined by DLS. Considering the value for  $d_{SEM}$  is close to the value for  $d_{h(4.0)}$ , we estimate that the  $d_{h(4.0)}$  are the size of collapsed particles in the dispersion.

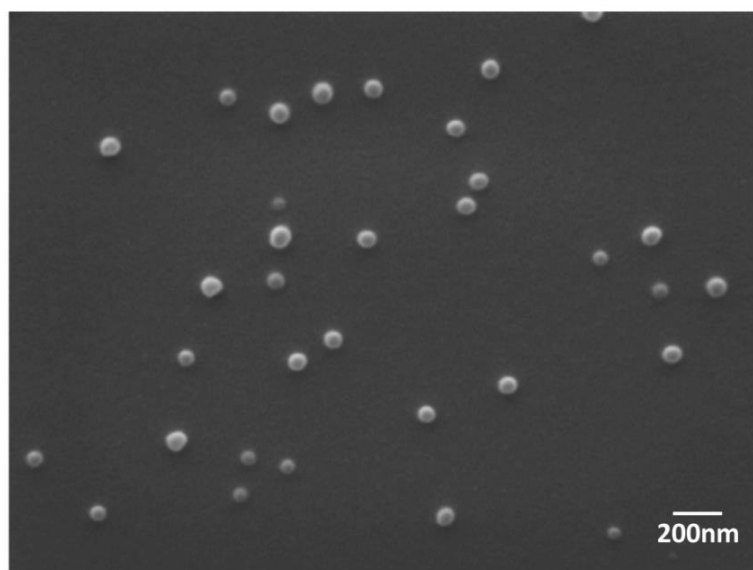


**Fig. 4.3.** SEM images of SX MG particles.

#### **4.4.2 Characterisation of CNT**

The details of the CNT were given by the supplier. The outer diameter of the tubes was in the range of 6 to 13 nm, and the length was between 2.5 to 20  $\mu\text{m}$ . The CNTs are a hydrophobic material and tends to be entangled or aggregated in the dispersion.<sup>14</sup> Therefore, in this study ultrasonication was used to separate the CNTs and disperse them in the water media. However, it is noted that the length of CNTs may become shorter due to ultrasonication.<sup>15-16</sup> The structures of both as-applied CNTs and the ultrasonicated CNT were examined by SEM and Raman spectroscopy.

##### **4.4.2.1 Scanning Electron Microscopy**

The quality of as-supplied CNTs was observed by SEM and the images are shown in Fig 4.4 (a) and (b). Fig 4.4a showed the edge of an aggregate form CNT powder, which the CNTs are highly entangled. By contrast, 0.5 wt.% of CNT was added into water and ultrasonicated for 10 minutes and an image is shown in Fig 4.4c. It can be seen that the large aggregates of CNT were separated into individual and small bundles (Fig 4.4d). Also, the length of CNT became shorter than the as-supplied CNTs. This behaviour is similar to that reported for CNTs under ultrasonication<sup>16</sup>.

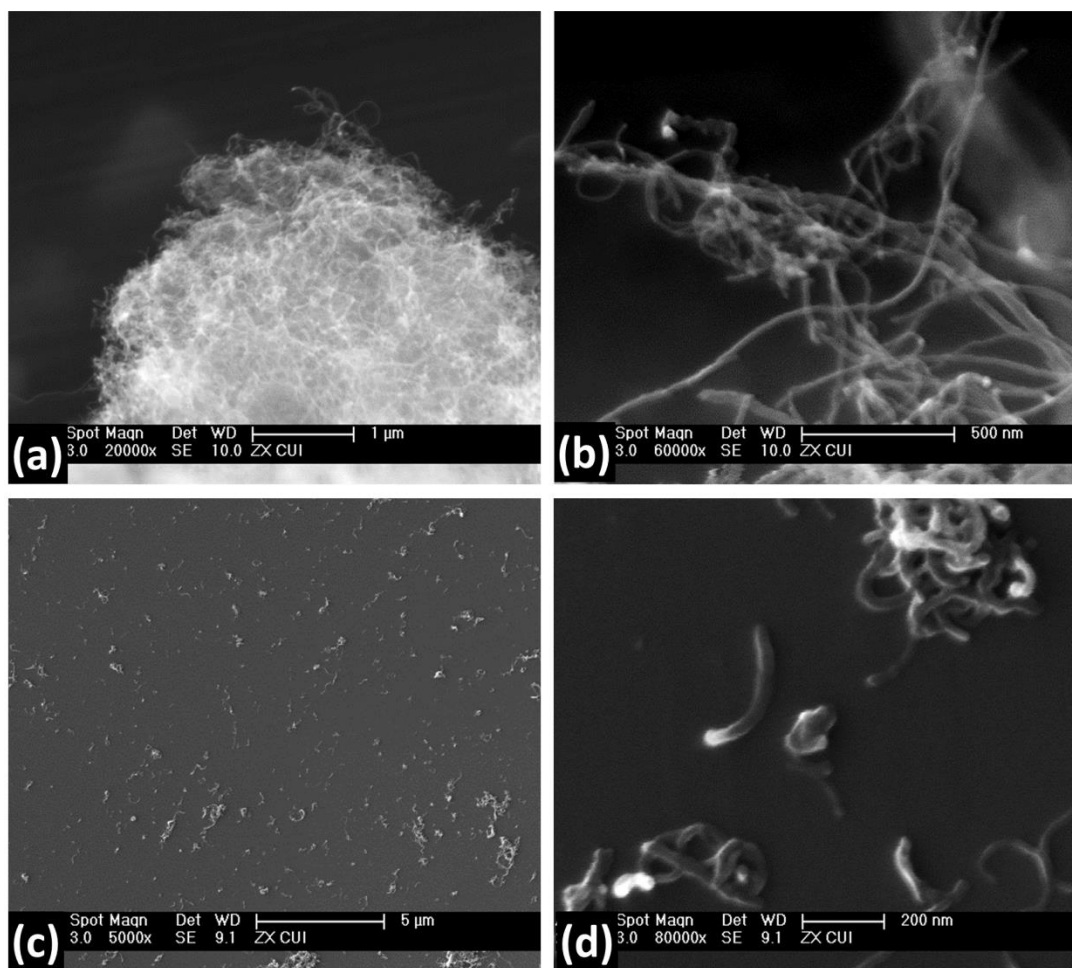


**Fig. 4.4.** SEM images of as-supplied (a) and (b), Images after dispersing CNTs using ultrasonication (c) and (d).

#### 4.4.2.2 Raman spectroscopy

The dispersing process for the CNTs was also characterised by Raman spectroscopy as shown in Fig 4.5. Fig. 4.5a presents the spectrum of as-supplied CNTs. The D band located at around  $1350\text{ cm}^{-1}$  and the G band located at around  $1600\text{ cm}^{-1}$ . Both spectra (before and after dispersing) showed a typical characterisation of CNTs (Multi-walled),<sup>17</sup> which is the prominent D band, the latter is from the disordered carbons in multi-layers of graphene structures and the defects on the walls. In contrast, the SWNTs normally have a lower prominent D band, and the graphite does not show this band. The Raman spectrum for CNTs after ultrasonication showed very similar intensities of the D and G bands which indicate that ultrasonication did not

induce more defects on the walls of the CNTs (Fig 4.5b).

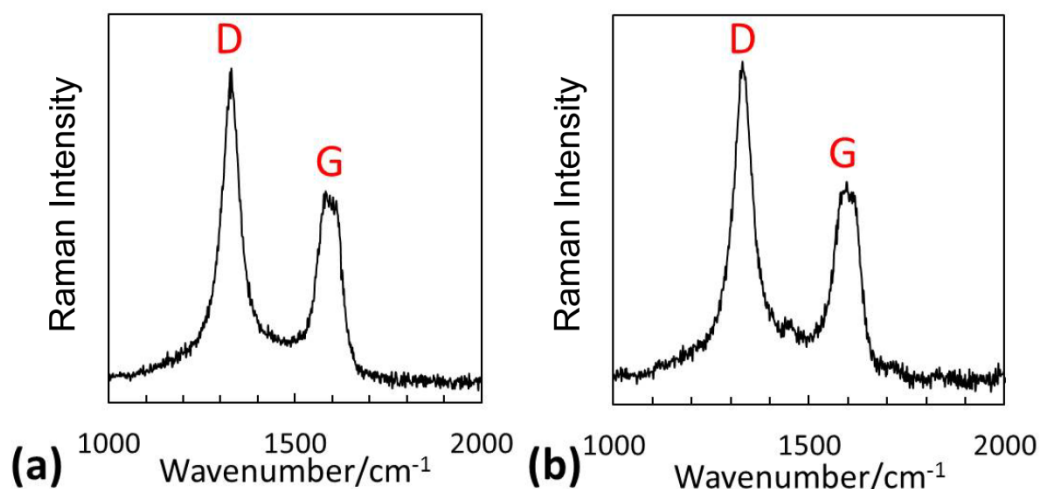


**Fig. 4.5.** Raman spectra of (a) as-supplied CNTs and (b) the CNTs after ultrasonication in water.

#### 4.4.3 Characterisation of MG/CNT dispersions

Dispersing CNTs using MGs was a crucial step in this study since a relatively high concentration of CNTs ( $> 0.05$  wt.%) tend to precipitate in water rapidly.<sup>18</sup> Here, we dispersed the CNTs in viscous MG dispersions ( $\text{pH} = 6.8$ ) by performing ultrasonication. After ultrasonication, the MG/CNT dispersion could form a physical gel rapidly, so the swollen particles opposed the movement of CNTs which were trapped in the dispersed state and the formation of large CNT aggregates was avoided. Also, there were hydrophobic groups on the MG particles (e.g. ethyl groups in EA) which may have interacted with the hydrophobic surfaces to increase the stability of the CNT dispersion. Finally, the high content of  $-\text{COOH}$  groups on the surface of the MG particles assist dispersing the CNTs.<sup>19</sup> Here, we need to note that the MG dispersion become not stable with ultrasonication when the pH was lower than 6.8. Then, the MG particles could swell to form a viscous solution which also could stabilise the dispersion of CNTs. This viscous CNT/MG mixture dispersion was characterised by optical microscopy and TEM images.

#### 4.4.3.1 Optical microscopy

The MG/CNT<sub>1.0</sub> viscous dispersion (pH = 6.8) was investigated by an optical microscopy as shown in Fig 4.6a. By contrast, water and SDS (2.5 wt.%) solutions were used to disperse the same concentration of CNTs as shown in Fig 4.6 (b) and (c), respectively. For dispersing the CNTs, the MG particles were more effective than either water or SDS solutions. In water, the CNTs could form large aggregates and the CNT could not be dispersed in water at this concentration (1 wt.%). For SDS solutions, obvious aggregates were observed, but the average size was smaller than for water. For MG/CNT dispersions, no large aggregates can be found in Fig 4.6a. However, some small spherical aggregates were still present, which were most likely small CNT bundles.

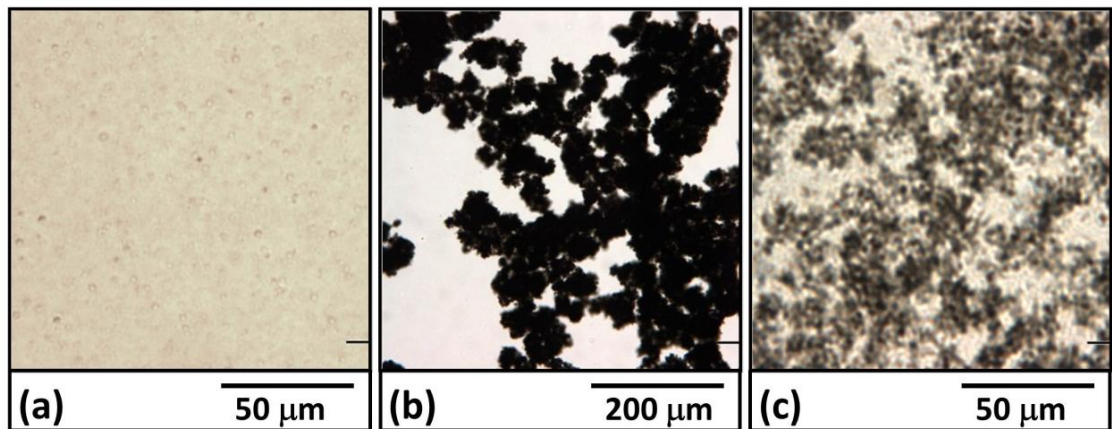


**Fig. 4.6.** Optical micrographs of CNT (1 wt.%) dispersed in (a) MG solution (10 wt.%, pH = 6.8) as a viscous fluid, (b) water and (c) in aqueous SDS (2.5 wt.%) solution. All images were taken within 5 minutes after ultrasonication.

The CNT bundles are also clearly revealed from the image for the SX MG/CNT<sub>1.0</sub> gel (Fig 4.7a) since the MG particles are transparent in this state. Considering the MG particles were swollen and occupied most of the space, we believe that the CNTs did not form large aggregates within the composites gel but tended to form small and uniformly distributed CNT bundles. Therefore, the MG-assisted dispersion/trapping method enabled CNTs to be dispersed at  $C_{CNT}$  values up to 1 wt.%. The latter value is

relatively high compared with the  $C_{CNT}$  values reported for CNTs dispersed by conventional surfactants.<sup>20-21</sup> The dispersed nature of SX MG/CNT<sub>1.0</sub> dispersion is shown in Fig. 4.7b and the gels were formed when increasing the pH to 7.2. In the gel state the composites were not only injectable (Fig. 4.7c) but also moldable as shown in Fig. 4.7d when the gel could maintain a cylinder shape on a rod.

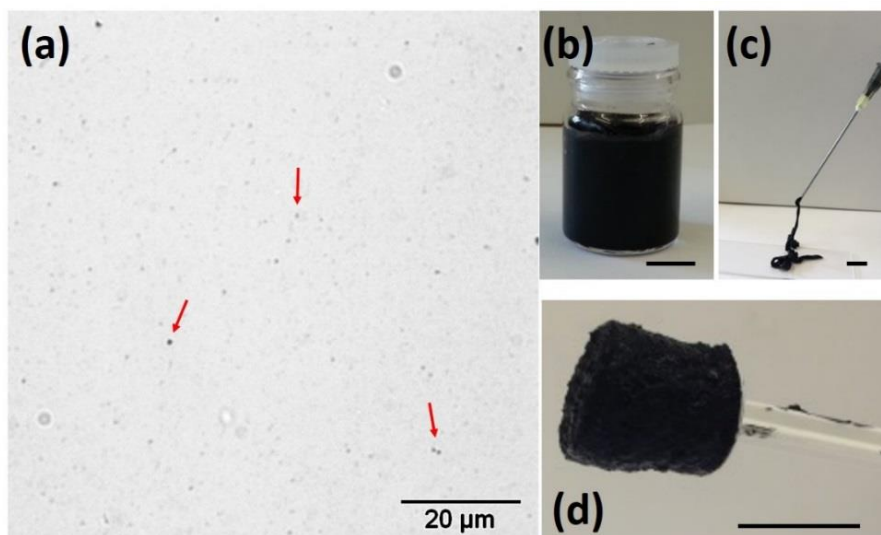


**Fig. 4.7.** (a) Optical micrograph of SX MG/CNT<sub>1.0</sub> gel and the photographs of SX MG/CNT<sub>1.0</sub> dispersion (b) and gel ((c) and (d)). The scale bars in (b)-(d) represent 10 mm. The red arrows in (a) showed the CNT bundles.

One important question concerns whether the MG particles and CNTs have interactions in the composites. It was mentioned that the MG particles aggregated at low pH during ultrasonication. Interestingly, when the MG/CNT dispersion (pH ~ 4.3) was ultrasonicated, the MG particles and CNTs formed macroscopic aggregates together (Fig. 4.8a), and the remaining solution was slightly turbid. By contrast, a CNT dispersion with the same concentration in water is shown in Fig. 4.8b, and many sediments were observed. Therefore, we propose there was an attractive interaction between CNTs and MG particles.

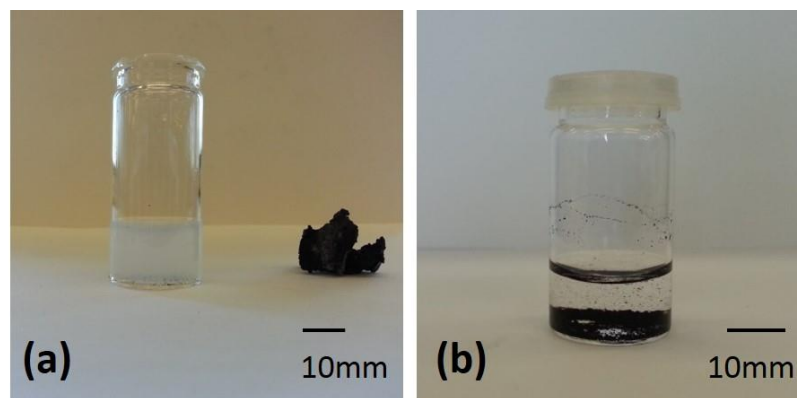


**Fig. 4.8.** (a) showed the MG and CNTs formed a macroscopic aggregate. (b) showed the sediments of CNTs in water. The CNT concentration in both cases was 0.5 wt.%

#### 4.4.3.2 TEM studies

The dispersions of MG/CNT<sub>1.0</sub> were also examined by TEM after sample deposition. Fig. 4.9a showed that the CNTs were clearly evident as separately and uniformly distributed state within a concentrated MG layer on the carbon film. There are some other observations to understand the complex morphology of CNTs within MGs matrix. Fig 4.9b shows an area with low concentration of MG particles where some CNTs are exposed. In this images, three observations are worth to indicate. Firstly, in Fig. 4.9b(i) one straight CNT passed through a looped CNT, this feature could explain the entangled CNT bundles which is because of some CNTs are significantly bent or even looped. Furthermore, several MG particles adhered directly to the wall of CNTs (Fig. 4.9b(ii)), which probed the interaction between CNT and MGs. If there is no interaction, the MG particles and CNTs should stay separately because of MG particles are much more hydrophilic than CTNs. Finally, Fig. 4.9b(iii) showed the MG particles bridged the adjacent CNTs which would be an important interaction for stress transfer within the composites.



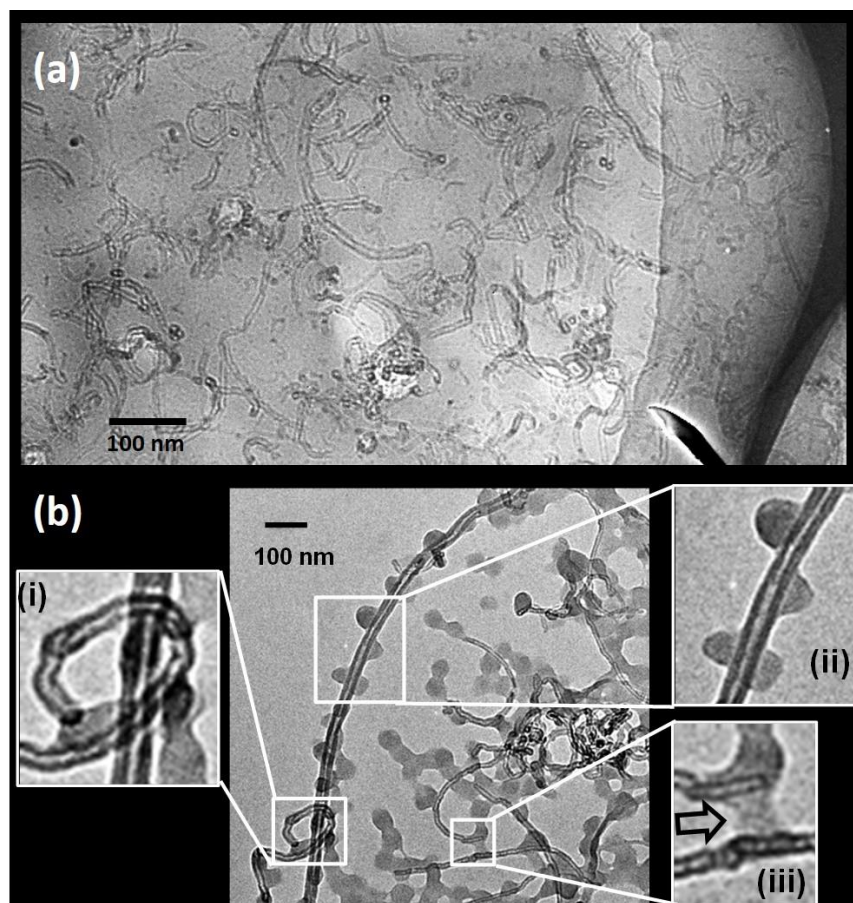


**Fig. 4.9.** TEM images showed (a) CNTs were distributed in a concentrated MG layer and (b) evidence of CNT-MG interaction. The insets of b showed (i) the entangled CNTs, (ii) the interaction between CNT and MG particles, (iii) MG particles bridging two CNTs.

#### 4.4.4 Characterisation of SX MG/CNT and DX MG/CNT gels

##### 4.4.4.1 Morphology of freeze-dried DX MG/CNT gel

The morphology of DX MG/CNT gels was examined by SEM (Fig. 4.10). The porous structure is a typical morphology for freeze-dried hydrogel as shown in Fig 4.10a. The evidence of discrete CNTs was clearly shown on the walls of composite gel, which indicate an excellent dispersibility of CNTs within the gel matrix. The higher magnification image (Fig. 4.10b) focused on the surface of the composite gel. The rod-like features are most likely CNTs, but the diameter of the rod is much higher than the as-supplied CNTs.

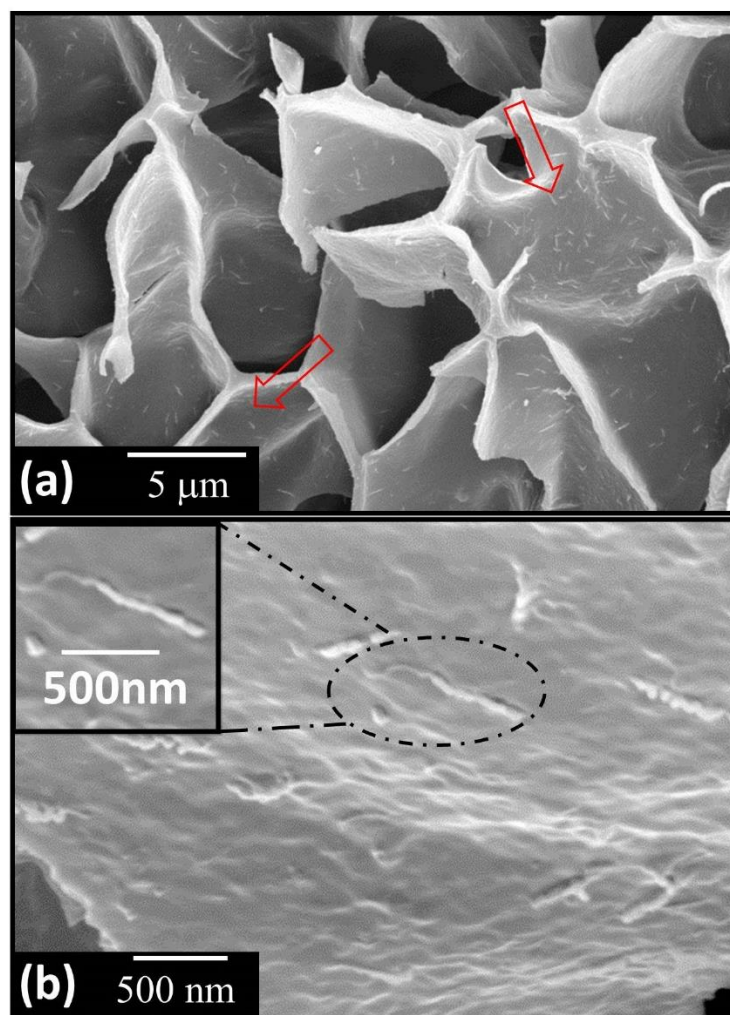


**Fig. 4.10.** SEM images of a freeze-dried DX MG1/CNT<sub>0.5</sub>. (a), (b) show low and high magnification images. The red arrows in (a) shows many CNTs can be observed on the surface of DX MGs. The inset in (b) shows CNT on the surface.

#### 4.4.4.2 Structure of CNT networks

CNTs are thermal stable materials at 900 °C in N<sub>2</sub> atmosphere.<sup>22</sup> Hence, this property can be used to explore the morphology of CNT percolated networks and the distribution of CNTs within the gel matrix. A freeze-dried composite gel sample was heated at 850 °C in N<sub>2</sub> for 1 hr. Under this condition, about 85% of the weight of freeze-dried composite gel was removed (Fig. 4.11) and the CNTs were exposed (Fig 4.12). The remaining matter revealed a nanoporous morphology with pore walls that were composed of the CNTs networks. The overall microscopic porous structure in Fig. 4.10 was very similar to what we observed in Fig 4.12, which indicates the

CNTs networks were able to keep the structure after removing the MGs. The higher magnification image (Fig 4.12b) showed that the CNTs were entangled and formed a 3D mesh structure. However, there was a large volume reduction in gel structure during the drying process due to the removal of water. This compressed the space for the CNTs networks. Considering the structure shown in Fig. 4.9a, we propose that the CNTs structure in the as-prepared composite gels consisted of dispersed individual CNTs and a network of entangled CNTs. Moreover, considering inter-linked MG particles were present, we also proposed that these gel composites contained interpenetrating networks of interlinked MGs and entangled CNTs.

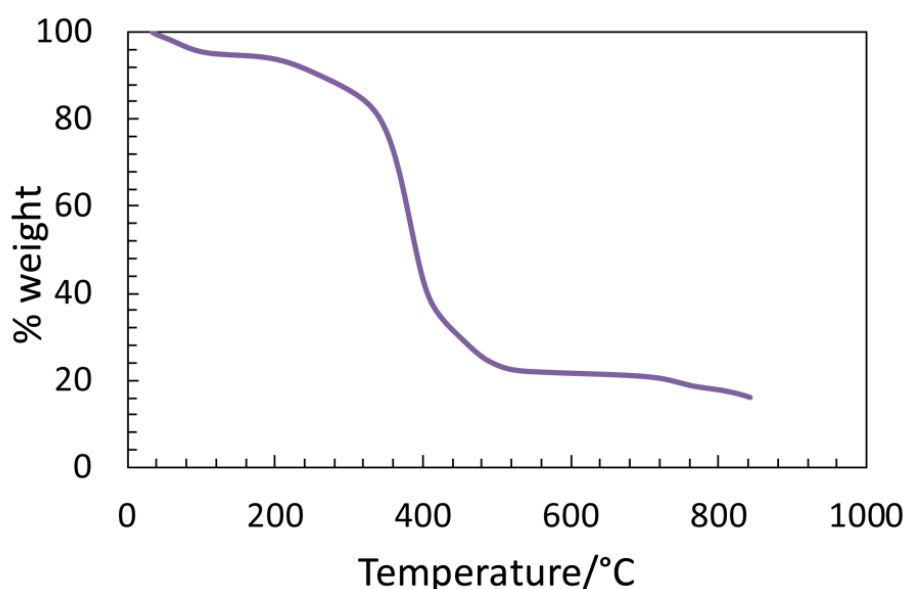


**Fig. 4.11.** TGA data for DX MG/CNT<sub>0.5</sub> when heated under a N<sub>2</sub> atmosphere.

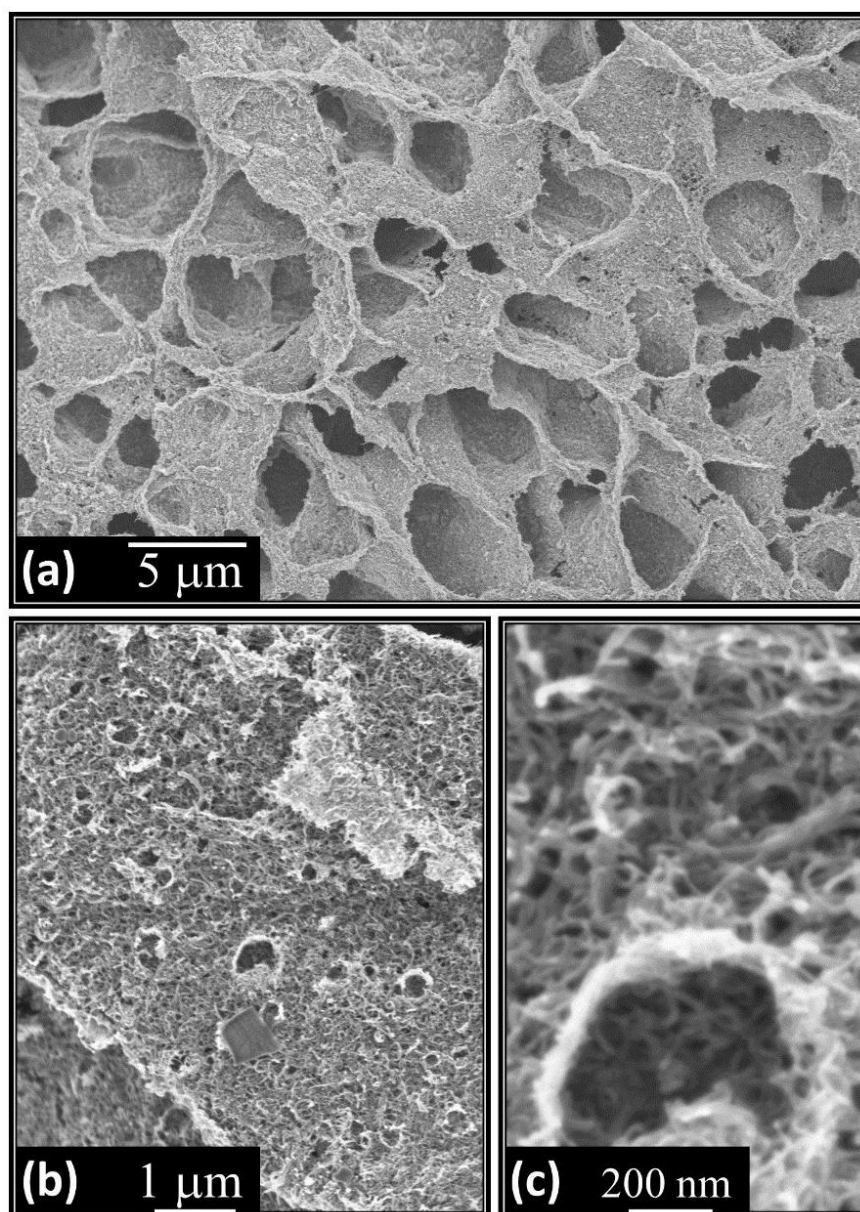


**Fig. 4.12.** SEM images of a DX MG1/CNT<sub>0.5</sub> gel after heating at 800 °C in N<sub>2</sub>.

#### 4.4.4.3 Morphology of fracture surface

The fracture surfaces of the freeze-dried gel composite sample were observed by SEM as shown in Fig 4.13. One crack was produced on the gel surface, and then the samples were rapidly immersed into liquid N<sub>2</sub> which followed with freeze-drying. The crack is shown in Fig. 4.13a and the close examination showed some protruding CNTs on the fracture surface (Fig 4.9b). The presence of “pulled out” CNTs at the fracture surface indicates some of the CNTs acted as bridges in the MG matrix instead of forming isolated agglomerates.



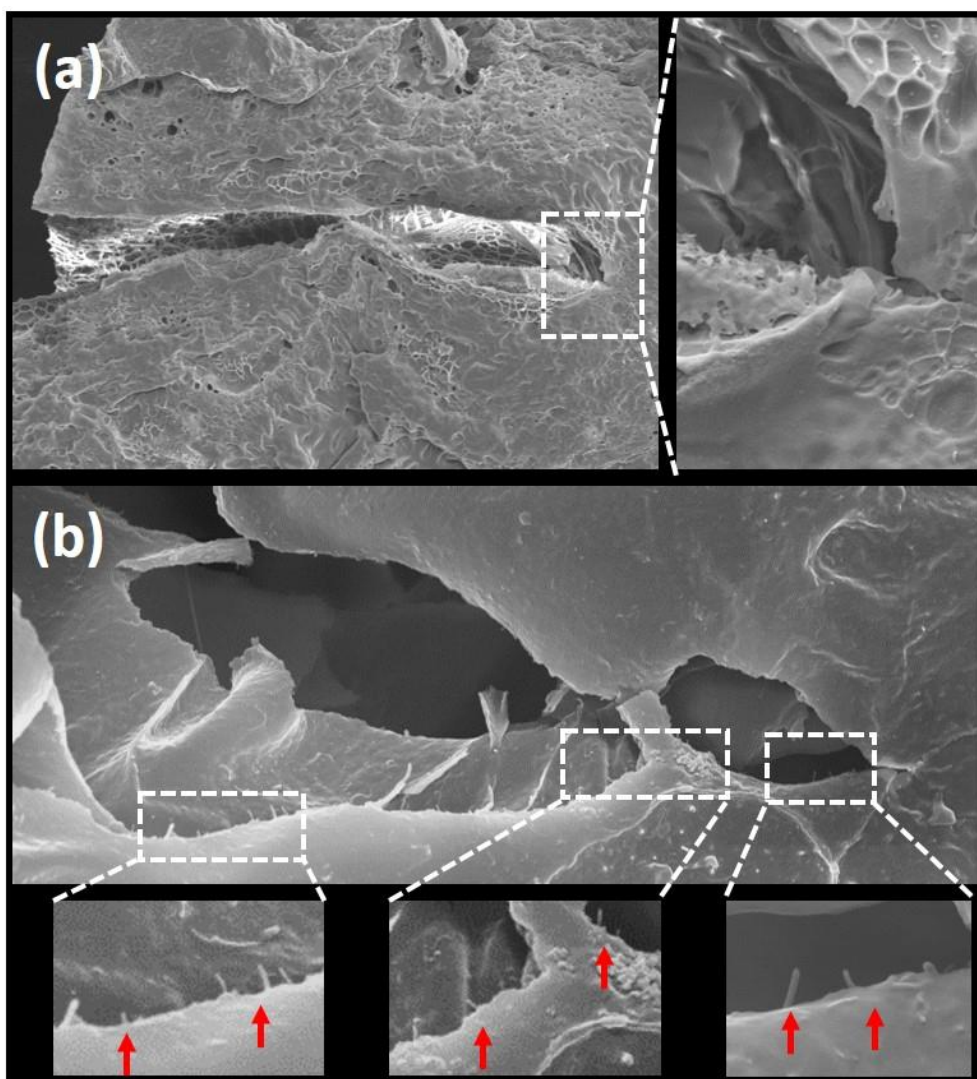


**Fig. 4.13.** A sample that was fractured and then freeze-dried and the SEM images show a fracture surface. (a) shows a crack on the gel surface. (b) shows the higher magnification images of the tail part of the crack. The inset in (a) showed the position of the tail part. The insets in b showed the pulled-out CNTs, which were also highlighted by red arrows.

#### 4.4.4.4 Swelling test

The swelling behaviours of DX MG/CNT gels is shown in Fig. 4.14. The as-made gels were prepared at a similar size (Fig. 4.14a) and placed into buffer solutions with various pH values of 4.0, 7.6 and 10.0. Fig. 4.14b showed that the gel was collapsed at pH 4 and swelled at pH 7.6 and 10.0. The gels were further placed in solution for 30 days, which indicated that neither the collapsed gel (Fig. 4.14c) or the swollen gel (Fig. 4.14 d) ruptured or generated sediments. By contrast, one sample of SX MG/CNT physical gel was placed into buffer solution (pH = 7.6) and the gel

redispersed after 30 minutes. These observations confirmed the existence of inter-linking between particles (for DX MG/CNT) which could retain the gel structure at both low and high pH environments for an extended period.

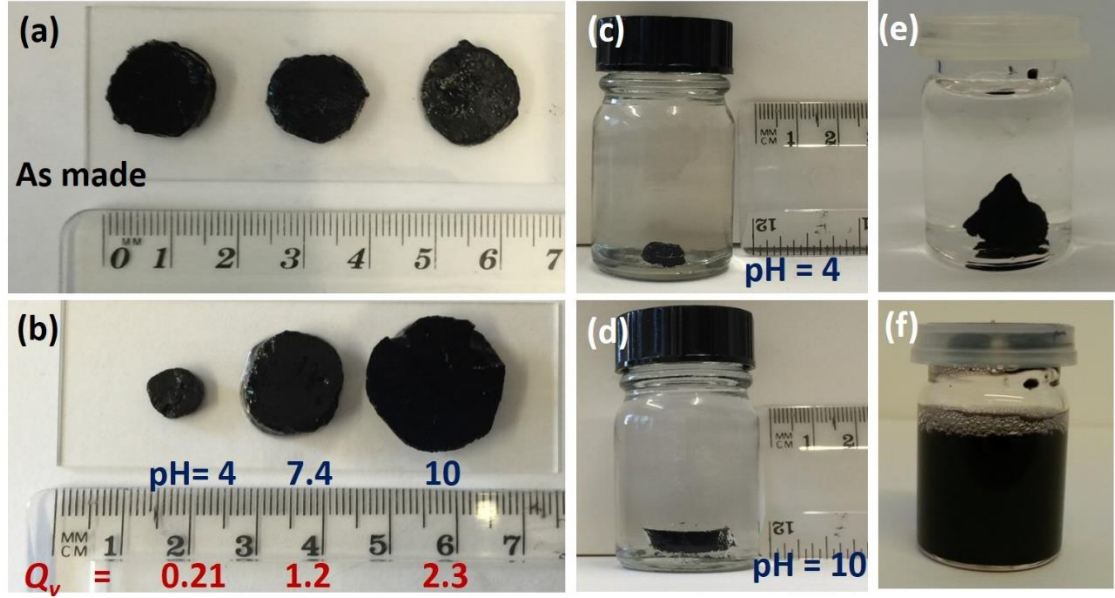


**Fig. 4.14.** Variable pH swelling behaviour for DX MG/CNT<sub>1.0</sub> gels. (a) showed the as-made DX MG/CNT<sub>1.0</sub> gels. (b) showed the size of samples after being placed in various buffer solutions for 7 days. Volume swelling ratios are also shown. (c) and (d) showed the sample in buffer solutions at pH 4 and 10, respectively, after 30 days. (e) showed a piece of SX MG/CNT<sub>1.0</sub> gel was placed into buffer solution and (f) showed the gels re-dispersed after 30 minutes.

#### 4.4.4.5 Electrical conductivity measurements for DX MG/CNT gels.

Electrical conductivity measurements were performed on the gel composites to study the conductivity of CNT networks and percolation threshold. The data from Fig. 4.15 showed that the DX MG/CNT<sub>1.0</sub> had the highest conductivity values ( $\sigma$ ) of 0.032 S/cm which is two orders of magnitude higher than the values for CNT-free gels. The conductivity of gels increased with the  $C_{CNT}$ , and this tendency was simulated by a percolation power law.<sup>23</sup>

$$\sigma = \sigma_o (C_{CNT} - C_{CNT(p)})^s \quad (4.3)$$

where  $\sigma_0$  is a factor relate to the conductivity of CNT,  $C_{CNT(p)}$  is the concentration of CNTs at the percolation threshold, and  $s$  is the power law component associated with the dimensionality of the network.

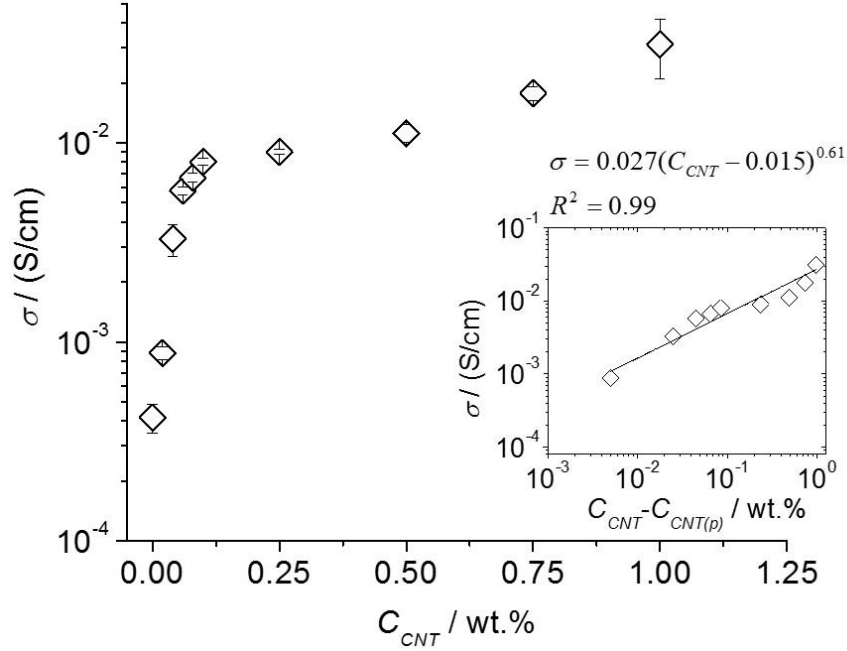


**Fig. 4.15.** Conductivity vs CNT concentration for DX MG/CNT composite gels. The inset shows a fit for the data to the percolation power law.

The fitting result for equation 4.3 are shown in Fig. 4.15 (inset). The percolation threshold of the composite gel was 0.015 wt.%. The value of  $\sigma_0$  is 0.027 S/cm and  $s = 0.61$ . The value for  $C_{CNT(p)}$  is one of the lowest reported values for hydrogel/CNT composites.<sup>19, 23-24</sup> This may be because the CNTs were not dispersed in a homogeneous matrix. The matrix constructed by swollen MG particles is a volume excluded system and is not considered by Equation (4.3). This structure reduced the space for dispersing CNTs and thus reduced the percolation threshold. The value for  $s$  was also smaller than the reported values for 3D CNTs networks in composites.<sup>19</sup> The reason for the relatively low value of  $s$  may cause by the non-uniform arrangements of CNTs within composites. The aggregations process of CNTs might reduce the value of  $s$ .<sup>25</sup>

#### 4.4.4.6 Dynamic rheology measurements

The mechanical properties of both the physical gels (SX MG/CNT) and covalent gels (DX MG/CNT) were examined by the frequency-sweep and strain-sweep dynamic rheology as shown in Fig. 4.16.

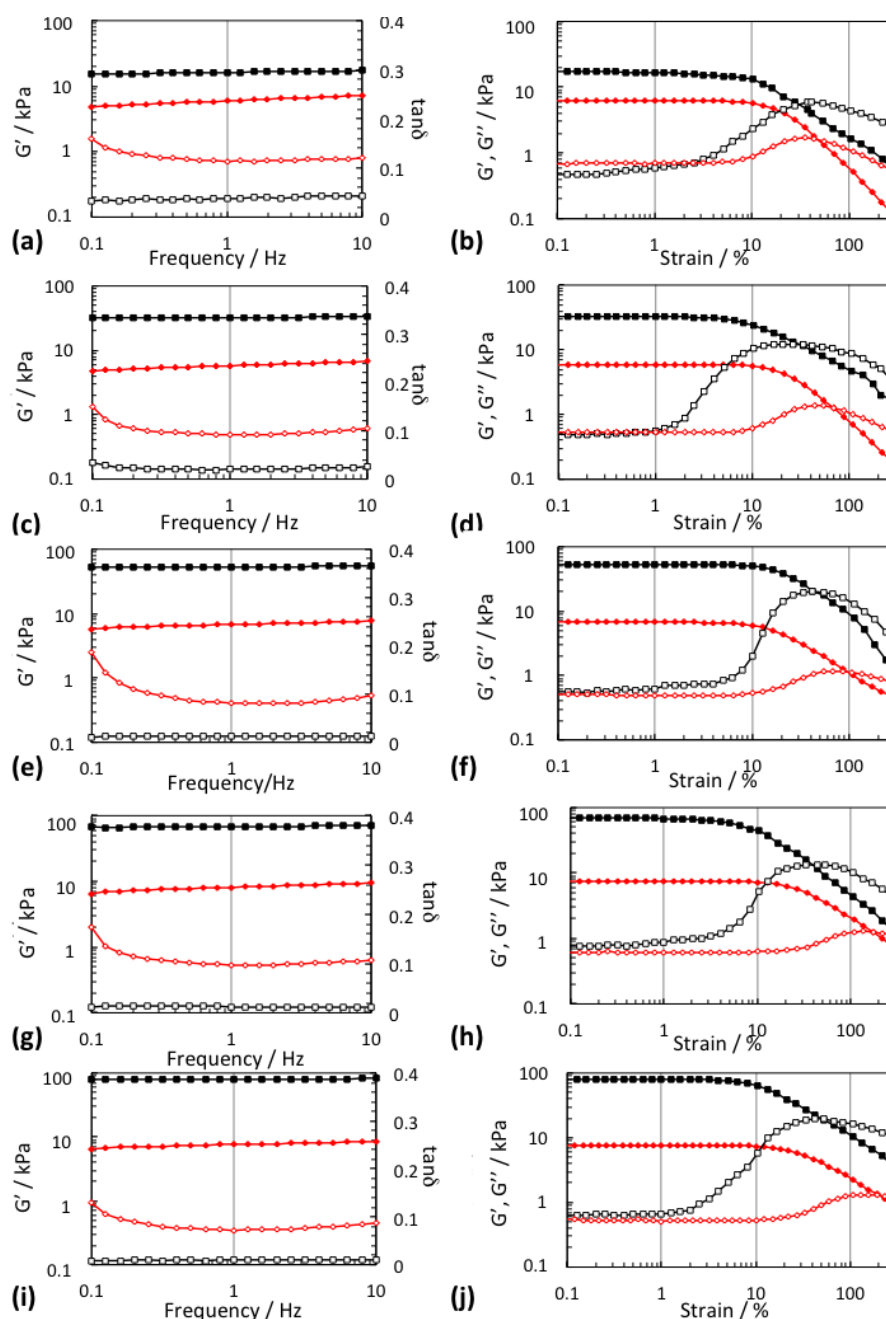


**Fig. 4.16.** Dynamic rheology data for to DX MG/CNT (black) and SX MG/CNT (red), respectively. Frequency-sweep data are in the left column. For (a), (c), (e), (g) and (i), the closed and open symbols are  $G'$  and  $\tan \delta$ , respectively. Strain-sweep data are shown in in the right column. For (b), (d), (f), (h) and (j), The closed and open symbols are  $G'$  and  $G''$ , respectively. The concentrations of CNT used to prepare the composite gels were 0 ((a) and (b)), 0.25 ((c) and (d)), 0.50 ((e) and (f)), 0.75 ((g) and (h)) and 1.0% ((i) and (j)).



For the frequency sweep data, the storage modulus ( $G'$ ) for DX MG/CNT and SX MG/CNT showed weak frequency dependencies. The values of  $G'$  and  $\tan \delta$  ( $= G''/G'$ , where  $G''$  is the loss modulus) for the DX gels were obviously higher than SX because of the formation of covalent interlinkages between the MGs increased networks elasticity. The strain-sweep data for DX MG/CNT and SX MG/CNT showed a typical behaviour of hydrogel<sup>26</sup> or hydrogel composites<sup>27</sup>. The critical strain ( $\gamma_c$ ) is defined as the strain at when  $G' = G''$ . The curves started with a linear viscoelastic behaviour at a low strain before the gel can no longer withstand the strain and began to break. Subsequently, the  $G'$  started to decrease because the break of elastic networks. The  $G''$  values increased until reaching its maximum when  $G'$  and  $G''$  crossed. After that, the gel networks were increasingly destroyed and both  $G'$  and  $G''$  decreased.

To analyse the effect of  $C_{CNT}$  on the rheology behaviour of gels, the data in Fig. 4.16 was summarised and showed in Fig. 4.17. The  $G'$  can be used to assess stiffness, and the  $\gamma_c$  are commonly used to evaluate ductility. The  $G'$  values at 1 Hz and 1% strain were used because they correspond to the linear viscoelastic region. For the physical gels, the values for  $G'$  slightly increased with  $C_{CNT}$ . This is because the MG particles are not tightly inter-linked. They have the same freedom to move under stress. Therefore, compared to DX MGs the SX MG is a less efficient tool to transform stress into the CNT networks. Interestingly, the increase of  $C_{CNT}$  caused a significant different in values of  $\varepsilon_B$ , which indicates the CNTs increased ductility of the physical gel. These results are opposite to the general understanding of a composite conducting soft matrix and stiff fibre reinforcement in which the filler should increase the stiffness and the brittleness. One possible explanation is that the CNT networks can force the MGs to withstand a higher degree of deformation. The

attractive MG-CNT interaction shown in TEM images (Fig. 4.9) may have played a part in the ductility improvement.

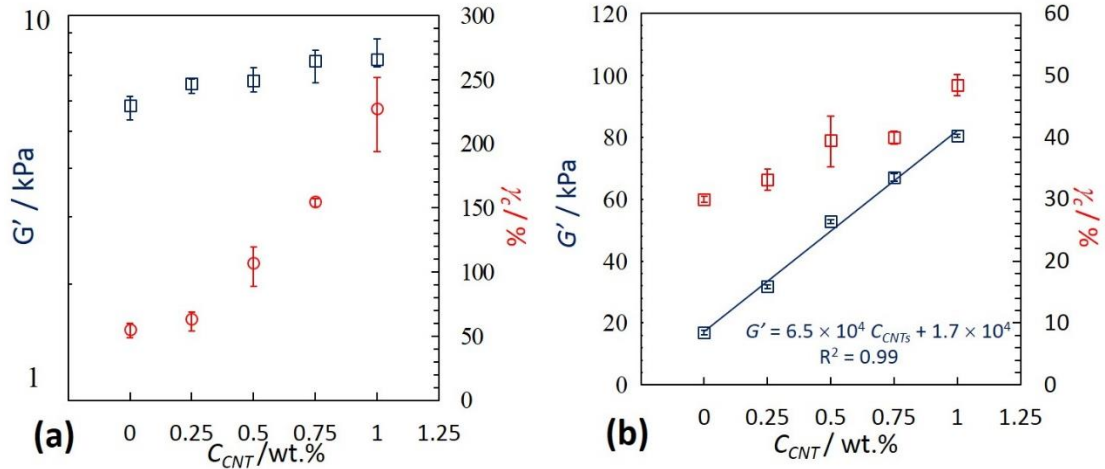


**Fig. 4.17.** Summary of dynamic rheology data for SX MG/CNT and DX MG/CNT gels. (a) showed the effect of CNT concentration on modulus and critical strain for (a) SX MG/CNT and (b) DX MG/CNT.

For the DX gels, there was a significant linear increase in modulus with the  $C_{CNTs}$  (see Fig. 4.17b), which indicate the CNTs were much more effectively involved in energy dissipation than for the physical gels. This is because the MGs were covalently inter-linked. Both the CNT networks and the MG particles had less space for movement and formed a stable macroscopic gel structure. Similar as SX gels, the ductility of DX gels was also increased by increasing  $C_{CNT}$ , which is due to CNT pull out as discussed below.

#### 4.4.4.7 Static axial compression tests

The mechanical properties of the composite gels were also examined by testing the cylinder samples (insets of Fig. 4.18a) using static axial compression. Fig 4.18a shows the stress vs. strain curve for DX MG/CNT gels over a range of  $C_{CNT}$  values. It can be seen that the CNTs enhance the mechanical properties of DX MGs as  $C_{CNT}$  increased. The DX MG/CNT<sub>1.0</sub> is the best sample which can stand both highest strain and stress. The compression modulus values for the samples were calculated and are

shown in Fig. 4.18b. The modulus of the gels increased with the increase of  $C_{CNT}$ . The ductility of gels is shown in Fig. 4.18c which gives the values for the strain-at-break. These values also increased as the  $C_{CNT}$  increased. Those observations followed and confirmed the results shown by rheology data that the modulus and ductility of DX composite gels increased as the  $C_{CNT}$  increased. These results can be explained by a pull-out mechanism. Firstly, in the crack tip the pulled out CNTs contribute to bridging the microcracks. When the CNTs are fully pulled out, the fracture surfaces are totally separated. In this mechanism, the interaction between CNTs and MG matrix dominated.<sup>28</sup> So the energy was wasted because of dissipation and this decreases the crack propagation. Another energy dissipation mechanism is that the CNTs are flexible<sup>29</sup> which the CNT deformation are involved within the MG matrix to resist the separation of fracture MG surfaces.

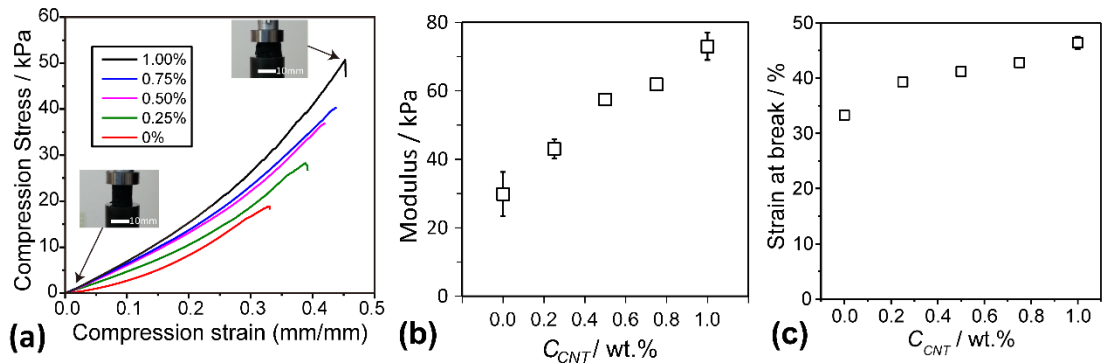


**Fig. 4.18.** Compression data for DX MG/CNT gel composites. (a) shows stress vs strain curve for various CNT concentrations. (b) and (c) show the effect of CNT concentration on modulus and strain at break, respectively.

#### 4.4.4.8 Cytotoxicity study

The cytotoxicity of the DX MG/CNT gel was examined using live / dead and Alamar blue assays. Human adipose-derived human mesenchymal stem cells (ASCs) were used because they have potential application for a range of regenerative medicine/tissue engineering applications including IVD repair.<sup>30-31</sup> Here, the cell viability was studied in the presence of the gel composites. The data from live / dead

assay (Fig. 4.19a and b) showed that over 99% of cells remain alive after exposure to DX MG/CNT<sub>1.0</sub> for 7 days. Furthermore, the cell cytotoxicity data at 1, 4, 7 day time points were similar to the cells not exposed to the gel composites (Fig. 4.19c). Therefore, exposure of adhered ASC cells to DX MG/CNT maintained normal cell viability and also metabolic activity. We conclude that the DX MG/CNT was not cytotoxic under the conditions used.

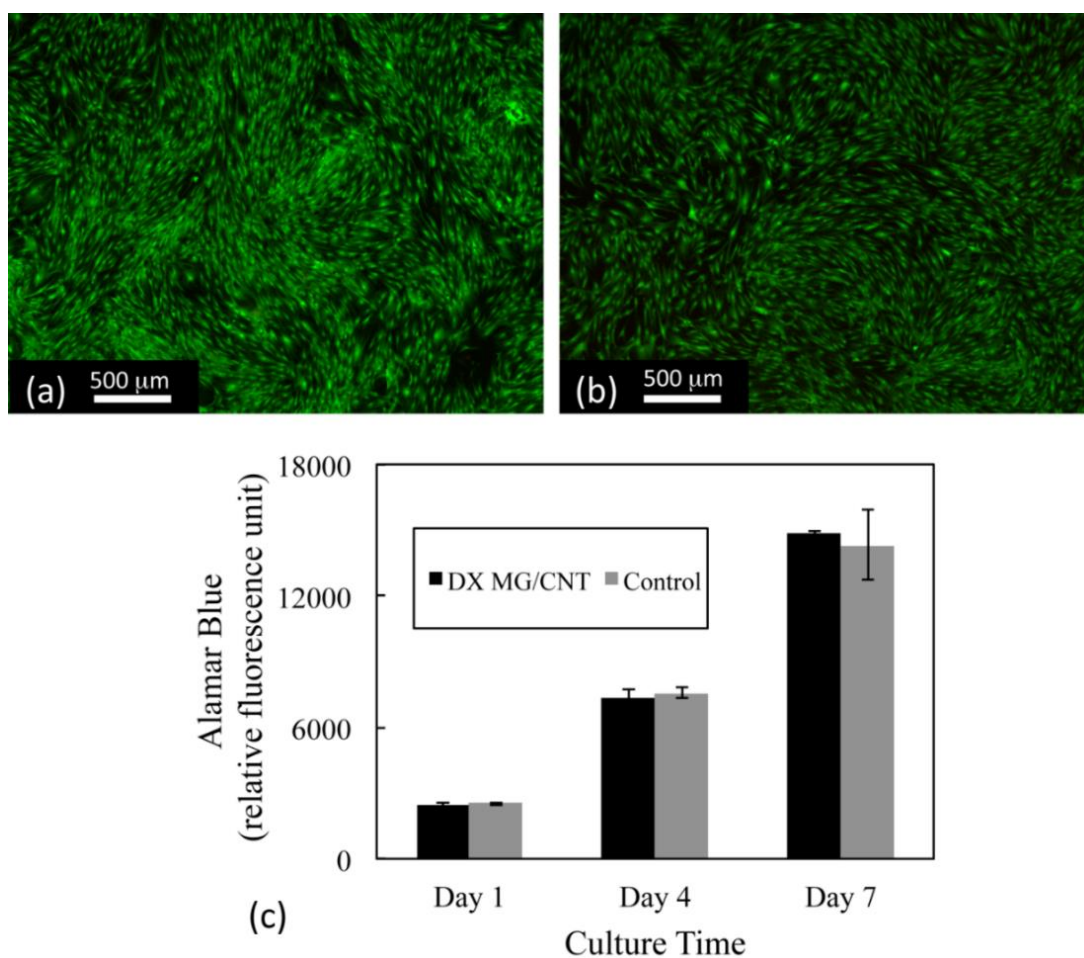


**Fig 4.19.** Cytotoxicity study for DX MG/CNT<sub>1.0</sub>. Live-Dead staining showing (a) ASC cells exposed to DX MG/CNT<sub>1.0</sub> gel at day 7, and (b) showed cells without exposure to the composite at the same condition. (c) Graph showing metabolic activity of MSCs after exposure to the gels for different time periods.

## 4.5 Conclusions

A new type of composite constructed from colloidal building blocks of MGs and CNTs was studied in this chapter. The MG particles played the multiple roles as dispersant and stabiliser for CNTs, building units for gels and macro-crosslinker for covalent gel formation. As the reinforcement, the CNT was used to provide electrical conductivity and enhance the mechanical properties of gels. The ability of the MGs to disperse the CNTs were proved, and the proposed mechanism was explained by a combination of attractive MG-CNT interactions and the excluded volume from swollen MG particles. The physical composite gels were injectable and mouldable. The DX MG/CNTs were electrically conductive which had a very low percolation threshold at 0.15 wt.%. The DX MG/CNT gels were pH-responsive and had the ability to avoid falling apart in an aqueous environment. The mechanical properties of both composite gels can be tuned by the concentration of CNT. The data showed both modulus and the ductility of the SX MG/CNT and DX MG/CNT gels increased with the loading of CNTs. The ductility increase was ascribed to dissipation associated with the pull out of the CNTs from the matrix. The cytotoxic data showed the DX MG/CNT gels are not toxic to cells. Our injectable DX MG/CNT showed the potential for applications in soft tissue engineering such as heart tissue repair and electronic skin.

## 4.6 References

1. Milani, A. H.; Freemont, A. J.; Hoyland, J. A.; Adlam, D. J.; Saunders, B. R., Injectable doubly cross-linked microgels for improving the mechanical properties of degenerated intervertebral discs. *Biomacromolecules* **2012**, 13, 2793-801.
2. Yamada, T.; Hayamizu, Y.; Yamamoto, Y.; Yomogida, Y.; Izadi-Najafabadi, A.; Futaba, D. N.; Hata, K., A stretchable carbon nanotube strain sensor for human-motion detection. *Nat Nanotech.* **2011**, 6, 296-301.
3. Breuer, O.; Sundararaj, U., Big returns from small fibers: A review of polymer/carbon nanotube composites. *Polym. Compos.* **2004**, 25, 630-645.
4. Zhu, Z. G.; Garcia-Gancedo, L.; Chen, C.; Zhu, X. R.; Xie, H. Q.; Flewitt, A. J.; Milne, W. I., Enzyme-free glucose biosensor based on low density CNT forest grown directly on a Si/SiO<sub>2</sub> substrate. *Sensors and Actuators B: Chemical* **2013**, 178, 586-592.
5. Mittal, G.; Dhand, V.; Rhee, K. Y.; Park, S.-J.; Lee, W. R., A review on carbon nanotubes and graphene as fillers in reinforced polymer nanocomposites. *J. Ind. Eng. Chem.* **2015**, 21, 11-25.
6. Claussen, J. C.; Franklin, A. D.; ul Haque, A.; Porterfield, D. M.; Fisher, T. S., Electrochemical Biosensor of Nanocube-Augmented Carbon Nanotube Networks. *ACS Nano* **2009**, 3, 37-44.
7. Bhirde, A. A.; Patel, V.; Gavard, J.; Zhang, G.; Sousa, A. A.; Masedunskas, A.; Leapman, R. D.; Weigert, R.; Gutkind, J. S.; Rusling, J. F., Targeted Killing of Cancer Cells in Vivo and in Vitro with EGF-Directed Carbon Nanotube-Based Drug Delivery. *ACS Nano* **2009**, 3, 307-316.
8. Dong, C.; Campell, A. S.; Eldawud, R.; Perhinschi, G.; Rojanasakul, Y.; Dinu, C. Z., Effects of acid treatment on structure, properties and biocompatibility of carbon nanotubes. *Appl. Surf. Sci.* **2013**, 264, 261-268.
9. Mikael, P. E.; Amini, A. R.; Basu, J.; Josefina Arellano-Jimenez, M.; Laurencin, C. T.; Sanders, M. M.; Barry Carter, C.; Nukavarapu, S. P., Functionalized carbon nanotube reinforced scaffolds for bone regenerative engineering: fabrication, in vitro and in vivo evaluation. *Biomed. Mater.* **2014**, 9, 035001.
10. Zhang, S.; Shao, T.; Bekaroglu, S. S. K.; Karanfil, T., The Impacts of Aggregation and Surface Chemistry of Carbon Nanotubes on the Adsorption of Synthetic Organic Compounds. *Environ. Sci. Technol.* **2009**, 43, 5719-5725.
11. Bertels, E.; Bruyninckx, K.; Kurttepel, M.; Smet, M.; Bals, S.; Goderis, B.,

Highly Efficient Hyperbranched CNT Surfactants: Influence of Molar Mass and Functionalization. *Langmuir* **2014**, 30, 12200-12209.

12. Gegenhuber, T.; Gröschel, A. H.; Löbbling, T. I.; Drechsler, M.; Ehlert, S.; Förster, S.; Schmalz, H., Noncovalent Grafting of Carbon Nanotubes with Triblock Terpolymers: Toward Patchy 1D Hybrids. *Macromolecules* **2015**, 48, 1767-1776.

13. Koh, B.; Cheng, W., Mechanisms of Carbon Nanotube Aggregation and the Reversion of Carbon Nanotube Aggregates in Aqueous Medium. *Langmuir* **2014**, 30, 10899-10909.

14. Vaisman, L.; Wagner, H. D.; Marom, G., The role of surfactants in dispersion of carbon nanotubes. *Adv. Colloid Interface Sci.* **2006**, 128–130, 37-46.

15. Huang, Y. Y.; Terentjev, E. M., Dispersion of Carbon Nanotubes: Mixing, Sonication, Stabilization, and Composite Properties. *Polymers* **2012**, 4, 275.

16. Montazeri, A.; Chitsazzadeh, M., Effect of sonication parameters on the mechanical properties of multi-walled carbon nanotube/epoxy composites. *Mater. Des* **2014**, 56, 500-508.

17. Bokobza, L., Raman spectroscopic characterization of multiwall carbon nanotubes and of composites. *Express Polymer Letters* **2012**, 6, 601-608.

18. Marsh, D. H.; Rance, G. A.; Zaka, M. H.; Whitby, R. J.; Khlobystov, A. N., Comparison of the stability of multiwalled carbon nanotube dispersions in water. *Physical Chemistry Chemical Physics* **2007**, 9, 5490-5496.

19. Grunlan, J. C.; Mehrabi, A. R.; Bannon, M. V.; Bahr, J. L., Water-Based Single-Walled-Nanotube-Filled Polymer Composite with an Exceptionally Low Percolation Threshold. *Adv. Mater.* **2004**, 16, 150-153.

20. Marsh, D. H.; Rance, G. A.; Zaka, M. H.; Whitby, R. J.; Khlobystov, A. N., Comparison of the stability of multiwalled carbon nanotube dispersions in water. *Phys. Chem. Chem. Phys.* **2007**, 9, 5490-6.

21. Moore, V. C.; Strano, M. S.; Haroz, E. H.; Hauge, R. H.; Smalley, R. E.; Schmidt, J.; Talmon, Y., Individually Suspended Single-Walled Carbon Nanotubes in Various Surfactants. *Nano. Lett.* **2003**, 3, 1379-1382.

22. Bayazit, M. K.; Clarke, L. S.; Coleman, K. S.; Clarke, N., Pyridine-Functionalized Single-Walled Carbon Nanotubes as Gelators for Poly(acrylic acid) Hydrogels. *J. Am. Chem. Soc.* **2010**, 132, 15814-15819.

23. Bauhofer, W.; Kovacs, J. Z., A review and analysis of electrical percolation in

carbon nanotube polymer composites. *Compos. Sci. Technol.* **2009**, 69, 1486-1498.

24. De Volder, M. F. L.; Tawfick, S. H.; Baughman, R. H.; Hart, A. J., Carbon Nanotubes: Present and Future Commercial Applications. *Science* **2013**, 339, 535-539.

25. Sandler, J. K. W.; Kirk, J. E.; Kinloch, I. A.; Shaffer, M. S. P.; Windle, A. H., Ultra-low electrical percolation threshold in carbon-nanotube-epoxy composites. *Polymer* **2003**, 44, 5893-5899.

26. Liu, R.; Milani, A. H.; Freemont, T. J.; Saunders, B. R., Doubly crosslinked pH-responsive microgels prepared by particle inter-penetration: swelling and mechanical properties. *Soft Matter* **2011**, 7, 4696-4704.

27. Cui, Z.; Milani, A. H.; Greensmith, P. J.; Yan, J.; Adlam, D. J.; Hoyland, J. A.; Kinloch, I. A.; Freemont, A. J.; Saunders, B. R., A Study of Physical and Covalent Hydrogels Containing pH-Responsive Microgel Particles and Graphene Oxide. *Langmuir* **2014**, 30, 13384-13393.

28. Cotterell, B.; Chia, J. Y. H.; Hbaieb, K., Fracture mechanisms and fracture toughness in semicrystalline polymer nanocomposites. *Eng. Fract. Mech.* **2007**, 74, 1054-1078.

29. Wichmann, M. H. G.; Schulte, K.; Wagner, H. D., On nanocomposite toughness. *Compos. Sci. Technol.* **2008**, 68, 329-331.

30. Acosta, F. L., Jr.; Metz, L.; Adkisson, H. D.; Liu, J.; Carruthers-Liebenberg, E.; Milliman, C.; Maloney, M.; Lotz, J. C., Porcine intervertebral disc repair using allogeneic juvenile articular chondrocytes or mesenchymal stem cells. *Tissue Eng. Part A* **2011**, 17, 3045-55.

31. Steck, E.; Bertram, H.; Abel, R.; Chen, B.; Winter, A.; Richter, W., Induction of intervertebral disc-like cells from adult mesenchymal stem cells. *Stem Cells* **2005**, 23, 403-11.



## **Chapter 5: Using intra-microgel crosslinking to control the mechanical properties of doubly crosslinked microgels**

### **5.1 Abstract**

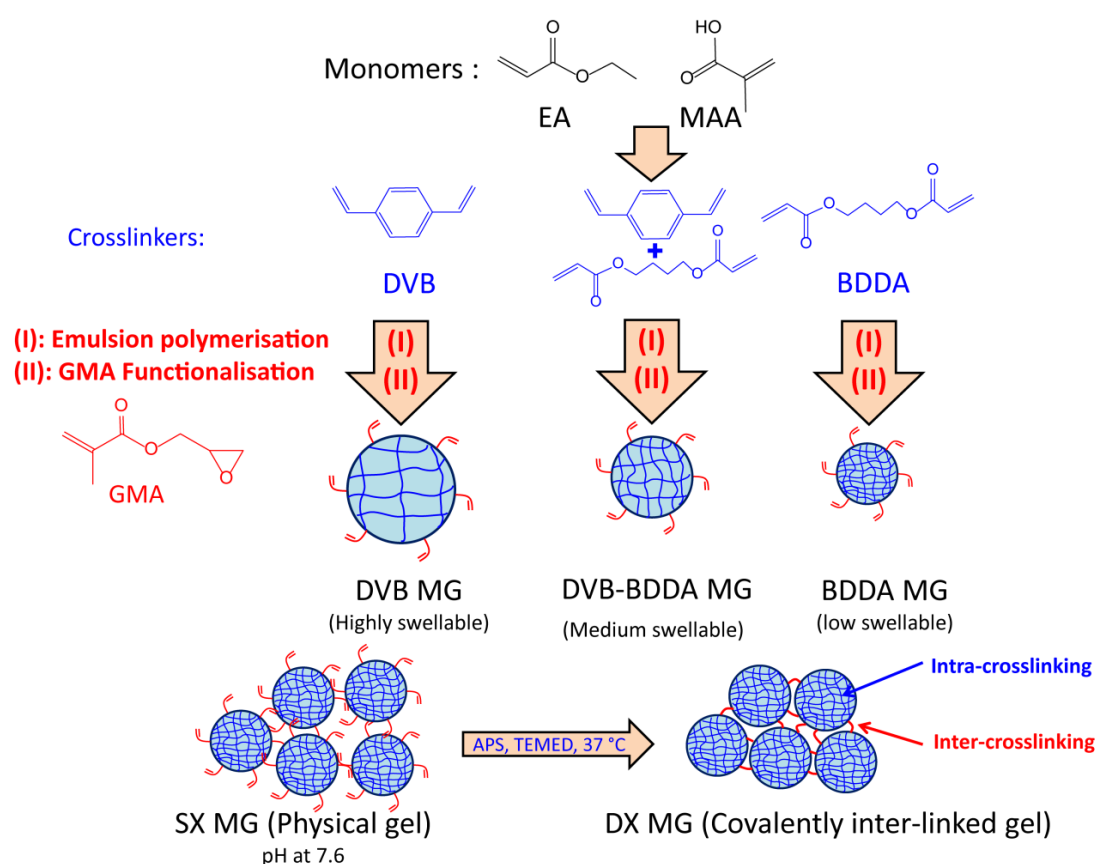
In this chapter, three types of microgels (MGs) were studied by tuning the crosslinking monomers and we expected to have more ductile hydrogels while the composite gels studied in the earlier chapters were relative brittle. The MGs were synthesised by emulsion polymerisation of ethyl acrylate, methacrylic acid and a crosslinking monomer. Three types of MGs were prepared using different crosslinking monomers: divinylbenzene (DVB); 1,4-butanediol diacrylate (BDDA) or a 1:1 mixture of both DVB and BDDA. Compared to the earlier chapters, DVB was a new crosslinking monomer. Here, the effects of intra-MG crosslinking of the MGs on the swelling behaviour and the mechanical properties were investigated. The swelling behaviours were studied by DLS and the mechanical properties were studied by both dynamic rheology and uniaxial compression measurements. The MGs containing DVB demonstrated higher swelling and more ductile properties when compared with the control sample which was the MG formed with BDDA. The average compressive strain for the DVB-containing DX MGs before the break was 76 % which is the highest value reported for a DX MG system to date. The study also showed a potential method to tune the DX MG properties by adjusting the DVB and BDDA contents within the MG particles. The results of this study provide design tools for improving DX MG ductility and hence increasing the range of potential applications for this new class of hydrogel.

## 5.2 Introduction

Hydrogels are high water content swollen polymer network and are attracting large interest in biomaterial applications<sup>1-3</sup> such as drug delivery<sup>4</sup>, regenerative medicine<sup>5</sup> and soft tissue engineering<sup>6-7</sup> due to their strong property resemblance with native extracellular matrix<sup>8</sup>. The swelling and mechanical properties of hydrogels are directly connected to the number-density of elastically effective chains<sup>9</sup>. When compared to high ductility gels such as double network hydrogels<sup>10</sup>, our previous doubly crosslinked microgels (DX MGs) were relatively brittle<sup>11-12</sup>. In the earlier chapters, the composite strategy has proved an efficient method to improve the stiffness of the DX MGs. However, a lack of ductility is a key limitation for the DX MG systems. In this study, we aimed to design a new microgel (MG) system to reduce the brittleness.

Considering the polymer networks have the same concentration of crosslinks, when it disperses in a good solvent, a network containing an inhomogeneous distribution of crosslinks tend to swell more than the one with uniform distribution. The distribution of crosslinking junctions in polymer particles is determined during emulsion polymerisation and controlled by the nature and concentration of crosslinker<sup>13-15</sup>. The preparation of uniformly crosslinked polymer particles has been reported<sup>16-17</sup>. Meanwhile, inhomogeneous crosslinking distributions have also been studied to prepare highly swellable MGs<sup>18</sup>. The idea of changing crosslinking distribution is to improve the swelling behaviour of pH-responsive MGs by using divinylbenzene (DVB) to replace the 1,4-butanediol diacrylate (BDDA) as the crosslinker is depicted in Scheme 5.1. We expect the inhomogeneous junction distribution could improve the inter-linking of the particles when DX gel formed covalently and produced a

more ductile hydrogel. BDDA and EA have similar solubility. Conversely, DVB is a more hydrophobic monomer<sup>19-20</sup>. Furthermore, if we assume that when paired with EA, the reactivity rate for DVB and BDDA are similar to those for styrene and hydroxyethyl acrylate, respectively<sup>21</sup>, then DVB should distribute less uniformly within the EA matrix compared to BDDA. Consequently, major differences in the partitioning of the crosslinker into the growing particles were expected for DVB and BDDA.



**Scheme 5.1.** Outline of the method used to prepare MGs and DX MGs. The MG particles contained ethyl acrylate (EA) and methacrylic acid (MAA) and were prepared by emulsion polymerisation. Divinylbenzene (DVB), 1,4-butanediol diacrylate (BDDA) or a mixture of DVB and BDDA were used as intra-MG crosslinkers. The MGs are termed singly-crosslinked microgels (SX MGs) and were functionalised with glycidyl methacrylate (GMA). Concentrated dispersions formed physical gels ( $\text{pH} > \text{pK}_a$ ) which were transformed into doubly crosslinked microgels (DX MGs) by covalent inter-MG crosslinking.

The first MG system using poly(EA-co-MAA-co-BDDA) were introduced by Rodriguez et al in 1994<sup>22</sup>. A core-shell model was introduced to simulate the

properties of this system. In the past decade, Saunders' group and others have expanded this family of pH-responsive MGs.<sup>23-24</sup> In 2011 these MGs (after vinyl functionalisation) were inter-linked together to form hydrogels.<sup>11</sup> DX MGs have potential application in regeneration medicine for intervertebral disc (IVD) repair.<sup>25</sup> In this chapter, three MGs containing different crosslinker combinations were synthesised using emulsion polymerisation as shown in Scheme 5.1. As the BDDA system is our old system, the new system (DVB-containing gels) were compared. A hybrid MG system was also synthesised by using a mixture of 0.5 mol.% of DVB and 0.5 mol.% of BDDA. These MGs were functionalised by glycidyl methacrylate (GMA) to achieve formation of covalent inter-linking (Scheme 5.1). The three MG (poly(EA-*co*-MAA-*co*-DVB), poly(EA-*co*-MAA-*co*-DVB-*co*-BDDA), poly(EA-*co*-MAA-*co*-BDDA) dispersions are abbreviated as SX DVB, SX DVB-BDDA and SX BDDA, respectively. The SX term differs from DX because there is no interlinking of particles in the SX system. The SX MG dispersions are formed physical gels at pH ~ 7.6, whereas, the formation of covalently inter-linked MGs (i.e., DX MGs) was achieved by adding ammonium persulfate (APS) and *N,N,N',N'*-tetramethylethylenediamine (TEMED) at 37 °C.

The motivation and aim of this chapter is to improve the ductility of DX MG system. The improvement is sought from using a different crosslinking monomer which can provide a distinct crosslinking distribution within the MG particles. The effects were examined in swelling behaviours, morphologies and the mechanical properties which are important factors for biomaterial applications. The dynamic rheology and static axial compression tests showed that inclusion of DVB produced a remarkably ductile DX MG. An analysis based on data indicates that the nature of crosslinking monomer can control the swelling properties of MG particles. In addition, the

analysis suggested that the swelling of MG relate to the mechanical properties and therefore, the crosslinking monomer can further determine the mechanical properties of the DX MG. The improved ductility of the DX DVB gels can provide more applications in soft tissue engineering, such as IVD repair.<sup>25</sup>

## 5.3 Experimental

### 5.3.1 Materials

EA (99%), MAA (99%), GMA (97%), BDDA (90%), DVB (80%), NaOH (97%), APS (98%), sodium dodecyl sulphate (SDS,  $\geq 92.5\%$ ), TEMED (99%) and dipotassium phosphate ( $K_2HPO_4$ , 97%) were purchased from Sigma-Aldrich and used as received. All water was of ultra-high purity de-ionised quality.

### 5.3.2 Microgel synthesis

The synthesis of SX DVB, SX DVB-BDDA and SX BDDA MGs used seed-feed emulsion polymerisation. The compositions of the mixed monomer feeds are shown in Table 5.1. The preparation of SX DVB is given in detail as an example: A mixed co-monomer solution (250 g) containing EA (164.4 g, 1.64 mol.), MAA (82.2 g, 0.95 mol.) and DVB (3.4 g, 0.026 mol.) was prepared. Seed formation was conducted using a portion of the co-monomer mixture (31.5 g) after adding water (510 g) containing SDS (1.8 g) and  $K_2HPO_4$  (3.15 g of 7.0 wt.% solution) under a nitrogen atmosphere. Subsequently, the APS (10.0 g of 2.0 wt.% solution) was introduced rapidly. The seed was formed at 80 °C with mechanical stirring (300 rpm) for 30 minutes. The remaining co-monomer solution was added uniformly to the seed at a rate of about 2.4 g/min feed by a pump (i.e. feed 90 minutes for remaining 218.5 g monomers mixture). After completion of the feed, the temperature was maintained at 80 °C for a further 2.5 h. During the reaction, samples were collected from reaction solution every 15 minutes to monitor the growth of particles by using DLS measurement. Each collected sample was diluted by buffer (pH = 4) and cooled in an ice bath. Filtration was used to remove aggregates from the main product after

cooling in the ice bath. Finally, the product was extensively dialysed against water for three weeks and store at 3°C in the fridge.

**Table 5.1.** Compositions of the mixed co-monomer solutions used to synthesise the MGs.

Sample Abbreviations	EA mol.%	MAA mol.%	DVB mol.%	BDDA mol.%
SX DVB	62.6	36.4	1.0	0
SX DVB-BDDA	62.6	36.4	0.5	0.5
SX BDDA	62.6	36.4	0	1.0

The GMA functionalisation for all of the MGs used the same conditions. The functionalisation process used here differs from earlier chapters where the pH of the MG solution was not adjusted at first and reaction time was shortened to 4 h. GMA (30 g, 0.2 mol.) was added to MG dispersion (400 g, 5 wt.%) in a 2 L flask. The dispersion was mixed by mechanical stirring at 400 rpm and heated at 50 °C for 4 h. After the reaction, the product was cooled in an ice bath and the aggregates were removed by a film mesh (pore size = 0.2 mm). The unreacted GMA was removed by washing with chloroform (200 ml) in a separating funnel twice. Any remaining chloroform was removed by rotary evaporation (vacuum = 160 mbar) at room temperature, and the final GMA-functionalised MG was concentrated to about 10 wt.% (vacuum = 20 mbar). The final wt.% of MG was determined by a gravimetric total solids content test.

The other MGs were prepared using the procedure described above by replacing DVB with either a 1:1 DVB/BDDA mixture (for SX DVB-BDDA) or BDDA (for SX BDDA) as shown in Table 5.1.

### 5.3.3 Preparation of doubly crosslinked microgels

All of the covalently interlinked DX MG gels were prepared using the same conditions (depicted in Scheme 5.1). Aqueous NaOH solution (~700 µl, 4 M) was added to MG dispersion (10 g of 10 wt.% dispersion) and the pH adjusted to ~7.6 to form a SX MG physical gel. DX MGs were formed by mixing APS solution (250 µl, 1.6 wt. %) with the SX MG physical gel and then TEMED solution (250 µl, 2 wt.%) with stirring. The physical gels were subsequently heated in sealed moulds at 37 °C for 2 h to form DX MGs.

### 5.3.4 Physical Measurements

Potentiometric titration was conducted using a Mettler Toledo DL15 titrator. The titrations were performed by adding 3 g MG (10wt.%) in 40 g NaCl solution (0.01 M) and the titrant was aqueous NaOH solution (1.0 M). Dynamic light scattering (DLS) measurements were conducted using a 50 mW He/Ne laser operated at 633 nm with a standard avalanche photodiode (APD) and 90° detection optics connected to a Malvern Zetasizer Nano ZS90 autocorrelator. For measuring the pH-responsive swelling, a series of buffer solutions were prepared (pH 4.0 to 11.0). The ionic strength of all buffer was about 0.1 M excluding pH 4.0 solution which was prepared by dilute hydrochloride acid solution to avoid the aggregation of SX MGs. The swelling behaviours of the SX MGs were assessed using the particle volume swelling ratio ( $Q$ ) which was calculated using the following equation.

$$Q = \left( \frac{d_{h(x)}}{d_{h(4)}} \right)^3 \quad (5.1)$$

where  $d_h$  is the hydrodynamic diameter and  $x$  represents the pH value. The MG particles were considered to be in their collapsed state at pH 4.0.



TEM measurements were obtained using a JEOL JEM-2011F instrument operated at an accelerating voltage of 200 kV and the samples were deposited onto 200 mesh copper TEM grids. SEM images were obtained using a Philips FEGSEM XL30 instrument. The freeze-dried DX MG samples were coated by platinum with a thickness of about 3 nm.

Dynamic rheology measurements were conducted using a TA Instruments AR-G2 temperature-controlled rheometer equipped with an environmental chamber. A parallel plate geometry (diameter = 20 mm) was used. Each DX MG sample was prepared in a rubber ring which was clamped in the middle of two parallel glass slides. The shape of sample matches the parallel plate of rheometer with a diameter of 20 mm and a thickness of 1 mm. For the strain-sweep data, a frequency of 1 Hz was used to test the samples. Uniaxial compression measurements were conducted using an Instron series 5569 load frame equipped with a 100 N compression testing head with a testing rate of 2 mm per minute. The samples were cylindrical, and the height and diameter were both 12 mm.

## 5.4 Results and discussion

### 5.4.1 Microgel particle size and pH-triggered swelling

Three types of GMA-functionalised MG were prepared for this study. The SX MGs were prepared using 1.0 mol.% of either DVB or BDDA or a crosslinking monomer mixture containing both DVB (0.5 mol.%) and BDDA (0.5 mol.%) (see Table 5.1). In the following sections, the difference in swelling behaviour, morphology, mechanical properties of both SX MGs and DX MGs will be mentioned which is resulted from the crosslinkers only within the MG particles.

#### 5.4.1.1 Potentiometric titration

The content of acid group ( $-\text{COOH}$ ) and the content of GMA functionalisation of SX MGs was determined by potentiometric titration data. The  $-\text{COOH}$  contents were directly determined by the potentiometric titration data of SX MGs, and the GMA contents were determined from the difference of MAA content in particles before and after GMA functionalisation (i.e. the mol.% of MAA consumed during GMA functionalisation). The measurements were performed in the presence of aqueous 0.01 M NaCl solution as electrolyte background.

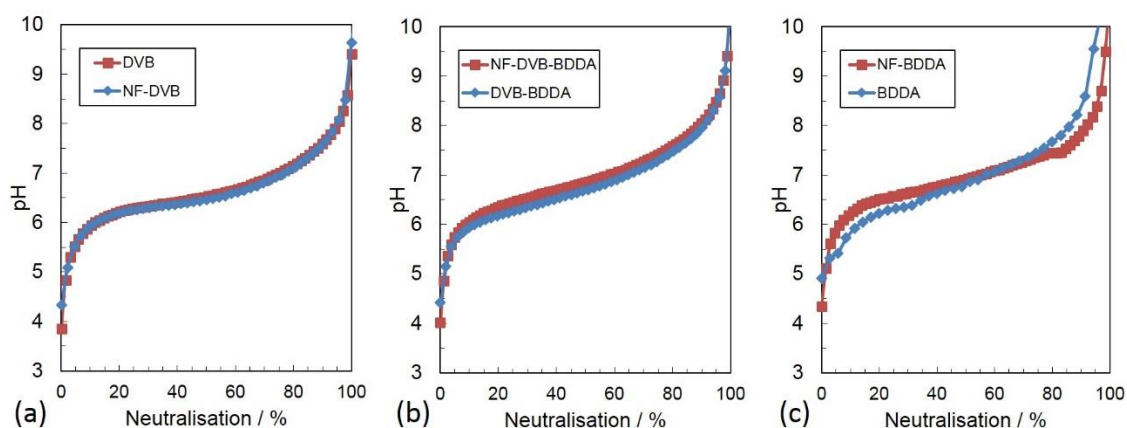


**Fig. 5.1.** Potentiometric titration data for (a) DVB, (b) DVB-BDDA, (c) BDDA MGs. The NF in the captions represent the non-functional MGs which is used to distinguish from functional MGs.

The calculated values from titration data were shown in Table 5.2. All the SX MGs had similar -COOH contents (about 32 mol.%) and the concentrations of GMA in the MGs were between 5.3 and 8.2 mol.%, which is enough to achieve the DX process. The  $pK_a$  values of these MGs were in the range of 6.5 to 6.9 (Table 5.2). Those  $pK_a$  values are less than physiological pH (~7.4) which means that the MG particles (and respective DX MGs) would be swollen in such an environment.

**Table 5.2.** Characterisation data for the MGs investigated in this work.

Abbreviation	mol.% GMA <sup>a</sup>	mol.% MAA <sup>b</sup>	$d_{n(TEM)} / \text{nm}$ [CV] <sup>c</sup>	$d_{h(4)} / \text{nm}^d$	$d_{h(8)} / \text{nm}^d$	$Q_{(8)}^e$	$pK_a^f$
SX DVB	5.3	32.5	55 [12]	79	321	68	6.5
SX DVB-BDDA	8.2	32.4	57 [12]	81	280	41	6.7
SX BDDA	6.3	31.1	64 [10]	91	217	13	6.9

<sup>a</sup> Calculated from the difference in the mol.% MAA values measured using potentiometric titration before and after GMA functionalisation. <sup>b</sup> MAA content of SX MG particles. <sup>c</sup> Number-average diameters determined from TEM images. The number in brackets is the coefficient of variation. <sup>d</sup> Hydrodynamic diameters measured at pH values of 4.0 and 8.0. <sup>e</sup> Volume-swelling ratio calculated from the  $d_{h(8)}$  and  $d_{h(4)}$  values for the parent microgel using equation (1). <sup>f</sup> Apparent  $pK_a$  values.

#### 5.4.1.2 DLS measurements

The hydrodynamic diameter ( $d_h$ ) of the SX MGs over a range of pH values was determined by DLS measurements (see Fig. 3.3). The  $d_h$  values for the three SX MGs were in the range of 79 to 91 nm at pH 4.0 (Table 5.2), which is the collapsed state, and the  $d_{h(4)}$  value decreased with increasing DVB content.

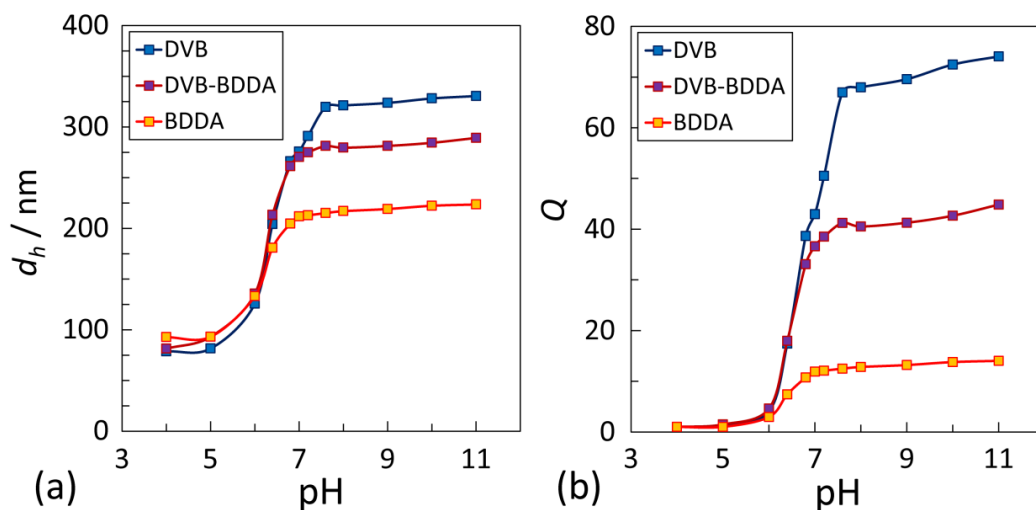


**Fig. 5.2.** (a) Hydrodynamic diameters and (b) particle volume-swelling ratios ( $Q$ ) of SX MG particles at pH 4 to pH 11 measured at various values.

The MG systems were pH-responsive, and the particles swelled when the increasing pH increased (Fig. 5.2a). The variation of particles size is due to neutralisation of  $-\text{COOH}$  groups. For MG particles, the polymer chain expansion of MG particles was caused by inter-segment electrostatic repulsion from  $-\text{COO}^-$  groups. A strong effect from crosslinking monomer on the pH-dependent swelling behaviour can be seen in Fig. 5.2. The extent of pH-triggered swelling strongly increased as the DVB content increased. This was caused by the nature of the crosslinker because all three SX MGs had very similar  $-\text{COOH}$  group contents. The  $Q$  values for the SX MG systems are shown in Fig. 5.2b. The  $Q$  value decreased in the order SX DVB > SX DVB-BDDA > SX BDDA and therefore we identify SX DVB as highly swellable particles with a  $Q$  of 68, by contracts, the SX BDDA and SX DVB-BDDA are low swelling ( $Q = 13$ ) and medium swelling particles ( $Q = 41$ ). It is a new observation that the MGs containing DVB as crosslinker swelled more than those containing BDDA. This trend shows that there was a lower number-average density of intra-particle elastically effective chains ( $v_{\text{intra}}$ ) for the DVB-containing MGs. This behaviour is attended to an inhomogeneous crosslinking distribution within DVB MGs and therefore, DVB was a less efficient crosslinker than BDDA for these MGs.

#### 5.4.1.3 Transmission Electron Microscopy

The TEM images of three SX MGs were shown in Fig. 5.3. The particles were spherical and the number-average diameters from TEM ( $d_{n(TEM)}$ ) were in the range of 55 to 64 nm and were not significantly different (Table 5.2). Compared to the respective hydrodynamic diameter ( $d_{h(4)}$ ) in the collapsed state, the  $d_{n(TEM)}$  values are smaller. Because the MGs particles are not totally “dry” in water.<sup>26</sup> The particles still absorbed water molecules in the collapsed state which give a larger size in DLS. The MG particles had a tendency to partially coalesce when dried on the carbon film as shown from insets of Fig. 5.3, which showed the MG dispersion had a good film-forming properties<sup>27</sup>. Interestingly, the higher magnification images show significant differences in the area of particle-particle contact which is indicated by yellow arrows. The particle-particle contact points for the MGs containing DVB and DVB-BDDA were relatively smooth (insets in Fig. 5.3a and b) and no clear particle-particle boundary can be seen. By contrast, a distinct particle-particle boundary can be seen for the MG particles containing BDDA (insets in Fig. 5.3c). Coalescence of MG particles was obstructed by intra-particle crosslinking. Consequently, these data suggest that the BDDA-containing MG particles had a relatively high concentration of crosslinks at the periphery of the particles compared to the DVB-containing MG particles.

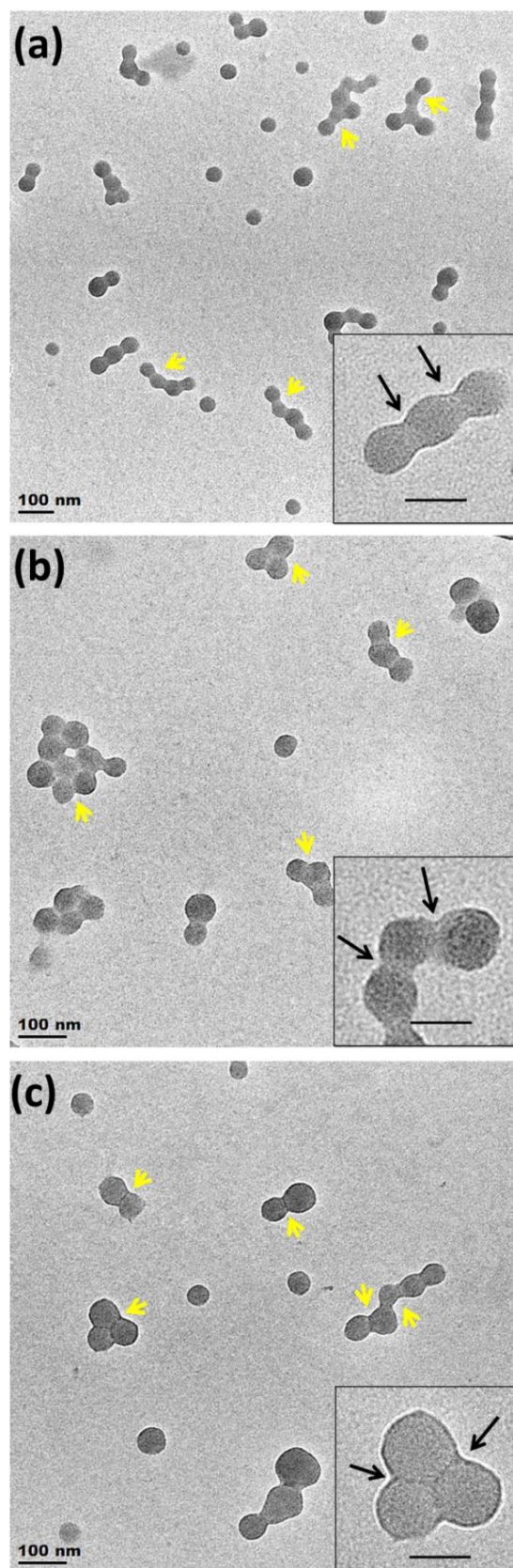


**Fig. 5.3.** TEM images of (a) SX DVB, (b) SX DVB-BDDA and (c) SX BDDA particles. The arrows indicate the particle-particles contact area. The insets show higher resolution images of several representatives connected particles. The scale bars for each inset represent 50 nm.

#### 5.4.2 Dynamic rheological measurements for SX MGs and DX MGs

In this study, SX MGs dispersions and DX MGs with a solid content of 10 wt.% were prepared and examined. The SX MG physical gel formation was achieved by increasing the pH at 7.6, and such gels are transparent and injectable in SX DVB is shown as an example in Fig 5.4. Physical gels formed because the MGs particles were trapped by the neighbour particles when all particles are swollen at certain pH. For the covalently DX gels, they were formed by adding initiator (APS) and accelerator (TEMED) to the physical gels and heating to 37 °C in order to link the particles with each other by the reaction of GMA groups. This physical gel to covalently gel transformation occurred after injection medical (physical gel state) and could fill an irregular space to transform to stronger covalently gel. This approach may be suitable for biomaterial applications<sup>25</sup>.

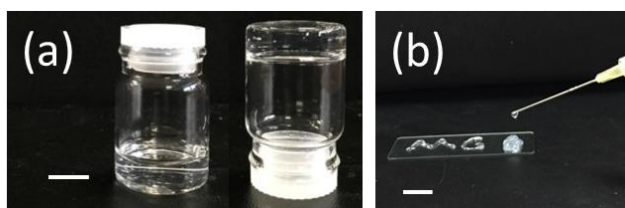


**Fig. 5.4.** (a) the inversion test of DVB SX (b) “MG” letters written by continuous injection of DVB SX gel.

The mechanical properties were studied by strain-sweep dynamic rheological measurements for both SX MGs and DX MGs in order to study the effect of crosslinking monomer on the viscoelastic properties (Fig. 5.5). Here, the storage modulus ( $G'$ ), the loss modulus ( $G''$ ) and  $\tan \delta (= G''/G')$  were used to study the viscoelasticity of various MG gels. All data in Fig. 5.5 had a similar shape and were characterised by three regions: The curves start with linear  $G'$  and  $G''$  behaviours in low strain region; Then a non-linear decrease of  $G'$  and an increase of  $G''$  at

intermediate strain occurs and  $G''$  increases until  $G'' = G'$  ( $\tan \delta = 1$ ). (3) at high strain the  $G''$  starts to decrease.

For the low strain region, the values of  $G'$  and  $G''$  were stable and we can consider that the gel can withstand the strain in this region without any structural damage. So the  $G'$  are compared to access the elasticities of the gels. As shown in Fig. 5.5, the modulus of DX MG gels is always higher than the value for the respective SX MG gel which can be seen as a proof of DX formation. Both SX BDDA and DX BDDA MGs have the highest  $G'$  values in the SX and DX series which indicates the BDDA containing gels are more elastic than DVB containing gels.

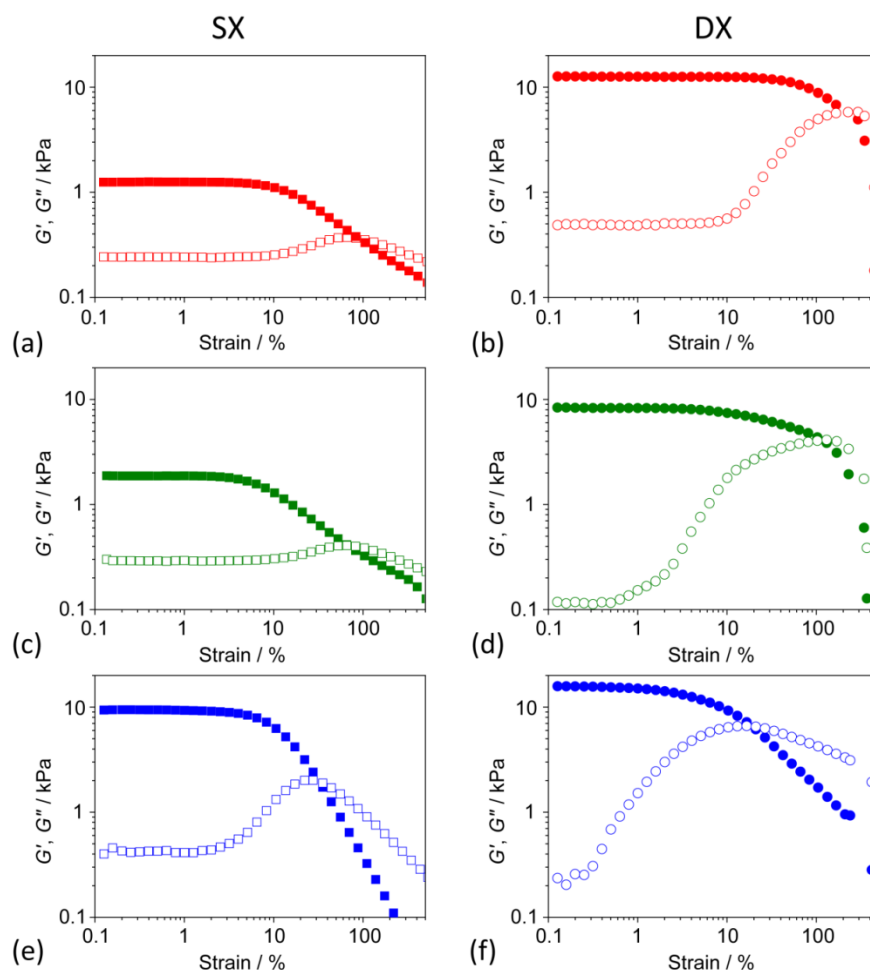


**Fig. 5.5.** Strain-sweep rheology data for SX MG physical gels (left) and the corresponding covalently-interlinked DX MGs (right). The data shown are for (a) SX DVB, (b) DX DVB, (c) SX DVB-BDDA, (d) DX DVB-BDDA, (e) SX BDDA and (f) DX BDDA. The closed and open symbols represent the storage modulus ( $G'$ ) and the loss modulus ( $G''$ ), respectively.



For region (2), the decrease of  $G'$  occurs indicates that the gel structures start to fail. The point where the  $G'$  data passed through the  $G''$  maximum is considered as a critical point indicating the gel structure fully failed. The strain at this point is defined as critical strain ( $\gamma_c$ ) and it can be used as a defined value to judge the ductility of the gels. Therefore, for the DX gels, the  $\gamma_c$  value for DX DVB was much higher than the other two as shown in Fig 5.6. The  $\gamma_c$  value for SX gels (See Fig. 5.6a and b) follows the same trend as DX gels, which is, SX DVB > SX DVB-BDDA > SX BDDA. These data show that construction of MGs using DVB gave more ductile SX MGs and DX MGs. However, the modulus of DX DVB gels were lower than DX BDDA gels. Both SX BDDA and DX BDDA had the highest modulus as shown in Fig. 5.6a and b.

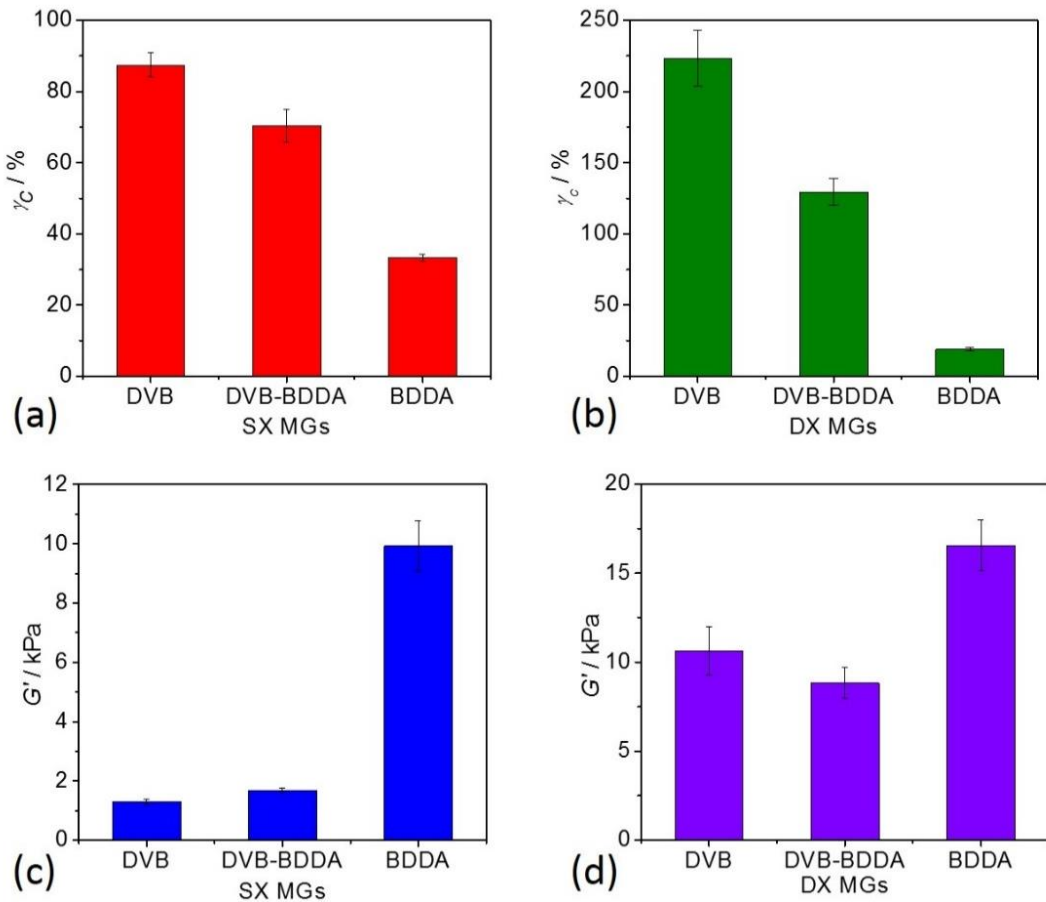


**Fig. 5.6.** Critical strain of SX MG gels (a) and the DX MGs (b). Shear modulus of SX MG (c) and DX MGs (d).

The variation of  $\gamma_c$  for the various gel can be explained using a well-known cage-breaking theory<sup>28</sup>. In this theory, each particle is trapped in a cage of its nearest neighbour particles<sup>29</sup> and the  $\gamma_c$  values of DX gels can be considered as the minimum strain for this particles to escape from the cage (i.e. cage break) or the maximum strain to cause irreversible particle rearrangement. For the  $\gamma_c$  values in Fig. 5.6a, the SX DVB MG gel had the highest value indicate that the SX MG particle is the most deformable particles in three. With the cage built by these particles and inter-linked with each other, the DX DVB MG can stand a relatively high strain before cage breaking as shown in Fig 5.6b. Here, we propose that internal failure of the intra-particle network within the MGs determined the  $\gamma_c$  values, and this was highest for the DVB MG because those particles were the most flexible which has been indicated by their pronounced particles swelling as shown in Fig. 5.2.

### 5.4.3 DX MG morphology

The morphology of DX MGs was assessed by SEM images as shown in Fig 5.7. The images of freeze-dried DX MGs showed typical hydrogel structures<sup>23</sup> which are highly porous. The pores were formed during the rapid ice formation. Interestingly, an obvious difference between Fig 5.7a and Fig. 5.7e is that the average pore size of DX DVB gels is larger than the DX BDDA gel. The average pore sizes were determined by measuring 100 pores and the average values for DX DVB, DX DVB-BDDA and DX BDDA were  $6.3 \pm 3.2$ ,  $5.3 \pm 1.8$  and  $1.1 \pm 0.4$   $\mu\text{m}$ , respectively. The average pore size of the freeze-dried gels increased as the DVB content for the parent MGs increased. It follows that the DX DVB gels were the most deformable under same applied force condition (ice formation). Such porous materials have been considered as potential materials for tissue scaffold applications<sup>30-31</sup>. Moreover, the

present work gives a possible method in tuning the pore size of the freeze-dried hydrogel by selection of the crosslinking monomers<sup>32</sup>.

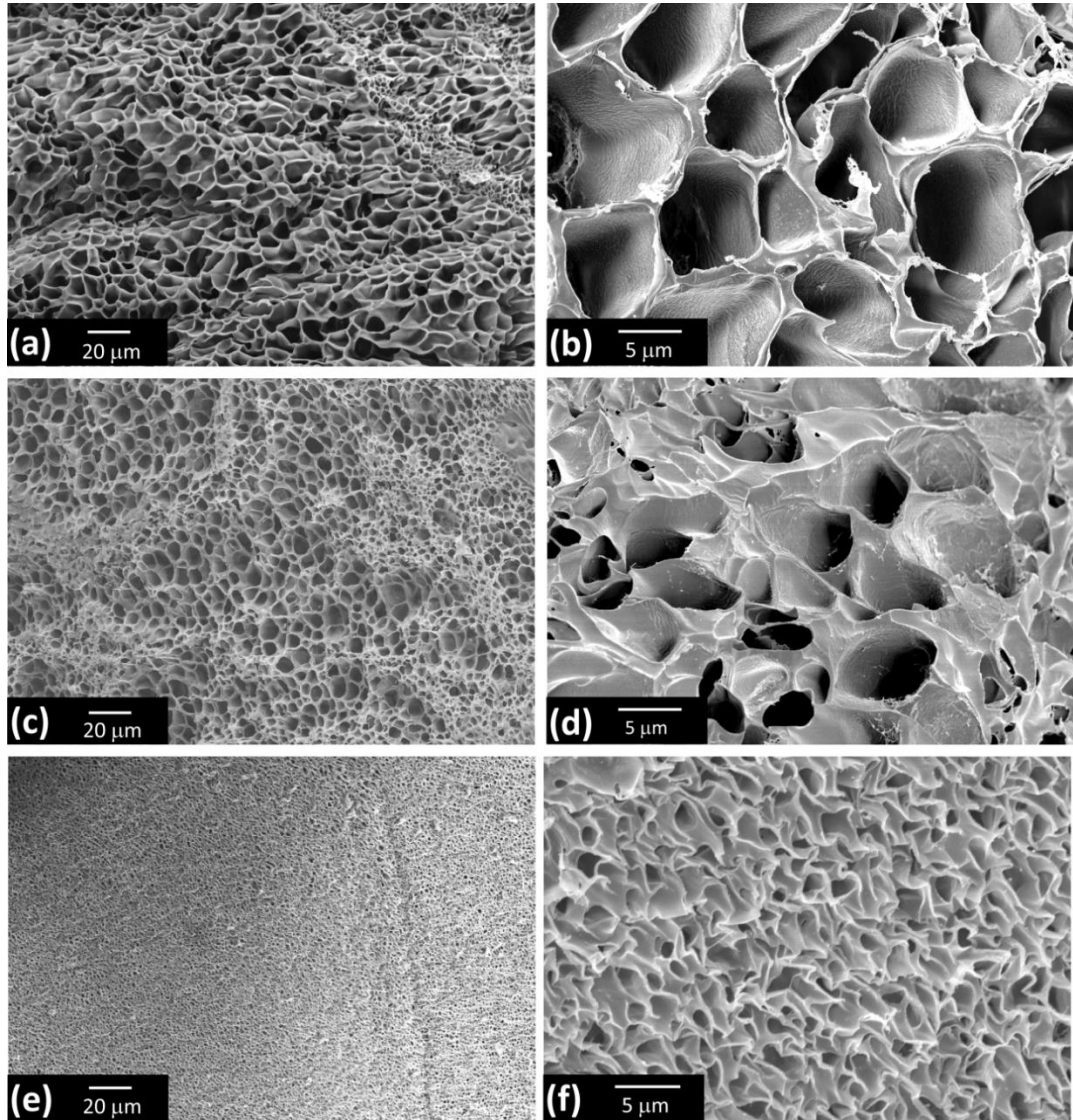


**Fig. 5.7.** SEM images for freeze-dried DX DVB (a) and (b), DX DVB-BDDA (c and d) and DX BDDA (e and f). (a), (c) and (e) are low magnification images and (b), (d) and (f) are higher magnification images.

#### 5.4.4 Uniaxial compression and bending of the DX MGs

The static uniaxial compression tests were performed for all DX MG gels. The stress vs. strain data of selected representative measurements are shown in Fig. 5.8. The compression modulus ( $E$ ) was calculated from the slope of the initial 10% part in the total curves before failure. The strain-at-break ( $\varepsilon_B$ ) was determined when the curve started to fall and the associated stress at this point is the maximum stress ( $\sigma_B$ ). The

average values of these parameters are shown in Table 5.3. The DX DVB was much more ductile than DX BDDA MG system. The deformation of DX DVB sample under compression was photographed insets in Fig 5.8). The average value of  $\varepsilon_B$  for the DX DVB was 76.1 % which is an outstanding improvement compared to 19.7 % for DX BDDA (the latter is a standard DX MG). In addition, the DX DVB gel can also stand about 14 times more stress before being broken compared to DX BDDA. The  $E$  value modulus showed the opposite behaviour and increased in the order DX DVB < DX DVB-BDDA < DX BDDA. (See Table 5.3). This trend follows the observation of pore size in Fig 5.7 and supports the view that the stiffer gels formed the smaller pores. The  $E$ ,  $\varepsilon_B$  and  $\sigma_B$  values for DX DVB-BDDA were always between those for DX DVB and DX BDDA. The compression data trends for stiffness ( $E$ ) and ductility ( $\varepsilon_B$ ) matched those observed from rheology as measured by  $G'$  and  $\gamma_c$  (see Fig. 5.5), respectively. DX DVB was very ductile. In fact, the average  $\varepsilon_B$  value of 76.1% for DX DVB MG is a record for DX MGs prepared using GMA functionalisation.<sup>11, 33</sup>

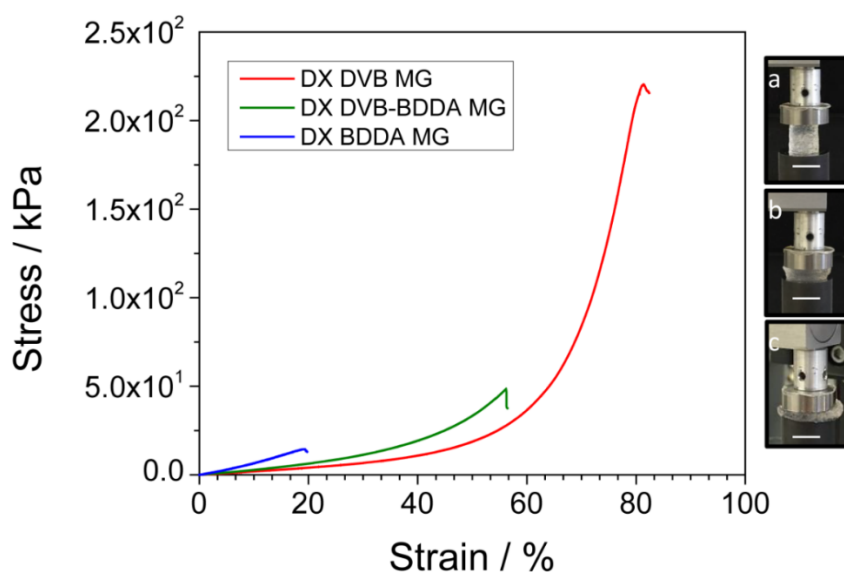


**Fig. 5.8.** Uniaxial compression stress vs. strain data for DX MGs prepared using various crosslinkers. The photographs show DX DVB MG compressed at different strains which were (a) 0%, (b) 40% and (c) 80%. The scale bars represent 10 mm.

**Table 5.3.** Static uniaxial compression data for the DX MGs.

Abbreviations	$E$ / kPa <sup>a</sup>	$\varepsilon_B$ / % <sup>b</sup>	$\sigma_B$ / kPa <sup>c</sup>
DX DVB	$19.8 \pm 1.6$ <sup>c</sup>	$76.1 \pm 4.8$	$207.1 \pm 10$
DX DVB-BDDA	$26.4 \pm 1.0$	$57.8 \pm 3.7$	$54 \pm 11$
DX BDDA	$53.2 \pm 5.2$	$19.7 \pm 0.4$	$14.5 \pm 0.1$

<sup>a</sup> Calculated from the initial gradient of stress vs. strain curves. <sup>b</sup>  $\varepsilon_B$  and <sup>c</sup>  $\sigma_B$  are strain-at-break and stress-at-break values, respectively.

Fig. 5.9 shows a series of screenshot images from a video which demonstrated that a DX DVB gel film was completely folded over and subsequently relaxed without damage. This process was repeated for three times. This performance cannot be achieved by any DX gels shown in earlier chapters, and these images demonstrate the remarkably flexible nature of the DX DVB systems.

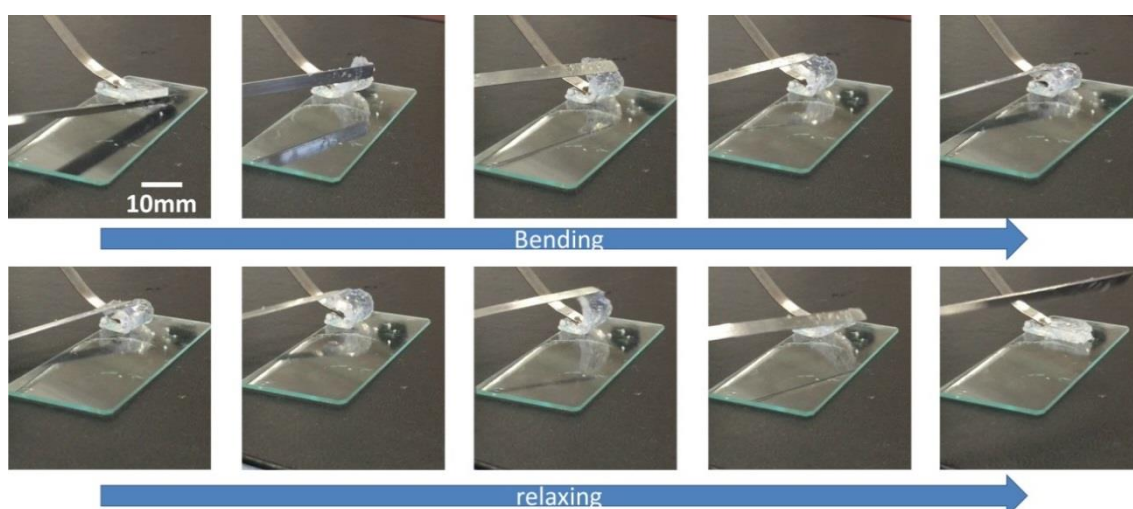


**Fig. 5.9.** The DX DVB MG film was tested under bending followed by relaxations cycles. The process was repeated for three times. (The sample is prepared as pie shape with diameter of 20 mm and thickness of 2 mm and cut in half)

#### 5.4.5 Proposed relationship between MG and DX MG mechanical properties

In the following, we test our assumption that the mechanical properties of the DX MGs were governed by those of the constituent MGs. The variation of  $E$  and  $\varepsilon_B$  are plotted as a function of  $Q$  in Fig. 7a. It can be seen from these data that the ductility of DX MGs (as measured by  $\varepsilon_B$ ) increased with increasing  $Q$  for the parent SX MGs. By contrast, the  $E$  values decreased with increasing  $Q$ .

We assume that the MG particles consist of perfect polymer networks as described in Flory's theory<sup>34</sup> and the swelling equilibrium with two components (polymer and solvent) are ideal as described in Chapter 2, Section 2.1.8.2. When the DX MG are applied by a small deformation, the applied force per unit area,  $\tau_s$  can be expressed by following equation<sup>35-37</sup>:

$$\tau_s = \left(\frac{v_e}{V_0}\right) RT \varphi_1^{1/3} \varphi_2^{2/3} (\alpha - \alpha^{-2}) \quad (5.2)$$

Where is  $(v_e/V_0)$  is effective chain network density (i.e. the effective crosslinking degree of DX MGs),  $R$  is the gas constant,  $T$  is absolute temperature,  $\alpha$  is the deformation ratio,  $\varphi_1$  is the polymer volume fraction for a swollen hydrogel (i.e. for DX gels),  $\varphi_2$  is the polymer volume fraction for swollen particles. So, we could assume  $E \sim \tau_s$  and  $\varphi_2 = Q^{-1}$ , and hence the  $E$  and  $Q$  values for the DX MG and parent MG should be related by  $E^{3/2} \sim Q^{-1}$  or  $E \sim Q^{-2/3}$ . This relationship was tested for the MGs and DX MGs (Fig. 7b). The data from our three DX MGs and parent MG systems showed perfect linearity.

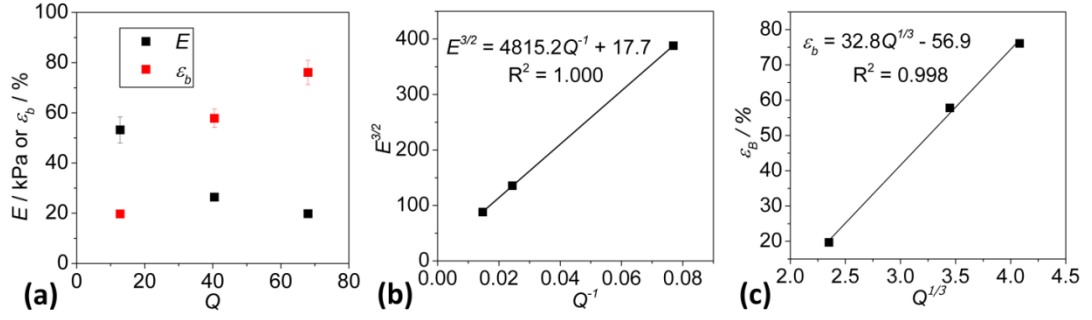


**Fig. 5.10.** (a) Variations of the modulus,  $E$ , and the strain-at-break,  $\varepsilon_b$ , for the DX MGs with the MG particle swelling ratio,  $Q$ , for the respective parent MG particles. (b) and (c) show the relationships between the  $E$  and  $\varepsilon_b$  values, respectively, and  $Q$ .

For a three dimensions network,<sup>34</sup> the modulus of networks is proportional to the number density of effective elastic chains,  $v_{eff}$  within MGs, then we can get  $v_{eff} \sim Q^{-2/3}$ . We next consider the ductility of the DX MGs. According to rubbery elasticity theory,<sup>38</sup> the maximum extension of a polymer chain is proportional to square root of the number of random links,  $n^{1/2}$  in the chain (i.e.  $\varepsilon_b \sim n^{1/2}$ ). The  $n$  is proportional to the average molecular weight of the elastically effective chains,  $M_{eff}$ . The relation between  $M_{eff}$  and  $v_{eff}$  can be expressed as:

$$\rho = M_{eff} \times v_{eff} \quad (5.3)$$

Where  $\rho$  is the density of the total networks within MGs. So the relationship between  $Q$  and  $\varepsilon_b$  can be derived as  $\varepsilon_b \sim Q^{1/3}$ . The plot of this relationship is shown in Fig. 5.10c, which showed an excellent linear behaviour.

In summary, both modulus and ductility of DX MGs are related to the swelling properties of MG particles, which is further controlled by the  $v_{eff}$  within MGs. The mechanical properties are dominated by the intra-linking of MGs particles but not the inter-linking. The main function for inter-linking in DX system is to fasten and adhere the MG particles to neighbouring particles to form the macroscopic gels.

## 5.5 Conclusions

In this chapter, the effects of the crosslinking monomer (DVB and BDDA) on the properties of pH-responsive MGs and DX MGs were investigated. The highly hydrophobic and fast-reacting crosslinker (DVB) was studied to prepare highly swellable MG particles. The results indicate that the selection of crosslinking monomer is important for controlling and determining the mechanical properties of DX MGs. The high  $Q$  values of MG particles lead to a highly ductile DX MGs. The novel DX DVB MG system performed as a ductile hydrogel with a very high  $\varepsilon_B$  value of 76%. This value is a new record for this class of DX MGs. Here, we provide a new possible tool to control the ductility of this system by selecting the crosslinkers. This ability benefits for designing and preparing improved injectable pH-responsive DX MG systems in future and these materials may provide a promising route for fabrication soft tissue engineering or degenerative medicine application.<sup>39</sup>



## 5.6 References

1. Richtering, W.; Saunders, B. R., Gel architectures and their complexity. *Soft Matter* **2014**, 10, 3695-3702.
2. Chen, Q.; Zhu, L.; Chen, H.; Yan, H.; Huang, L.; Yang, J.; Zheng, J., A Novel Design Strategy for Fully Physically Linked Double Network Hydrogels with Tough, Fatigue Resistant, and Self-Healing Properties. *Adv. Funct. Mater.* **2015**, 25, 1598-1607.
3. Sydney Gladman, A.; Matsumoto, E. A.; Nuzzo, R. G.; Mahadevan, L.; Lewis, J. A., Biomimetic 4D printing. *Nat. Mater.* **2016**, 15, 413-418.
4. Zhang, Z.; He, Z.; Liang, R.; Ma, Y.; Huang, W.; Jiang, R.; Shi, S.; Chen, H.; Li, X., Fabrication of a Micellar Supramolecular Hydrogel for Ocular Drug Delivery. *Biomacromolecules* **2016**, 17, 798-807.
5. Rosales, A. M.; Anseth, K. S., The design of reversible hydrogels to capture extracellular matrix dynamics. *Nat. Rev. Mater.* **2016**, 1, 15012.
6. Xavier, J. R.; Thakur, T.; Desai, P.; Jaiswal, M. K.; Sears, N.; Cosgriff-Hernandez, E.; Kaunas, R.; Gaharwar, A. K., Bioactive Nanoengineered Hydrogels for Bone Tissue Engineering: A Growth-Factor-Free Approach. *ACS Nano* **2015**, 9, 3109-3118.
7. Motamed, S.; Del Borgo, M. P.; Kulkarni, K.; Habila, N.; Zhou, K.; Perlmutter, P.; Forsythe, J. S.; Aguilar, M. I., A self-assembling beta-peptide hydrogel for neural tissue engineering. *Soft Matter* **2016**, 12, 2243-6.
8. Costa, A. M. S.; Mano, J. F., Extremely strong and tough hydrogels as prospective candidates for tissue repair – A review. *Eur. Polym. J.* **2015**, 72, 344-364.
9. Flory, P. J., *Principles of polymer chemistry*. Cornell University Press: Ithaca, N.Y., 1953; p xvi, 672 p.
10. Gong, J. P., Why are double network hydrogels so tough? *Soft Matter* **2010**, 6, 2583.
11. Liu, R.; Milani, A. H.; Freemont, T. J.; Saunders, B. R., Doubly crosslinked pH-responsive microgels prepared by particle inter-penetration: swelling and mechanical properties. *Soft Matter* **2011**, 7, 4696-4704.
12. Cui, Z.; Milani, A. H.; Greensmith, P. J.; Yan, J.; Adlam, D. J.; Hoyland, J. A.; Kinloch, I. A.; Freemont, A. J.; Saunders, B. R., A Study of Physical and Covalent Hydrogels Containing pH-Responsive Microgel Particles and Graphene Oxide. *Langmuir* **2014**, 30, 13384-13393.

13. Wu, X.; Pelton, R. H.; Hamielec, A. E.; Woods, D. R.; McPhee, W., The kinetics of poly(N-isopropylacrylamide) microgel latex formation. *Colloid. Polym. Sci.* **1994**, 272, 467-477.
14. Meyer, S.; Richtering, W., Influence of Polymerization Conditions on the Structure of Temperature-Sensitive Poly(N-isopropylacrylamide) Microgels. *Macromolecules* **2005**, 38, 1517-1519.
15. Acciaro, R.; Gilányi, T.; Varga, I., Preparation of Monodisperse Poly(N-isopropylacrylamide) Microgel Particles with Homogenous Cross-Link Density Distribution. *Langmuir* **2011**, 27, 7917-7925.
16. Destribats, M.; Eyharts, M.; Lapeyre, V.; Sellier, E.; Varga, I.; Ravaine, V.; Schmitt, V., Impact of pNIPAM Microgel Size on Its Ability To Stabilize Pickering Emulsions. *Langmuir* **2014**, 30, 1768-1777.
17. Zhang, B.; Wei, B.; Hu, X.; Jin, Z.; Xu, X.; Tian, Y., Preparation and characterization of carboxymethyl starch microgel with different crosslinking densities. *Carbohydr. Polym.* **2015**, 124, 245-253.
18. Still, T.; Chen, K.; Alsayed, A. M.; Aptowicz, K. B.; Yodh, A. G., Synthesis of micrometer-size poly(N-isopropylacrylamide) microgel particles with homogeneous crosslinker density and diameter control. *J. Colloid Interface Sci.* **2013**, 405, 96-102.
19. Errede, L. A., Polymer swelling. 5. Correlation of relative swelling of poly(styrene-co-divinylbenzene) with the Hildebrand solubility parameter of the swelling liquid. *Macromolecules* **1986**, 19, 1522-1525.
20. Koenhen, D. M.; Smolders, C. A., The determination of solubility parameters of solvents and polymers by means of correlations with other physical quantities. *J. Appl. Polym. Sci.* **1975**, 19, 1163-1179.
21. Brandrup, J.; Immergut, E. H.; Grulke, E. A., *Polymer handbook*. 4th ed.; Wiley: New York ; Chichester, 1999.
22. Rodriguez, B. E.; Wolfe, M. S.; Fryd, M., Nonuniform Swelling of Alkali Swellable Microgels. *Macromolecules* **1994**, 27, 6642-6647.
23. Lally, S.; Bird, R.; Freemont, T. J.; Saunders, B. R., Microgels containing methacrylic acid: effects of composition on pH-triggered swelling and gelation behaviours. *Colloid. Polym. Sci.* **2009**, 287, 335-343.
24. Tiwari, R.; Heuser, T.; Weyandt, E.; Wang, B.; Walther, A., Polyacid microgels with adaptive hydrophobic pockets and ampholytic character: synthesis, solution properties and insights into internal nanostructure by cryogenic-TEM. *Soft Matter*

**2015**, 11, 8342-8353.

25. Milani, A. H.; Freemont, A. J.; Hoyland, J. A.; Adlam, D. J.; Saunders, B. R., Injectable Doubly Cross-Linked Microgels for Improving the Mechanical Properties of Degenerated Intervertebral Discs. *Biomacromolecules* **2012**, 13, 2793-2801.

26. Tadros, T. F., Emulsion Formation, Stability, and Rheology. In *Emulsion Formation and Stability*, Wiley-VCH Verlag GmbH & Co. KGaA: 2013; pp 1-75.

27. Saunders, B. R.; Vincent, B., *Adv. Coll. Interf. Sci.* **1999**, 80, 1-25.

28. van der Vaart, K.; Rahmani, Y.; Zargar, R.; Hu, Z.; Bonn, D.; Schall, P., Rheology of concentrated soft and hard-sphere suspensions. *J. Rheol.* **2013**, 57, 1195-1209.

29. Pham, K. N.; Petekidis, G.; Vlassopoulos, D.; Egelhaaf, S. U.; Poon, W. C. K.; Pusey, P. N., Yielding behavior of repulsion- and attraction-dominated colloidal glasses. *J. Rheol.* **2008**, 52, 649-676.

30. Yao, X.; Yao, H.; Li, Y., Hierarchically aligned porous scaffold by ice-segregation-induced self-assembly and thermally triggered electrostatic self-assembly of oppositely charged thermosensitive microgels. *J. Mater. Chem.* **2009**, 19, 6516-6520.

31. Chau, M.; De France, K. J.; Kopera, B.; Machado, V. R.; Rosenfeldt, S.; Reyes, L.; Chan, K. J. W.; Förster, S.; Cranston, E. D.; Hoare, T.; Kumacheva, E., Composite Hydrogels with Tunable Anisotropic Morphologies and Mechanical Properties. *Chem. Mater.* **2016**, 28, 3406-3415.

32. Roman, J.; Cabanas, M. V.; Pena, J.; Vallet-Regi, M., Control of the pore architecture in three-dimensional hydroxyapatite-reinforced hydrogel scaffolds. *Sci. Tech. Adv. Mater.* **2011**, 12.

33. Cui, Z.; Wang, W.; Obeng, M.; Chen, M.; Wu, S.; Kinloch, I.; Saunders, B. R., Using intra-microgel crosslinking to control the mechanical properties of doubly crosslinked microgels. *Soft Matter* **2016**, 12, 6985-6994.

34. Flory, P. J., Molecular Theory of Rubber Elasticity. *Polym. J.* **1985**, 17, 1-12.

35. Mawad, D.; Foster, J. L. J. R.; Lauto, A., Drug-delivery study and estimation of polymer-solvent interaction parameter for bisacrylate ester-modified Pluronic hydrogels. *Int. J. Pharm.* **2008**, 360, 231-235.

36. Ruiz, J.; Mantecón, A.; Cádiz, V., Network characterization and swelling behavior of chemical hydrogels based on acid - containing poly(vinyl alcohol). *J.*

*Appl. Polym. Sci.* **2003**, 88, 3026-3031.

37. Abdurrahmanoglu, S.; Can, V.; Okay, O., Equilibrium swelling behavior and elastic properties of polymer–clay nanocomposite hydrogels. *J. Appl. Polym. Sci.* **2008**, 109, 3714-3724.

38. Treloar, L. R. G., *The physics of rubber elasticity*. 3rd ed.; Clarendon: Oxford, 2005; p xii, 320 p.

39. Frith, J. E.; Cameron, A. R.; Menzies, D. J.; Ghosh, P.; Whitehead, D. L.; Gronthos, S.; Zannettino, A. C. W.; Cooper-White, J. J., An injectable hydrogel incorporating mesenchymal precursor cells and pentosan polysulphate for intervertebral disc regeneration. *Biomaterials* **2013**, 34, 9430-9440.

## Chapter 6: Conclusions and future works

### 6.1 Summary of conclusions

The main aim of this research is to design and develop the pH-responsive doubly crosslinked(DX) microgels(MGs) based materials and composites for potential use in soft tissue engineering. The mechanical properties of each material were specially focused through it directly relate to if they can support mechanical loading when applied *in vivo*. Besides, other properties like swelling properties, morphology and cytotoxicity were also studied to comprehensively understand MG and MG-contained composites systems.

Composite strategy offered a simple and flexible route to prepare high modulus gels using the incorporation of vinyl functionalised MG particles and graphene oxide (GO). The study of MG/GO composites was described in Chapter 3, which showed the possibility to blend the concentrated MG dispersion with the GO dispersion. The singly crosslinked (SX) was successfully prepared by increasing the pH of the blending dispersion. The physical gel is injectable and enables a further curing process to form a covalently gels (DX) in the presence of an initiator. This process can be applied to an injected medicine. The introduced GO was proved to significantly improve the modulus for both SX gels and DX gels which followed a linear isostrain model for GO loading. The results from live / dead assay for DX MG/GO composites demonstrate the gels were not toxic that the gel had potential application in biomaterials such as IVD repair.

Chapter 4 showed a method to prepare a new class of MG composites constructed by carbon nanotubes (CNTs) networks and MG building blocks. The method also

includes the MGs which were used as a dispersant for CNTs to obtain a stable and finely dispersed composites. Similar to MG/GO composites, the SX MG/CNT physical gels are injectable which were formed when the pH was increased to approach human body environment. Both modulus and ductility of DX MG/CNT composite gels were improved by the addition of CNT, and these gels showed a long-period structural stability in PBS solution. Moreover, the DX MG/CNT composite gels were electrical conductive with a very low percolation threshold of CNT. The feedback from cytotoxicity measurements for the composites showed they are not cytotoxic. These conductive composites have potential applications in soft tissue repairing like biomechanical monitoring or electronic skin.

Though Chapter 4 and 5, we have shown the ability to design a DX gel with considerable enhancement in modulus. However, there is a lack of tools to improve the ductility. Chapter 6 investigate the effect from the nature of crosslinking monomers on the pH-responsive and mechanical properties of MG particles. The investigation in this chapter analysed the relationship between the swelling properties of MG particles and the mechanical properties of their corresponded DX MGs. The comparison data about the crosslinking monomers was focused on the differences from divinylbenzene (DVB), or 1,4-butanediol diacrylate (BDDA) or their mixtures. The results demonstrate that the crosslinking monomer played a considerable role in determining the swelling ratio of MG particles and the mechanical properties of DX gels. As results, a new type of MG particles using divinylbenzene (DVB) as crosslinking monomer showed a significant improvement comparing to other MGs. The results also showed the possible design tools for improving DX MG ductility by adjusting the crosslinking monomers, and therefore expanding the range of potential applications for this new class of hydrogel.

## 6.2 Future works

The results from Chapter 4 and 5 show it is possible to introduce a 1D or 2D filler into MG dispersion. However, the dark colour and the low transparency of GO/MG and CNT/MG composites may significantly affect the impression of clients and limit their applications in biomedicine field. Therefore, some fillers with similar structures such as gold nanorods, cellulose and chitosan nanowires (1D), or silicate and calcium phosphate nanoplates (2D) are worthwhile. Furthermore, the method for utilising GO sheets in Chapter 4 can be updated. The thickness and size of as-made GO sheets are not uniform. The large pieces of GO significantly increase the possibility of mechanical defects. It can be improved by adding a size-selecting process and investigating the effect of the size of uniform GO sheets on the mechanical properties of DX gels. Moreover, the surface and edge of GO sheets are chemically reactive. If nano-sized GO sheets can be separated and functionalised which enables the GO involving in the crosslinking structure, it could be more efficient to improve the modulus of DX gels than simply blending two dispersions without solid interaction between filler and the MG particles. Besides, the morphology data in Chapter 4 and 5 show that the fillers are randomly distributed in the MG continuous phase. If the filler can be aligned to selected orientations, some new features can be introduced to MGs. For example, if the CNTs are aligned in one direction, the modulus in the axial direction are supposed to be larger than other directions, and this axial direction can be placed as same as stress direction. The alignment of CNTs can be achieved by applying force<sup>1</sup> or by applying an electric field.<sup>2-3</sup>

In Chapter 6, we have shown the crosslinking monomers can significantly affect the mechanical properties of DX gels. However, we only studied the effect from various

types of crosslinking monomers, the relationship between structures of microscopic MG structures and the properties of macroscopic are worthy to dig further. One possible proposal is to study the influence of mechanical properties DX gels on the total feeding amount of crosslinking monomers. Higher feeding amount offered a higher crosslinking degree which may increase the modulus of DX gels.<sup>4</sup> Besides, the distribution of crosslinking junctions is worth to be controlled during seed-feed emulsion polymerisation. In our method, the co-monomers were continuously fed with the same composition. If the crosslinking monomer of high concentration in total co-monomer mixtures is fed at first and followed by the one in low concentration, a particle structure with a highly crosslinked “core” surrounded by some polymer arms may occur. The outer part could be more flexible and stand more deformation under strain and hence improve the ductility of DX gels.



### 6.3 References

1. Ding, W.; Pengcheng, S.; Changhong, L.; Wei, W.; Shoushan, F., Highly oriented carbon nanotube papers made of aligned carbon nanotubes. *Nanotechnology* **2008**, 19, 075609.
2. Kamat, P. V.; Thomas, K. G.; Barazzouk, S.; Girishkumar, G.; Vinodgopal, K.; Meisel, D., Self-Assembled Linear Bundles of Single Wall Carbon Nanotubes and Their Alignment and Deposition as a Film in a dc Field. *J. Am. Chem. Soc.* **2004**, 126, 10757-10762.
3. Ahadian, S.; Ramón-Azcón, J.; Estili, M.; Liang, X.; Ostrovidov, S.; Shiku, H.; Ramalingam, M.; Nakajima, K.; Sakka, Y.; Bae, H.; Matsue, T.; Khademhosseini, A., Hybrid hydrogels containing vertically aligned carbon nanotubes with anisotropic electrical conductivity for muscle myofiber fabrication. *Sci. Rep.* **2014**, 4, 4271.
4. Bryant, S. J.; Chowdhury, T. T.; Lee, D. A.; Bader, D. L.; Anseth, K. S., Crosslinking Density Influences Chondrocyte Metabolism in Dynamically Loaded Photocrosslinked Poly(ethylene glycol) Hydrogels. *Ann. Biomed. Eng.* **2004**, 32, 407-417.

## Appendix

### Published works

1. Cui, Z., Wang, W., Obeng, M., Chen, M., Wu, S., Kinloch, I., Saunders, B. R. Using intra-microgel crosslinking to control the mechanical properties of doubly crosslinked microgels. *Soft Matter* **2016** 12, 6985-6994
2. Cui, Z., Zhou, M., Greensmith, P. J., Wang, W., Hoyland, J., Kinloch, I., Freemont, T. J., Saunders, B. R. A study of conductive hydrogel composites of pH-responsive microgels and carbon nanotubes. *Soft Matter* **2016** 12, 4142-4153.
3. Cui, Z., Milani, A. H., Greensmith, P. J., Yan, J., Adlam, D. J., Hoyland, J. A., Kinloch, I.A., Freemont, T. J., Saunders, B. R. A Study of Physical and Covalent Hydrogels Containing pH-Responsive Microgel Particles and Graphene Oxide. *Langmuir* **2014** 30, 13384-93.

### Co-author works

4. Pafiti, K., Cui, Z., Adlam, D., Hoyland, J., Freemont, A. J., Saunders, B. R. Hydrogel composites containing sacrificial collapsed hollow particles as dual action pH-responsive biomaterials. *Biomacromolecules* **2016** 17, 2448–2458.
5. Pafiti, K., Cui, Z., Carney, L., Freemont A. J., Saunders, B. R. Composite gels of polyacrylamide and crosslinked pH-responsive micrometer-sized hollow particles. *Soft Matter* **2016** 12, 1116-1126
6. Yan, J., McNaughter, P. D., Wang, Z., Hodson, N., Chen, M., Cui, Z., O'Brien, P., Saunders, B. R. Controlled aggregation of quantum dot dispersions by added amine bilinkers and effects on hybrid polymer film properties. *RSC Advance* **2015** 5, 95512-95522
7. Chen, M., Cui, Z., Edmondson, S., Hodson, N., Zhou, M., Yan, J., O'Brien, P., Saunders, B. R. Photoactive composite films prepared from mixed dispersions of polystyrene microgel particles and poly(3-hexylthiophene). *Soft Matter* **2015** 11, 8322-8332
8. Wang, W., Milani, A. H., Carney, L., Yan, J., Cui, Z., Thaiboonrod, S., Saunders, B. R. Doubly crosslinked microgel-colloidosomes: a versatile method for pH-responsive capsule assembly using microgels as macrocrosslinkers. *Chemical Communications* **2015** 51, 3854-7.